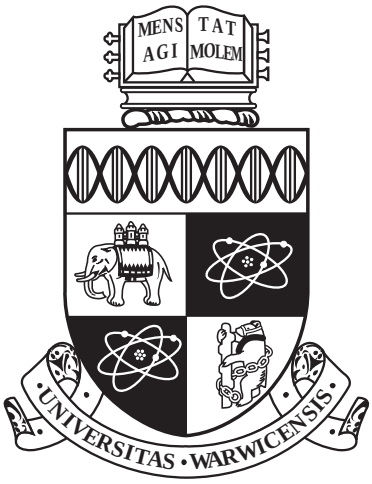

Simple Collision Operators for Direct Vlasov Solvers

by

Daniel Fletcher

Thesis

Submitted to the University of Warwick

for the degree of

Doctor of Philosophy

Department of Physics

March 2014

THE UNIVERSITY OF
WARWICK

Contents

Acknowledgments

I'd like to thank my parents for their continuing support and belief in me throughout my studies. I'd also like to thank my supervisor, Tony for helpful discussions and continued patience and support.

Declarations

All work and results presented in this thesis were produced by myself except where clearly noted.

Abstract

Existing codes for directly solving for the particle distribution function in laser plasma interaction studies either assume a collisionless plasma or solve for the full Fokker-Planck collision term. The former approach is the basis of an existing code at Warwick (VALIS). The latter approach is computationally expensive and often relies on a spherical harmonic expansion of the distribution function, making the implementation of a laser driver difficult. Here the existing collisionless code is extended by including reduced collision operators based on both the Krook and Fokker-Planck operator. The formulation of a fully conservative velocity-dependent Krook operator that shows agreement classical transport co-efficients in the regimes they are valid. The accuracy of the operator is shown to be improved using a normalisation method to ensure the Krook model yields the same heat flux as the Fokker-Planck model. The Krook model is also shown to be in agreement with full Vlasov-Fokker-Planck simulations of non-local transport. Two forms of a model Fokker-Planck operator are also included as a comparison to other reduced models of collisions.

Chapter 1

Introduction

1.1 Thesis Overview

In this chapter some key issues in fusion energy and inertial confinement schemes are introduced, in particular the issue of fast electron transport in fast ignition. The fundamental concepts of the kinetic approach are then discussed and illustrated through the derivation of Vlasov's equation. Coulomb collisions are then introduced and collision operators that attempt to model the collective effect these have on the distribution function. Finally aspects of laser-plasma physics where collisions may and may not be neglected are discussed. The second chapter describes the 2D2P Vlasov-Maxwell code VALIS and explains the justification for directly solving Vlasov's equation rather than using other methods. The third chapter details the formulation and implementation of the Krook collision operator and verifies the results both in regimes where classical transport is valid and in regimes relevant to inertial confinement fusion experiments. In the fourth chapter a method of implementing a phenomenological heating source using a method similar to the Krook operator. The next chapter described alternative collision operators based on a reduced Fokker-Planck equation. Again these were tested against classical transport coefficients and the Krook operator. In the final chapter the Vlasov-Maxwell-Krook code will be used to model a fast electron transport and return current generation problem relating to a fast ignition scenario. A previous study of this problem [1] using the Vlasov-Fokker-Plank model utilised an implicit field algorithm which allows a larger time step to be taken which is limited by the collision frequency rather than the plasma frequency. This method however

precludes resolution of electrostatic instabilities. The Vlasov-Maxwell-Krook code here employs an explicit field algorithm which can resolve these features.

1.2 Fusion Energy Overview

The concept of nuclear fusion as a source of energy began with the discovery of the mass-energy equivalence arising from the theory of special relativity developed by Einstein in 1905. The consequences of this relation for atomic physics were revealed by Aston in 1920 when his accurate mass spectrometry revealed the mass of four hydrogen atoms was greater than the mass of one helium atom. This discovery led to Eddington proposing that this change in mass due to the fusion process was the source of energy production in stars. Studies of nuclear physics in the 1920's and 30's allowed Bethe [2,3] to describe a sequence of thermonuclear reactions that could occur under the conditions at the centre of a star, known as the carbon cycle. This cycle is dominant in stars with core temperatures above $10^9 K$. In stars with cooler core temperatures however, such as our Sun, the proton-proton cycle is more common,

$$\begin{aligned} H_1^1 + H_1^1 &\rightarrow D_1^2 + e^+ + \nu && (1.44 MeV) \\ D_1^1 + H_1^1 &\rightarrow He_2^3 + \gamma && (5.49 MeV) \\ He_2^3 + He_2^3 &\rightarrow He_2^4 + 2H_1^2 && (12.86 MeV) \end{aligned}$$

Where e^+, ν and γ denote positrons, neutrinos and gamma rays respectively and the numbers in brackets denote the energy released by each reaction.

1.2.1 Ignition and Breakeven

For fusion reactions to occur, the nuclei must be brought within close proximity such that the strong nuclear force overcomes the Coulomb repulsion between the protons. In terms of fusion energy, ignition is defined as the point where the energy produced by nuclear reactions is sufficient enough to maintain the temperature of the plasma without an external power source. The general set of conditions that must be met for an energy producing nuclear reactor are often referred to as the Lawson criteria [4]. Assuming a deuterium-tritium fuel

with equal number densities, $n_D = n_T = n$, the power generated by a nuclear fusion reactor per unit volume is given by,

$$P_{fus} = \frac{1}{4} n^2 \langle \sigma v \rangle \Delta E$$

where $\langle \sigma v \rangle$ is the reaction rate which is the reaction rate derived from the collisional cross section, σ and the relative particle velocities. For a D-T plasma at 10KeV, $\langle \sigma v \rangle \sim 1.1 \times 10^{-22} m^3 s^{-1}$ [5], and ΔE for the D-T reaction is $17.6 MeV$, thus the power generated per unit volume, $P_{fus} = 7.7 \times 10^{-35} n^2 W m^{-3}$. Of the energy released in the D-T fusion reaction, only 20% is in the form of kinetic energy to alpha particles which are able to heat the plasma to sustain the nuclear reactions. The power available from the alpha particles, $P_\alpha = 0.2 P_{fus}$. The rest of the energy is carried by the neutrons which pass through the plasma into the walls of the reactor. The rate of other energy losses must also be taken into account such as radiative losses through bremsstrahlung and heat loss to the reactor wall. The energy confinement time τ_E is a measure of the rate of these losses. This is the ratio of the plasma energy density to the rate at which energy is lost, $\tau_E = W / P_{loss}$ where $W = 3 n k_B T$. The ignition criteria requires the power generated to be at least equal to the power lost from the plasma,

$$P_\alpha \geq P_{loss}$$

substituting in the values derived earlier,

$$\frac{1}{4} n^2 \langle \sigma v \rangle \Delta E_\alpha = \frac{3 n k_B T}{\tau_E}$$

which can be written as,

$$n \tau_E \geq \frac{12}{E_\alpha} \frac{k_B T}{\langle \sigma v \rangle}$$

It's useful to write an expression for this criteria as a triple product,

$$n_e T \tau_E \geq C$$

where C is a constant depending on the cross section of the nuclear reaction in question. For the Deuterium-Tritium reaction, $C = 10^{21} keV.s/m^3$.

In the centre of stars this condition is met by the force of gravity maintaining a high density confinement time. In the laboratory however the plasma

must be confined through alternative means. Magnetic confinement devices utilise the charged particle nature of a plasma to contain along magnetic field lines. A Tokamak confines the plasma in a toroidal chamber using the combination of toroidal and poloidal field lines. Since magnetic confinement devices contain the plasma for long periods of time, the energy carried by the neutrons is able to be converted into electricity by the reactor which can in turn be used to heat the plasma. In this case the Lawson criteria refers to breakeven, rather than ignition and requires,

$$P_\alpha + \eta P_n = \frac{3nk_BT}{\tau_E}$$

where η is the efficiency of conversion from neutron energy to a heating mechanism and P_n is the power supplied by the neutrons. Since the total energy carried by the neutrons is five times that of the alpha particles, this can be written as

$$P_\alpha = \frac{3nk_BT}{\tau_E}.\frac{1}{1+5\eta}$$

Breakeven can therefore be met with a lower P_α than is required for ignition.

The ITER tokamak device currently under construction in the south of France aims to reach breakeven after full deuterium-tritium operation begins in 2027 [6], with an ultimate aim of producing 10 times as much power as it consumes.

1.3 Inertial Confinement

1.3.1 Overview

Inertial Confinement Fusion in contrast to Magnetic Confinement Fusion attempts to reach ignition by compressing the plasma to far higher densities so that the Lawson criterion can be satisfied with a confinement time many orders of magnitude smaller. The energy confinement time, τ_E in this case is simply due to the inertia of the D-T fuel rather than external magnetic fields. For the D-T reaction the triple product can be written

$$nT\tau_E \geq 3 \times 10^{28} Ksm^{-3} \tag{1.1}$$

A sphere of fuel is heated to $10^8 K$ and expands at the thermal velocity,

$$\begin{aligned} v_{th} &\sim \frac{k_B T}{\bar{m}} \\ &\sim 6 \times 10^5 m s^{-1} \end{aligned}$$

where $\bar{m}$ is $(m_D + m_T)/2$. If the sphere expands to double the volume then the radius is increased by $\frac{1}{4}$. Estimating the energy confinement time as,

$$\tau_E = \frac{R}{4 v_{th}}$$

equation 1.1 can be written as

$$nR \geq 7.2 \times 10^{26}$$

or multiplying by $\bar{m}$ to give the mass density, ρ,

$$\rho R \geq 0.3 g.cm^{-2}$$

The burn fraction Φ_b, in other words the fraction of the DT fuel that can be expected to fuse before it flies apart can be show to be [7],

$$\Phi_b \simeq \frac{\rho R}{\rho R + 6}$$

and fusion energy output for this fraction can be calculated to be

$$E_{fus} = 3.3 \times 10^{11} M_b$$

where M_b is the DT mass burned. Assuming $\Phi_b = 1/3$ and setting an upper limit of fusion energy output to ensure the survival of the reactor at $E_{fus} = 10MJ$ (2.5kg TNT). The corresponding D-T fuel mass, $M = 10^{-4} g$. The mass of a spherical fuel capsule can be written,

$$M = \frac{4\pi}{3} \frac{(\rho R)^3}{\rho^2}$$

and since $\rho R = 3 g/cm^2$ is needed, compression up to $\rho = 10^3 g/cm^3$ is required to achieve ignition. For liquid density D-T fuel, $\rho = 0.21 g/cm^3$ so this corresponds to a volume compression requirement of over 10^3.

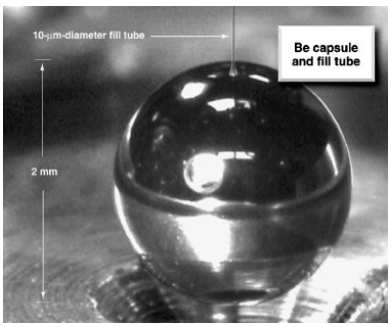

Figure 1.1: Fuel Capsule Prototype at the National Ignition Facility [8]

Inertial confinement fusion refers to a range of device designs which use lasers to heat and compress a fuel target. The largest inertial confinement experiment currently in operation is the National Ignition Facility(NIF) at Lawrence Livermore National Laboratory. The Laser driver at NIF is able to generate a 500 Terawatts with a peak energy of 1.8 Megajoules with a temporal pulse length of 10-20 nanoseconds [9]. The target capsule(figure 1.1 is comprised of an outer ablator shell made of a low Z material such as beryllium or a high density carbon and an inner fuel shell of deuterium-tritium ice which surrounds a core of DT gas. The core is a lower density to reduce its pressure therefore reduce the work required for compression. Figure 1.2 outlines the stages of an inertial confinement experiment. Initially the surface of the spherical target is irradiated by the laser and is rapidly heated. The hot outer shell rapidly rapidly expands reaching a pressure of around 100Mbar generating an implosion wave through the rocket effect. For ignition this implosion velocity, u_{imp} needs to be greater than $300 - 400km/s$. The imploding fuel reaches the highest temperature at the centre of the target where ignition occurs. The thermonuclear burn then propagates from the centre of the target through the surrounding fuel.

For efficient compression the laser energy must be delivered symmetrically over the surface of the capsule. Asymmetric heating over the shell produces lateral density perturbations that seed hydrodynamic instabilities such as the Rayleigh-Taylor instability. Indirect drive schemes surround the fuel capsule with a gold, cylindrical hohlraum as shown in figure 1.3. The laser at NIF has 192 beams which generate x-rays as they impinge on the inner walls of the gold hohlraum. It is these x-rays which are used to heat and implode the capsule. The smoother energy profile of the generated x-rays however comes

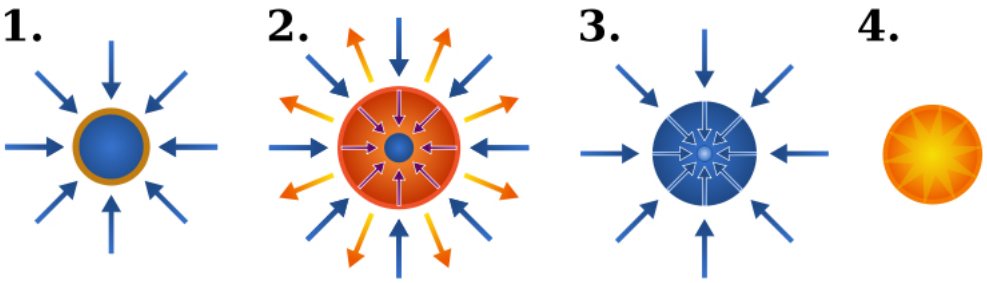

Figure 1.2: Stages of inertial confinement fusion [10]

at the cost of reduced coupling efficiency between the laser energy input and the fuel capsule.

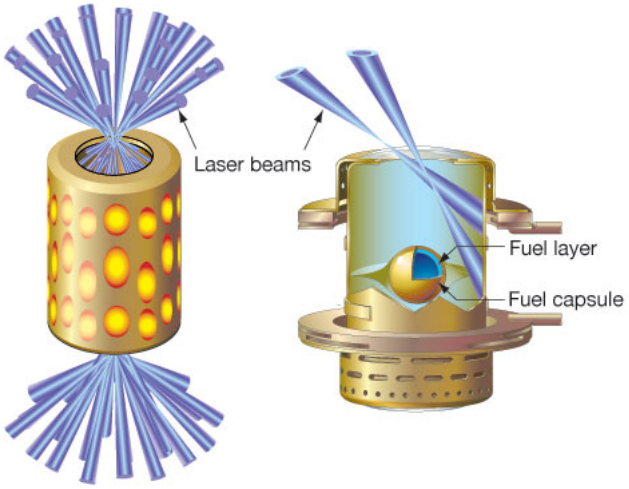

Figure 1.3: Overview of an indirect drive inertial confinement experiment. Image reproduced from Lawrence Livermore National Laboratory [11]

The hot spot at the centre of the compressed fuel capsule of radius R_h is typically much smaller than the initial capsule radius. The convergence ratio, $C_r = R_0/R_h \sim 30 - 40$ [12]. Deformations in the hotspot, $\delta R_h/R_h$ are related to implosion velocity asymmetry. The difference in radius, after an implosion time t_{imp}

$$R_0 - R_h = u_{imp} t_{imp}$$

considering implosion dynamics, the asymmetry of the hot spot can be esti-

mated,

$$\frac{\delta R_h}{R_h} \sim \left(\frac{R_0}{R_h} - 1\right) \frac{\delta u_{imp}}{u_{imp}}$$

the asymmetry in implosion velocity is due to pressure non-uniformity which itself is due to the asymmetry in target irradiation,

$$\frac{\delta u_{imp}}{u_{imp}} \sim \frac{\delta p_a}{p_a} \sim \frac{2}{3}\frac{\delta I}{I}$$

where growth of hydrodynamic instabilities due to pressure non-uniformity has been neglected. With these assumptions one still requires $\delta I \ll (3/2)(R_h/R_0)$.

1.3.2 Fast Ignition

Fast ignition is an ignition scheme where a hot spot is created after the fuel capsule has already begun imploding. In conventional fast ignition(see figure 1.4), an ultra-intense($\sim 10^{20} W/cm^2$) laser pulse is then fired which generates a beam of fast electrons around the critical density which produce a hot spot when they are stopped when they meet the compressed plasma. Such a scheme relaxes the symmetry requirements needed to generate a central hotspot required by conventional ICF schemes. The reduction in required laser energy and hydrodynamic requirements of the fuel capsule mean that fast ignition has the potential to produce greater gain. Numerous fast ignition schemes exist and are summarised in figure 1.6

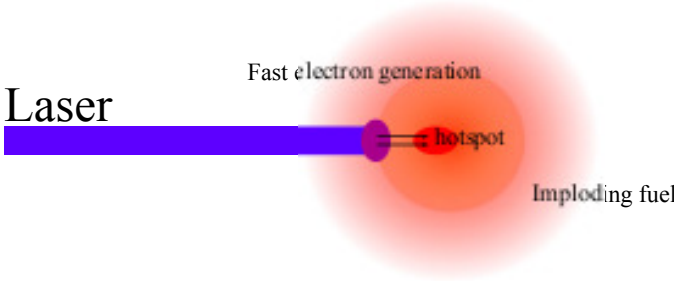

Figure 1.4: Conventional Fast ignition

There are issues however with the propagation of the short pulse laser beam through the coronal plasma before reaching the critical surface. To

alleviate this problem in conventional fast ignition the ultra-intense igniter beam is preceded by a lower power, hole boring pulse($\sim 10^{18} W/cm^2$). This then allows the igniter pulse to propagate uninhibited through the tunnel in the coronal plasma. Cone guided fast ignition uses a gold cone inserted into the side of the target. The gold cone maintains a vacuum during the implosion phase through which the igniter pulse can propagate. Fast electrons are generated when the igniter pulse hits the cone tip.

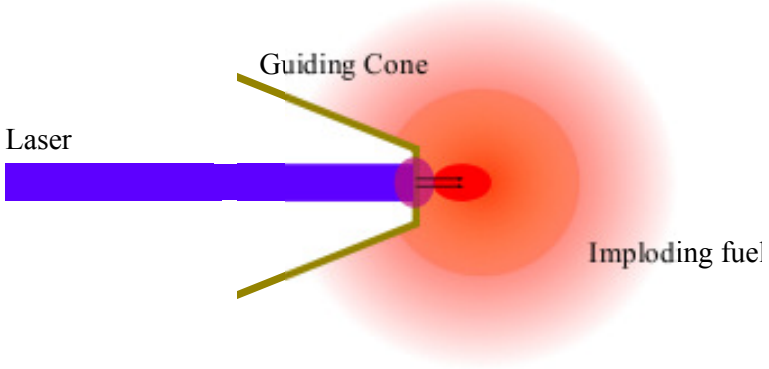

Figure 1.5: Cone Guided Fast ignition

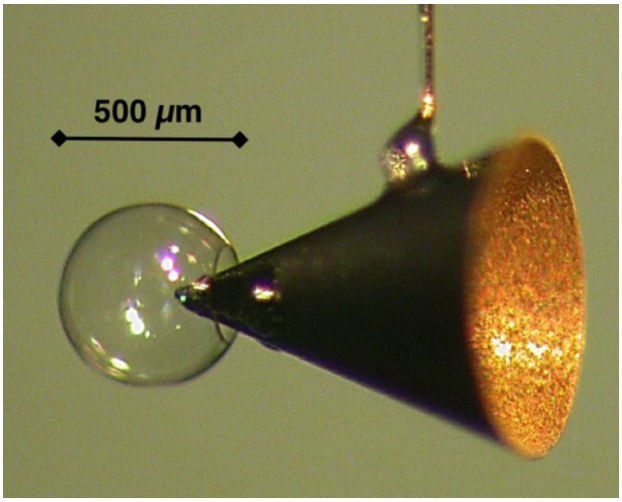

Figure 1.6: Cone guided fast ignition target [13]

1.3.3 Shock Ignition

Shock ignition [14] is another scheme which attempts to reach ignition through the collision between shocks. A central hotspot is created when a second, spherical symmetric ignitor shock, generated by a spike in laser energy collides with the reflected initial shock.

1.4 Plasma Physics Overview

1.4.1 Kinetic Theory and Vlasov's Equation

Rather than considering the overall bulk evolution of the plasma, kinetic theory instead considers the motion of each individual particle. The position and velocity of a single particle at a time t can be defined as its density function over phase space,

$$N(\mathbf{x}, \mathbf{v}, t) = \delta[\mathbf{x} - \mathbf{X}_1(t)]\delta[\mathbf{v} - \mathbf{V}_1(t)]$$

Where $\mathbf{x}$ and $\mathbf{v}$ are Eulerian co-ordinates in six dimensional phase space as $\mathbf{x} = (x, y, z)$ and $\mathbf{v} = (\mathrm{v}_x, \mathrm{v}_y, \mathrm{v}_z)$. $\mathbf{X}_1$ and $\mathbf{V}_1$ are the Lagrangian co-ordinates of the particle itself and δ is the Dirac delta function. If the particle exists at $\mathbf{X}_1 = \mathbf{x}$ and $\mathbf{V}_1 = \mathbf{v}$ the density function equals infinity there and zero everywhere else.

To get a complete description of all the particles of species s the density function must sum over N_0 the number density of the particles,

$$N_s(\boldsymbol{r}, \boldsymbol{v}, t) = \sum_{i=1}^{N_0} \delta[\mathbf{x} - \mathbf{X}_i(t)]\delta[\mathbf{v} - \mathbf{V}_i(t)]$$

At any time t the density of particles integrated over phase space is equal to the number of particles in the system. This follows from 1.4.1 due to the property of the Dirac delta,

$$\int_{-\infty}^{\infty} \delta(x)dx = 1$$

The total density is then given by the sum over each species, e.g. electrons and ions:

$$N(\mathbf{x}, \mathbf{v}, t) = \sum_{e,i} N_s(\mathbf{x}, \mathbf{v}, t)$$

Since derivative of the position is simply the velocity, it follows that if the position and velocity of a particle is known at a time t then we know them at all previous and later times. So

$$\dot{\mathbf{X}}_i(t) = \mathbf{V}_i(t) \tag{1.2}$$

where the overdot denotes the derivative with respect to time. The change of velocity with respect to time is given by the acceleration due to the Lorentz force,

$$F_i(t) = m_s\dot{\mathbf{V}}_i(t) = q_s\mathbf{E}^m[\mathbf{X}_i(t), t] + \frac{q_s}{c}\mathbf{V}_i(t) \times \mathbf{B}^m[\mathbf{X}_i(t), t] \tag{1.3}$$

Where the superscript m denotes the fields generated self-consistently by the point particles. These fields satisfy Maxwell's equations:

$$\begin{aligned}
\nabla.\boldsymbol{E}^m(\boldsymbol{x}, t) &= \frac{\rho^m(\boldsymbol{x}, t)}{\epsilon_0} \\
\nabla.\boldsymbol{B}^m(\boldsymbol{x}, t) &= 0 \\
\nabla \times \boldsymbol{E}^m(\boldsymbol{x}, t) &= -\frac{\partial \boldsymbol{B}^m(\boldsymbol{x}, t)}{\partial t} \\
\nabla \times \boldsymbol{B}^m(\boldsymbol{x}, t) &= \mu_0\boldsymbol{J}^m(\boldsymbol{x}, t) + \frac{1}{c^2}\frac{\partial \boldsymbol{E}^m(\boldsymbol{x}, t)}{\partial t}
\end{aligned}$$

Where the microscopic charge density and current are defined as:

$$\begin{aligned}
\rho^m(\boldsymbol{x}, t) &= \sum_s q_s \int N_s(\boldsymbol{x}, \mathbf{v}, t)dv \\
\boldsymbol{J}^m(\boldsymbol{x}, t) &= \sum_s q_s \int vN_s(\boldsymbol{x}, \mathbf{v}, t)dv
\end{aligned}$$

Differentiating N_s with respect to time:

$$\frac{\partial N_s}{\partial t} = \sum_{i=1}^{N_0}\left[\frac{\partial}{\partial t}\delta(\boldsymbol{x} - \boldsymbol{X}_i)\right]\delta(\mathbf{v} - \boldsymbol{V}_i) + \sum_{i=1}^{N_0}\delta(\boldsymbol{x} - \boldsymbol{X}_i)\left[\frac{\partial}{\partial t}\delta(\mathbf{v} - \boldsymbol{V}_i)\right] \tag{1.4}$$

using the chain rule, for example $\frac{\partial}{\partial t}(\boldsymbol{x} - \boldsymbol{X}_i) = -\frac{d\boldsymbol{X}_i}{dt}.\frac{\partial}{\partial \boldsymbol{x}}f(\boldsymbol{x} - \boldsymbol{X}_i)$ and using

1.2 and 1.3, equation 1.4 becomes:

$$\frac{\partial N_s}{\partial t} = \sum_{i=1}^{N_0} = -\sum_{i=1}^{N_0} \boldsymbol{V}_i.\nabla_x \delta\left[\mathbf{x} - \mathbf{X}_i(t)\right] \delta\left[\mathbf{v} - \mathbf{V}_i(t)\right] - \sum_{i=1}^{N_0} \boldsymbol{F}_i.\nabla_x \delta\left[\mathbf{x} - \mathbf{X}_i(t)\right] \delta\left[\mathbf{v} - \mathbf{V}_i(t)\right] \tag{1.5}$$

Using the relation $g(x)\delta(x - x_0) = g(x_0)\delta(x - x_0)$, inserting equation 1.4.1 yields the Klimontovich equation:

$$\frac{\partial N_s}{\partial t} + \mathbf{v}.\nabla N_s + \frac{q_s}{m_s}\left(\boldsymbol{E}^m + \mathbf{v} \times \boldsymbol{B}^m\right).\nabla_{\mathbf{v}} N_s = 0 \tag{1.6}$$

We have obtained a set of equations which in terms of classical mechanics, completely determines the system. The Klimontovich equation however involves the summation over every single particle in the system. While being an exact description of the system, the Klimontovich equation is too complex to perform any meaningful calculations with and useful only as a starting point from which to derive average properties.

A more useful measure of the system is to consider a smooth function that yields the number of particles found in a volume $\Delta\mathbf{x}\Delta\mathbf{v}$ of phase space. Suppose we are interested in long range electric and magnetic fields that extend over ranges much larger than the inter-particle spacing. A volume of configuration space $\Delta\mathbf{x}$ centred about $\mathbf{x}$ can be chosen. The number of particles in that volume with velocities falling within a range $\mathbf{v} + \Delta\mathbf{v}$ can be normalised and the result is the distribution function, $f_s(\mathbf{x}, \mathbf{v}, t)$. The evolution of this function with time will be in good agreement with the ensemble average of the density function. The spikey effects due to the discrete nature of the particles can be decoupled using the definitions:

$$\begin{aligned} N_s(\mathbf{x}, \mathbf{v}, t) &= f_s(\mathbf{x}, \mathbf{v}, t) + \delta f_s(\mathbf{x}, \mathbf{v}, t) \\ \mathbf{E}^m(\mathbf{x}, \mathbf{v}, t) &= \mathbf{E}(\mathbf{x}, \mathbf{v}, t) + \delta\mathbf{E}(\mathbf{x}, \mathbf{v}, t) \\ \mathbf{B}^m(\mathbf{x}, \mathbf{v}, t) &= \mathbf{B}(\mathbf{x}, \mathbf{v}, t) + \delta\mathbf{B}(\mathbf{x}, \mathbf{v}, t) \end{aligned}$$

Where $\mathbf{E}$ and $\mathbf{B}$ are the ensemble averages of $\mathbf{E}^m$ and $\mathbf{B}^m$ respectively. Inserting these into the Klimontovich equation (1.6) gives the plasma kinetic equation:

$$\frac{\partial f_s}{\partial t} + \mathbf{v}.\nabla_{\mathbf{x}} f_s + \frac{q_s}{m_s}\left(\boldsymbol{E} + \mathbf{v} \times \boldsymbol{B}\right).\nabla_{\mathbf{v}} f_s = -\frac{q_s}{m_s}\left\langle(\delta\mathbf{E} + \frac{v}{c} \times \delta\mathbf{B}).\nabla_{\mathbf{v}}\delta N_s\right\rangle \tag{1.7}$$

The terms on the left of equation 1.7 vary smoothly in phase space containing collective effects, while the terms on the right is the ensemble average of spiky terms that arise due collisions and individual particle correlations. Dropping these terms yields Vlasov's equation:

$$\frac{\partial f_s}{\partial t} + \boldsymbol{v}.\nabla f_s + \frac{q_s}{m_s}(\boldsymbol{E} + \boldsymbol{v} \times \boldsymbol{B}).\nabla_{\boldsymbol{v}} f_s = 0 \tag{1.8}$$

For a relativistic plasma, define $\mathbf{u} = \mathbf{v}\gamma$ where γ is the Lorentz factor which can be defined in terms of $\mathbf{u}$,

$$\gamma = \sqrt{1 + \frac{|\boldsymbol{u}|^2}{c^2}}.$$

Defining γ this helps avoid divide by zero problems that could occur when γ is defined the usual way.

Vlasov's equation for a relativistic plasma is then:

$$\frac{\partial f_s}{\partial t} + \frac{\boldsymbol{u}}{\gamma}.\nabla f_s + \frac{q_s}{m_s}(\boldsymbol{E} + \frac{\boldsymbol{u}}{\gamma} \times \boldsymbol{B}).\nabla_{\boldsymbol{v}} f_s = 0 \tag{1.9}$$

The Vlasov equation, coupled with Maxwell's equations describes the evolution of the particle distribution function forced by self-consistent, ensemble averaged fields. While this model ignores individual particle interactions it will be shown that it has applicability to a range of astrophysical and laboratory plasmas.

1.5 Collisions in an Ionised Gas

1.5.1 Coulomb Collisions

Collisions between neutral species are characterised by close range, large angle deflections as particles enter a proximity of the order of the atomic radius of each other. For these collisions the collision frequency is simply the average number of interactions between particles per unit time. In an ionised gas a particle can feel the influence of another particle through the Coulomb force over a much larger distance. The Coulomb force is an inverse square force given in SI units by:

$$\boldsymbol{F} = \frac{q_1 q_2}{4\pi\epsilon_0 r^2}\hat{r}$$

therefore while being much more common, interactions between particles in a

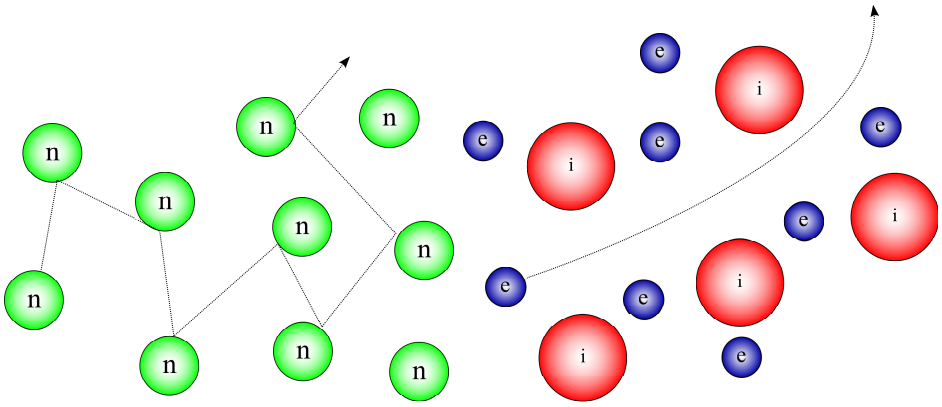

Figure 1.7: Typical test particle trajectories in a neutral fluid(left) and an ionised fluid(right). The collision time for a neutral gas is the time between collisions while in a plasma the collision time is defined as the time taken for the electron to be deflected through 90° due to the Coulomb forces from other particles

plasma result in the test particles only being deflected through a small angle. An illustration of collisions in a neutral fluid and a plasma are shown in figure 1.7.

To quantify these kind of collisions we will begin by considering binary Coulomb collisions between only two particles, in this case an electron encountering an ion. The geometry of this situation is illustrated in figure 1.8.

The electron has an initial velocity v_0, while the ion is heavier and moves much more slowly than the electron in thermodynamic equilibrium, so here the ion will be treated as if it is infinitely heavy and thus its trajectory is unchanged by the encounter. The encounter between the electron and ion can be characterised by the impact parameter b, which is the proximity the particles would have achieved had the electron not been deflected by their coulomb interaction. The velocity gained by the electron in the direction perpendicular to its unperturbed trajectory can be approximated by the integral of the perpendicular Coulomb forces($F_\perp$) on the electron travelling in a straight line at a distance b from the ion over time.

$$mv_\perp = \int_{-\infty}^{\infty} F_\perp(t)dt \tag{1.10}$$

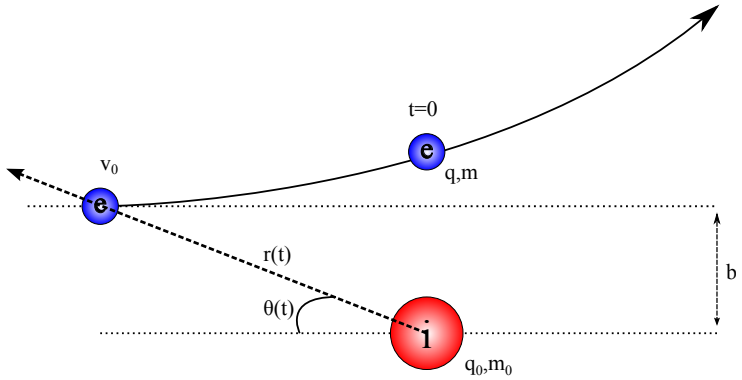

Figure 1.8: Schematic of a single Coulomb encounter

The scattering angle from a single encounter is assumed to be small such that $v_\perp \ll v_0$ so value of $F_\perp$ can be approximated using the electron's unperturbed trajectory, the dotted line in figure 1.8. Using Coulomb's law,

$$F_\perp = \frac{qq_0}{4\pi\epsilon_0 r^2}\sin\theta_e \tag{1.11}$$

the Coulomb force on the electron can be approximated by assuming it travels on an unperturbed trajectory thus $b = r\sin\theta_e$ and

$$F_\perp = \frac{qq_0}{4\pi\epsilon_0 b^2}\sin^3\theta_e \tag{1.12}$$

The total perpendicular velocity gained by the electron over all time is then, from equation 1.10

$$v_\perp = \frac{qq_0}{4\pi\epsilon_0 mb^2}\int_{-\infty}^{\infty}\sin^3\theta dt \tag{1.13}$$

The electron's position along the dotted line, $x = v_0 t$ and relates to θ through $x = -r\cos\theta$ and using $b = r\sin\theta$,

$$\frac{-b\cos\theta}{\sin\theta} = v_0 t$$

so

$$dt = \frac{p}{v_0}\frac{d\theta}{\sin^2\theta} \tag{1.14}$$

Using equation 1.13

$$\begin{aligned} v_\perp &= \frac{qq_0}{mv_0 b}\int_0^\pi \sin\theta d\theta \\ &= \frac{2qq_0}{mv_0 b} \end{aligned} \tag{1.15}$$

An impact parameter that causes the electron to gain perpendicular velocity equal to its parallel velocity, $v_\perp = v_0$, i.e. an impact parameter that causes a deflection of $\pi/4$ radians can be defined:

$$b_0 \equiv \frac{2qq_0}{mv_0^2} \tag{1.16}$$

Therefore each $b \leq b_0$ will lead to a large-angle deflection. The cross section for large-angle scattering by a single particle is given by πb_0^2. The frequency of these large-angle scatterings for an electron travelling through a medium of background particles is then:

$$\nu_L = \pi n_0 v_0 b_0^2 = \frac{4\pi n_0 q^2 q_0^2}{m^2 v_0^3}$$

As it travels through the plasma however, the electron is experiencing many more small angle deflections with an impact parameter $b \gg b_0$. The maximum impact parameter that causes a deflection can be set to the Debye length, since after this length charges are screened by particle motions. The frequency in which many of these small angle collisions lead to a deflection through $\pi/4$ radians can be derived by integrating over the range of impact parameters from b_0 to the Debye length(see, for example [15]). This gives the frequency of deflections through $\pi/4$ radians due to many small-angle collisions, or simply the collision frequency:

$$\nu_c = \frac{8\pi n_0 q^2 q_0^2 ln\Lambda}{m_e^2 v_0^3} \tag{1.17}$$

Equation 1.17 shows how the collision rate of a plasma differs to that of a neutral gas. Rather than being proportional to the particle's speed, the collision frequency is proportional to the inverse cube of the velocity of the test particle. While a particle with a higher velocity encounters particles more frequently, it does not experience a Coulomb force for as long and thus these collisions result in only a small angle of deflection.

1.5.2 Collision Operators

To include the effect collisions of the type described above on the distribution function described in section 1.4.1, terms must be added to the right hand side of Vlasov's equation:

$$\frac{\partial f_s}{\partial t} + \boldsymbol{v}.\nabla f_s + \frac{q_s}{m_s}(\boldsymbol{E} + \boldsymbol{v} \times \boldsymbol{B}).\nabla_{\boldsymbol{v}} f_s = \left(\frac{\partial f}{\partial t}\right)_c \tag{1.18}$$

Where the term $(\partial f/\partial t)_c$ is the rate of change of the distribution function due to collisions.

The Fokker-Planck Equation

For many years the Boltzmann collision integral was used for the collision term. This operator, being derived for a neutral gas assumed collisions were dominated by binary, short range interactions. This is not the case for in an ionised gas where collisions are dominated by weak, long-range interactions. The Fokker-Planck form of the collision operator was described by Chandrasekhar [16] by assuming that the motion of a particle undergoing Brownian motion is a Markov process then reducing it to a partial differential equation. It was then formulated for an inverse square force by Rosenbluth, MacDonald and Judd [17] for an arbitrary distribution function in terms of potentials in velocity space in the form:

$$\frac{1}{\Gamma}\left(\frac{\partial f_a}{\partial t}\right) = -\frac{\partial}{\partial \boldsymbol{v}}\left(f_a \frac{\partial h_a}{\partial \boldsymbol{v}}\right) + \frac{1}{2}\frac{\partial^2}{\partial \boldsymbol{v}\partial \boldsymbol{v}}\left(f_a \frac{\partial^2 g}{\partial \boldsymbol{v}\partial \boldsymbol{v}}\right)$$

The potentials are defined as:

$$\nabla_v^2 h_a = \sum_b \frac{m_a + m_b}{m_b} f_b(v)$$

and

$$\nabla_v^4 g = -8\pi \sum_b f_b(v)$$

and $\Gamma = 4\pi q_a^2 q_b^2 ln\Lambda/m_s$. This equation describes the change in the distribution of species a colliding with species b.

The Fokker-Planck formulation assumes that collisions are dominated by two-body, small angle deflections.

Bhatnagar-Gross-Krook

The Bhatnagar-Gross-Krook [18] model ignores the complex dynamics of particle-particle interactions and simply models the relaxation to an equilibrium, Maxwellian velocity distribution due to collisions. The operator is given by:

$$\left(\frac{\partial f}{\partial t}\right) = -\nu(f - f_0) \tag{1.19}$$

where ν is a collision frequency independent of velocity. The parameters of the Maxwellian distribution, f_0 are chosen by taking moments of f such that f_0 has the same density, momentum and energy. Collisions between differing species can also be included in this model in a conservative way [19].

This model can be improved through the use of a velocity dependent collision frequency. However this is not guaranteed to conserve momentum or energy due to the f_0 now being applied to f at differing rates in velocity space, particularly if f is far from equilibrium.

A method for implementing a Krook type collision operator with a velocity dependent collision frequency that is conservative will be described and its accuracy in laser-plasma regimes will be assessed in chapter 3.

1.5.3 Transport Coefficients

Since the electrons have a much smaller mass than the ions, they have higher typical speeds when the plasma is in thermal equilibrium. Because of their lower inertia, they are much more easily accelerated by external forces and as such are chiefly responsible for the transport of charge and energy through the plasma. The inclusion of collisions mean particles no longer travel uninhibited at their thermal velocity. The current and thermal flux can be written as [20]

$$\boldsymbol{J} = \sigma \boldsymbol{E} + \alpha \nabla T$$

$$\boldsymbol{q} = -\kappa \nabla T - \beta \boldsymbol{E}$$

Where the coefficients, κ and σ are the thermal and electrical conductivities respectively and α and β are thermoelectric transport coefficients.

The values for these coefficients can be derived using linear theory and the BGK collision operator [5], first assume a uniform plasma at rest in equi-

librium such that,

$$f_0 = f_m = n\left(\frac{m}{2\pi k_b T}\right)^{3/2} e^{-mv^2/2k_bT}$$

is perturbed by a weak and uniform electric field. This perturbs the plasma such that $f = f_0 + f_1$. Equation 1.18 with the Bhatnagar-Gross-Krook collision term with a collision frequency independent of velocity, ν_c, then reduces to

$$\frac{Ze\boldsymbol{E}}{m}.\frac{\partial f_0}{\partial \boldsymbol{v}} = -\nu_c f_1 \tag{1.20}$$

From Ohm's law, $\sigma\boldsymbol{E} = \boldsymbol{j}$ and $\boldsymbol{j}$ can be computed by integrating the distribution function and since the equilibrium distribution f_0 has no net current,

$$\boldsymbol{j} = Ze\int \boldsymbol{v} f_1 d\boldsymbol{v} \tag{1.21}$$

Integrating over velocity space and multiplying by $Ze\boldsymbol{v}$, equation 1.20 becomes

$$\nu_c \boldsymbol{j} = \frac{Z^2e^2}{k_bT}\boldsymbol{E}.\int \boldsymbol{v}\boldsymbol{v} f_M d\boldsymbol{v} \tag{1.22}$$

In 1D, where $\boldsymbol{E} = (E_x, 0, 0)$ and so $\boldsymbol{J} = (J_x, 0, 0)$. From equations 1.21 and 1.22 the electrical conductivity is obtained:

$$\sigma = \frac{nZ^2e^2}{m\nu_c} \tag{1.23}$$

The equilibrium distribution function for a plasma inhomogenous in space is

$$f_0(\boldsymbol{x}) = n(\boldsymbol{x})\left(\frac{m}{2\pi k_b T(\boldsymbol{x})}\right)^{3/2} e^{-mv^2/2k_BT}$$

The steady state, force-free solution of equation 1.18

$$\frac{\partial f_0}{\partial \boldsymbol{x}} = -\nu_c f_1 \tag{1.24}$$

For the thermal conductivity, assume constant pressure,

$$p = nk_bT.$$

so equation 1.24 becomes

$$f_0 \boldsymbol{v}.\nabla T \left(\frac{mv^2}{2k_b T^2} - \frac{5}{2T} \right) = -\nu_c f_1 \tag{1.25}$$

and the heat flux is given by

$$\boldsymbol{q} = \frac{1}{2} m \int v^2 \mathbf{v} f_1 d\mathbf{v}$$

multiplying equation 1.25 by $\frac{1}{2}mv^2\mathbf{v}$,

$$\nu_c \boldsymbol{q} = \frac{5m}{4T} \int v^2 \mathbf{v}\mathbf{v}.\nabla T f_0 d\mathbf{v} - \frac{m^2}{4k_b T^2} \int v^4 \mathbf{v}\mathbf{v}.\nabla T f_0 d\mathbf{v}$$

Since $T = \int 12mv^2 f dv$

$$\boldsymbol{q} = -\kappa \nabla T \tag{1.26}$$

Where the thermal conductivity, $\kappa = \frac{5nk_b^2 T}{2m\nu_c}$. For derivation using the velocity dependent form of the BGK collision operator see Struchtrup [21].

1.6 Collisional and Collisionless aspects of Laser-Plasma physics

In certain scenarios the collision time can be much longer than other timescales of interest.

The ratio of the collision frequency to the plasma frequency,

$$\frac{\nu_c}{\omega_{pe}}$$

where the collision frequency due to Spitzer [22] can be written

$$\nu_c \approx \frac{nZ^2 e^4}{2\pi \epsilon_0^2 m_e^2 v_0^3} ln\Lambda$$

and taking v_0 to be the thermal velocity $\sim \sqrt{k_B T_e / m_e}$ is then,

$$\frac{\nu_c}{\omega_{pe}} = \frac{ln\Lambda}{2\pi \lambda_D^3} = \frac{2ln\Lambda}{3N_D}$$

Plasma	$n_e(m^{-3})$	$T(K)$	N_D	ν_c/ω_{pe}
Solar Core	10^{32}	10^7	1	10^{-2}
Ionosphere	10^{12}	10^3	10^5	10^{-5}
Tokamak	10^{20}	10^8	10^8	10^{-7}
Solar Wind	10^6	10^5	10^{11}	10^{-11}
Interstellar Medium	10^5	10^4	10^{15}	10^{-15}
ICF	$10^{22} - 10^{32}$	$10^5 - 10^9$	$1 - 10^6$	$10^{-5} - 1$

Table 1.1: Typical Parameters of Laboratory and Astrophysical Plasmas

thus the importance of collisions is inversely proportional to N_D, the number of particles in a Debye sphere,

$$N_D = n\frac{4}{3}\pi\lambda_D^3 \quad \left(\propto \frac{T^{3/2}}{n^{1/2}}\right).$$

For hot and tenuous plasmas N_D becomes large such that the collision frequency is much smaller than the plasma frequency. Parameters for a few example plasmas are given in the table 1.1.

While these are approximate values, they give an idea of how the collisionality varies with density and temperature. The solar core is hot and dense. Confined by gravity, inter-particle encounters are common. Fusion of hydrogen to helium generates the Sun's energy. The ionosphere is part of the Earth's upper atmosphere, where particles are ionised by energetic particles and radiation from the Sun. The density here is low but so is the temperature, so large angle Coulomb deflections are more common. In a Tokamak the plasma is confined along helical field lines. Generally interactions with the EM fields are more important than inter-particle interactions, but collisions are important in understanding the transport of particles across field lines. The solar wind and interstellar medium are very sparse and may be assumed to be collisionless. Inertial confinement experiments range over a wide range of parameters. In an indirect drive scenario, the pre-plasma at the entrance to the Hohlraum has a ratio $\nu_c/\omega_{pe} \sim 10^{-5}$ while in the ablator shell this can be around $10^{-1} - 10^{-2}$ [23]. An overview of the physics of a high power laser interacting with matter is illustrated in figure 1.9

The values presented in table 1.1 show the wide range of conditions that must be considered in the physics of inertial confinement. Figure 1.9 shows an overview of the physical processes that are involved when a high intensity

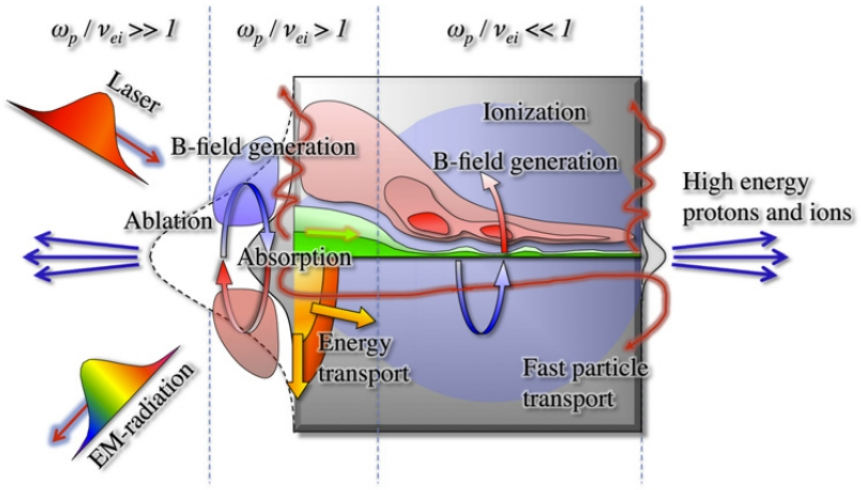

Figure 1.9: Summary of the physics of a high power laser hitting a target. Reproduced from Thomas et al. [23]

laser pulse interacts with matter and some characteristics of the plasma in each region. The region on the left corresponds to the region of ablated plasma. Here the plama is hot and tenuous and such that the plasma frequency is much greater than the typical collision frequency. For most studies in this region collisions may be neglected and the plasma is well described by the Vlasov equation. The next region covers the area where either the laser interacts with the plasma in direct drive and laser driven fast ignition schemes, or x-rays radiated from the inside of a hohlraum in indirect drive schemes. Modelling this region requires a method which is able to capture the coupling of laser energy to fast electron energy. This coupling however is still not fully understood with efficiencies derived from numerical and experimental work ranging from 10% up to 90% [24].

The region on the right of figure 1.9 is where the energetic particles propagating ahead of the heat front stream through through a background of cooler plasma. In electron driven fast ignition schemes the hot electron population can contribute to a considerable forward current density, around $10^{16} Am^{-2}$ [25]. This forward current($\boldsymbol{J}_f$) is balanced by a roughly equal return current($\boldsymbol{J}_r$) from the cool background population such that $J_f + J_r \equiv 0$. This return current response from the background plasma is highly collisional while the fast electron beam can is almost collisionless. In fast ignition studies modelling the transport through this region is key to estimating the coupling

efficiency between the ignitor pulse and the energy deposited in the hotspot. Divergence and filamentation of the electron beam reduce this efficiency, however methods involving applied z-pinches and resistivity gradients [26] exist to control these issues.

1.7 Summary

Some physical background and fundamental concepts have been introduced. Motivation for considering both collisional and collisionless models in aspects of laser-plasma experiments have been discussed. Simple transport coefficients have been derived from the Krook collision model to illustrate how they are related to the Vlasov-BGK equation. The issue of energy transport remains a pressing concern in both conventional inertial confinement fusion and fast and shock ignition and methods for modelling this will be discussed in subsequent chapters.

Chapter 2

Computer Simulation of The Vlasov-Maxwell System

2.1 Introduction

This chapter will discuss the computer simulation of the Vlasov-Maxwell system of equations, suitable for application when the ratio $\nu_{ei}/\omega_{pe} \ll 1$, or when the length of the simulation is far shorter than the mean free path. For collisionless plasmas, the Vlasov-Maxwell system provides an accurate way to model the evolution of the particle distribution functions over time. Due however to its nonlinearity, analytical solutions cannot be found for many important physical situations and the problem must then be solved numerically.

Approaches to Numerical Simulation

While efficient algorithms have been developed [27], the number of individual particles involved in most problems in plasma physics problems makes studying each individual particle unfeasible on current computing hardware. It's convenient to describe the position and velocity of a system of particles using a statistical approach considering the distribution of particles in space, velocity and time. The construction of such a distribution function is discussed in the introductory chapter.

A direct numerical solve of the Vlasov equation is a problem that requires significant computational effort. The distribution function requires the resolution of each of the phase space dimensions. Assuming the number of grid points in each dimension is n a computer simulation requires storage of n^d grid points, where d is the total number of dimensions in space and velocity space for each distribution function. For example in 3D, a modest simulation with 100 grid points in each x, y and z dimension in configuration space and with 64 grid points in each velocity dimension requires of the order 2.6×10^{11} grid points. Using double precision the memory requirement for a single distribution function is over 2000 gigabytes. In 2D however for equal resolution the requirement is only around 300 megabytes meaning that while formidable, higher resolution simulations are tractable on current high performance computing hardware.

Fluid models are derived by taking velocity moments of the distribution function and considering only these macroscopic quantities. Since only configuration space needs to be resolved, these methods can be used to simulate a plasma over a much longer time than is feasible for a kinetic model. This allows the simulation of hydrodynamic instabilities and magnetohydrodynamic phenomena. In terms of inertial confinement fusion, fluid codes are used to investigate Rayleigh-Taylor instabilities due to heterogenous heating of the capsule during the implosion phase [28]. The target designs at the National Ignition Facility(NIF) are based on results of fluid simulations using the LASNEX [29] code and the results themselves used to validate the model. Pure fluid models, while being highly efficient are unable to include detailed kinetics of energy absorption and transport.

Particle in Cell(PIC) methods have for many years been the preferred way to model kinetic problems in plasma physics. These methods are similar to n-body methods in molecular dynamics. However in PIC the Lorentz force on each particle is calculated by interpolating charges and currents to a fixed grid and updating Maxwell's equations using a finite difference method. The positions of the particles are then updated [30] using this force and the algorithm loops around again. Here the particles are actually macro-particles that represent many particles, as to make the simulation of system that may have a density of $\sim 10^{29} m^{-3}$ tractable. The more macro-particles that are used per cell therefore increases the accuracy of the method. Crucially, by using discrete particles that can inhabit any spatial co-ordinate the need for a

fixed velocity space grid is removed. In terms of the distribution function for a system of particles, the PIC method is a sampling of this distribution in phase space, illustrated in figure 2.1. PIC codes exhibit noise due to the fact the

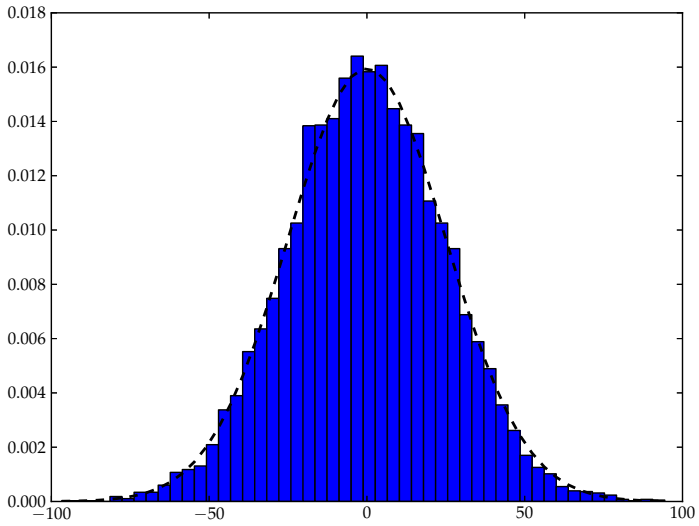

Figure 2.1: Histogram of the velocities of all particles in a cell between x and $x + \Delta x$.

macro particles can contain a large number of particles, which is proportional to $1/n_{pic}^2$, where n_{pic} is the number of macro-particles per cell.

In the limit of infinite particles per cell, the PIC method can be show to be analogous to solving Vlasov's equation. The choice then between a Vlasov code and a PIC code comes down to which one requires the least numerical effort for the same accuracy. Following the argument presented by Besse et al. [31] the ratio between the numerical effort(including both CPU and Memory requirement), between a Vlasov code and a PIC code will scale as:

$$\frac{N_{vlas}}{N_{part}},$$

which is the number of grid points in phase space over the total number of macro-particles in a corresponding particle in cell code. Here it is assumed that the total computational cost of updating the self-consistent fields is the

same in both schemes, however this is not strictly true, and is dependent on the choice of interpolation scheme used in the PIC code.

The memory requirement for a Vlasov code is then the product of the number of points in each dimension in configuration and velocity space,

$$N_{vlas} = N_x^{nd_x} N_v^{nd_v}$$

where nd_v and nd_x are the number of dimensions in velocity and configuration space respectively. For a particle in cell code the numerical effort can be written as

$$N_{part} = n_0 \Delta x^{nd_x} N_x^{nd_x}$$

where n_0 is the number of particles per cell. The graininess parameter due to discrete particles in a PIC code can be defined as:

$$g_{pic} = \frac{1}{n_0 \Delta x^{nd_x}}$$

Which is a measure of the numerical noise due to the finite number of particles used in a PIC simulation and is reduced by increasing the density of macro-particles. For a PIC simulation, N_{part} can be written

$$N_{part} = g_{pic}^{-1} N_x^{nd_x}$$

and the ratio is then.

$$\frac{N_{vlas}}{N_{part}} = g_{pic} (N_v)^{nd_v}$$

To capture kinetic effects such as wave-particle interactions g_{pic} is required to be as small as possible to resolve the distribution function in the high velocity tails where such interactions occur. The discrete nature of a particle code means that the distribution function can be poorly resolved in regions of low mass. A Vlasov code however resolves all of phase space and does not have this problem. For 1D1P problems, Vlasov codes are always preferred over PIC codes. For 2 dimensional problems it depends on the levels of noise that can be tolerated in the PIC code for the particular problem. For 3 dimensions PIC codes are always preferred.

In short-pulse laser-plasma studies, an incident laser beam can accelerate a fraction of the electron population to relativistic velocities. The generation and behaviour of these fast electrons requires fine-scale resolution in

the tails of the velocity distribution. These energetic populations may only represent a tiny fraction of the total electron population and would therefore be poorly resolved using a PIC code.

2.2 The Vlasov-Maxwell System

The Vlasov equation for a single species is essentially the Boltzmann equation where the collision term is zero and where the forcing term is the Lorentz force. For a multi-species plasma, the particles interact through the effect they themselves have on the electric and magnetic fields which must be calculated self-consistently using Maxwell's equations for moving charges. The Vlasov equation for a relativistic, multicomponent plasma is given by:

$$\frac{\partial f_j}{\partial t} + \frac{\boldsymbol{u}}{\gamma}.\nabla_{\boldsymbol{x}} f_j + \frac{q_j}{m_j}(\boldsymbol{E} + \frac{\boldsymbol{u}}{\gamma} \times \boldsymbol{B}).\nabla_{\boldsymbol{u}} f_j = 0 \tag{2.1}$$

Where the j subscript denoted the particle species. The fields must obey Maxwell's equations:

$$\nabla.\boldsymbol{E} = \frac{\rho(\boldsymbol{x}, t)}{\epsilon_0} \tag{2.2}$$

$$\nabla.\boldsymbol{B} = 0 \tag{2.3}$$

$$\nabla \times \boldsymbol{E} = \frac{\partial \boldsymbol{B}}{\partial t} \tag{2.4}$$

$$\nabla \times \boldsymbol{B} = \mu_0 \boldsymbol{J} + \epsilon_0 \mu_0 \frac{\partial \boldsymbol{E}}{\partial t} \tag{2.5}$$

Maxwell's equations must be solved with the Vlasov equation in a self-consistent way. Thus, he number density of each species is defined by its distribution function

$$n_j(\boldsymbol{x}) = \int f_j(\boldsymbol{x}, \boldsymbol{u}) d\boldsymbol{u} \tag{2.6}$$

And the charge and current density:

$$\rho(\boldsymbol{x}) = \sum_j q_j \int f_j(\boldsymbol{x}, \boldsymbol{u} d\boldsymbol{u}) \tag{2.7}$$

$$\boldsymbol{J}(\boldsymbol{x}) = \sum_j q_j \int \frac{\boldsymbol{u}}{\gamma} f_j(\boldsymbol{x}, \boldsymbol{u} d\boldsymbol{u}) \tag{2.8}$$

2.3 Numerical Schemes and the VALIS code

VALIS [32] is a code developed at Warwick by Tony Arber and Nathan Sircombe that solves the relativistic Vlasov-Maxwell system in up to 2 spatial and 2 velocity dimensions; a 2D2P system. In this geometry the components of the electric field, $\boldsymbol{E} = (E_x, E_y, 0)$ and equations 2.4 and 2.5 become

$$\frac{\partial E_x}{\partial t} = -J_x + \frac{\partial B_z}{\partial y} \tag{2.9}$$

$$\frac{\partial E_y}{\partial t} = -J_y - \frac{\partial B_z}{\partial x} \tag{2.10}$$

$$\frac{\partial B_z}{\partial t} = -\frac{\partial E_x}{\partial y} - \frac{\partial E_y}{\partial x} \tag{2.11}$$

with the electron density and current defined as

$$n_e = \int f_e d\boldsymbol{u} \tag{2.12}$$

$$J_{x,y} = -\int \frac{u_{x,y}}{\gamma} f_e d\boldsymbol{u} \tag{2.13}$$

There are no B_x, B_y components generated in this system so only B_z needs to be calculated.

2.3.1 Simulation Grid

The 2D2P model of the distribution function is described on a 4D phase-space grid. Valis uses a staggered mesh similar to a Yee mesh [33] commonly used in finite difference solvers. This is a fixed Eulerian grid running from x_{min} to x_{max} and y_{min} to y_{max} in the two spatial dimensions and $-u_{x_{max}}$ to $u_{x_{max}}$ in u_x and $-u_{y_{max}}$ to $u_{y_{max}}$ in u_y. The spatial and velocity grid cells are shown in figure 2.2.

When solving Maxwell's equations, the electric field depends on the first order spatial derivative of the magnetic field and the magnetic field depends on the first order spatial derivative of the electric field. When taking central differences on a standard grid this leads to a decoupling between the electric and magnetic fields which causes the checkerboard instability. The staggering of the distribution function, and components of the electric and magnetic field eliminate this problem. Two additional co-ordinate grids are defined to take

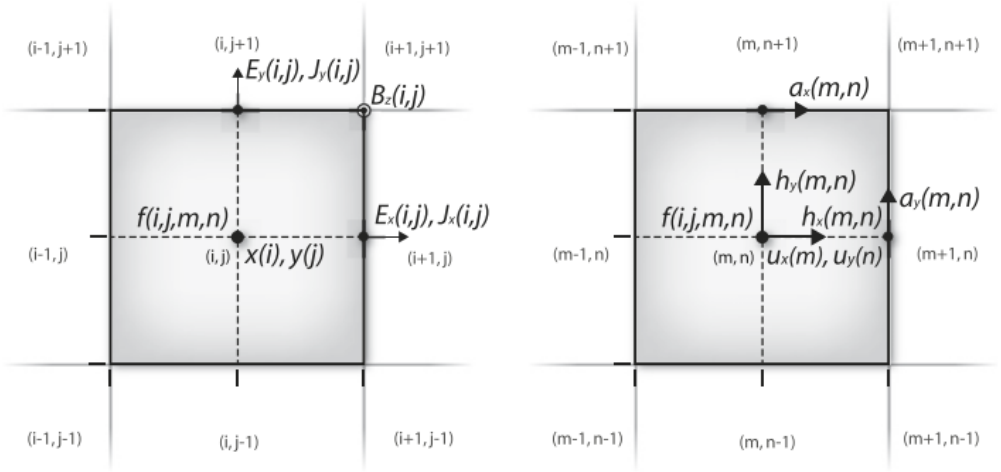

Figure 2.2: *Left* shows the spatial grid cell used in Valis. The distribution function is defined at the center with the fields defined at the cell boundaries. *Right* shows the momentum grid cell. The advection co-ordinates $a_{x,y}$ are defined at the cell boundaries and the distribution function, and $h_{x,y}$ are defined in the center [32].

into account the relativistic factor γ. For the spatial advections define

$$h_x(m,n) = \frac{u_x(m)}{\sqrt{1 + u_x^2(m) + u_y^2(n)}} \tag{2.14}$$

$$h_y(m,n) = \frac{u_y(m)}{\sqrt{1 + u_x^2(m) + u_y^2(n)}} \tag{2.15}$$

and for the momentum space advections:

$$a_x(m,n) = \frac{u_x(m)}{\sqrt{1 + u_x^2(m) + (\frac{u_y(n)+u_y(n+1)}{2})^2}} \tag{2.16}$$

$$a_y(m,n) = \frac{u_y(m)}{\sqrt{1 + u_y^2(m) + (\frac{u_x(m)+u_x(m+1)}{2})^2}} \tag{2.17}$$

Non-Uniform Velocity Grid

A disadvantage of solving Vlasov's equation directly is the requirement to advect areas of the distribution function that have little or no mass, for example in the high velocity tails where the distribution function is essentially zero. In the case where particles are accelerated by a high power laser, a fixed veloc-

ity grid must resolve velocity space up to these velocities at all times in the simulation. This is a major drawback of Vlasov codes. This problem can be somewhat diminished by concentrating grid points in areas where the distribution function has the most mass. This can also increase the accuracy of the numerical scheme at points where gradients in velocity space are the greatest. An illustration of a non-uniform velocity grid for a 2P distribution is shown in figure 2.3.

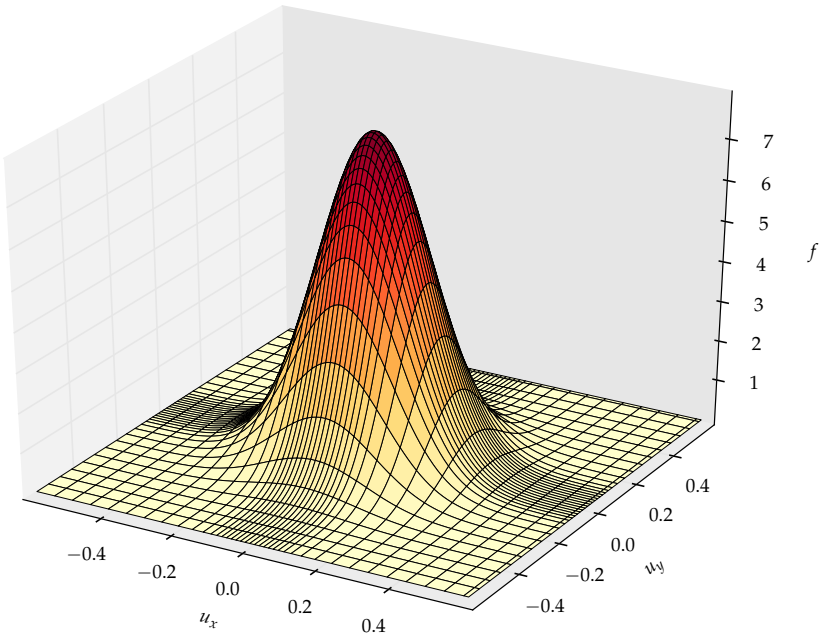

Figure 2.3: Non-Uniform grid spacing to increase resolution around $u_x = u_y = 0$

2.3.2 Updating the Distribution Function

A technique for updating the distribution function based on a Strang splitting method is described Cheng and Knorr [34]. They showed that the Vlasov equation can be split into a series of 1D advections. As an example, consider the 1D electrostatic Vlasov equation in dimensionless form:

$$\frac{\partial f}{\partial t} + v\frac{\partial f}{\partial x} - E\frac{\partial f}{\partial v} = 0 \tag{2.18}$$

Rather than solving 2.18 as a whole at each timestep, split the update into two steps. First solve

$$\frac{\partial f}{\partial t} + v\frac{\partial f}{\partial x} = 0 \tag{2.19}$$

for half a timestep, then solve

$$\frac{\partial f}{\partial t} + E\frac{\partial f}{\partial v} = 0 \tag{2.20}$$

for a full time step then complete the second half of the spatial advections. The result is then an approximation to equation 2.18. Using the same method, the distrubution function updates of the electromagnetic, relativistic 2D2P system solved by VALIS become the following 1D advections:

$$\frac{\partial f_e}{\partial t} + h_x\frac{\partial f_e}{\partial x} = 0 \tag{2.21}$$

$$\frac{\partial f_e}{\partial t} + h_y\frac{\partial f_e}{\partial y} = 0 \tag{2.22}$$

$$\frac{\partial f_e}{\partial t} + (E_x + a_y B_z)\frac{\partial f_e}{\partial u_x} = 0 \tag{2.23}$$

$$\frac{\partial f_e}{\partial t} + (E_y - a_x B_z)\frac{\partial f_e}{\partial u_y} = 0 \tag{2.24}$$

The advance of the distribution function from t to $t + \Delta t$ is then

1. x advection: advance 2.21 from t to $t + \Delta t/2$
2. y advection: advance 2.22 from t to $t + \Delta t/2$
3. u_x advection: advance 2.23 from t to $t + \Delta t/2$
4. u_y advection: advance 2.24 from t to $t + \Delta t$
5. u_x advection: advance 2.23 from $t + \Delta t/2$ to $t + \Delta t$
6. y advection: advance 2.22 from $t + \Delta t/2$ to $t + \Delta t$
7. x advection: advance 2.21 from $t + \Delta t/2$ to $t + \Delta t$

The x-y ordering is reversed on alternate timesteps to avoid any directional bias and the timestep size Δt is determined by the CFL condition such that $\Delta t = MIN(\Delta x/v^{max}, \Delta v/|E|_{max})$.

Carrying out the advections in this way yields a scheme which is accurate to second order in time. Thus all that is required to accurately advance

the distribution function is a method to accurately solve the 1D advection equations.

Advection Methods

Accurate numerical solutions to the 1D advection equation,

$$\frac{\partial a}{\partial t} + u\frac{\partial a}{\partial x} = 0 \tag{2.25}$$

are are often required in many fields of computational fluid dynamics. There are a number of different methods to carry out these advections, examples include predictor-corrector type schemes such as MacCormack's method [35], or interpolation schemes.

Interpolation Schemes The computational grid is shown in figure 2.4. Where $x_{j+1/2}$ is the boundary between the j^{th} and $j+1^{st}$ and $\Delta x = x_{i+1/2} - x_{i-1/2}$.

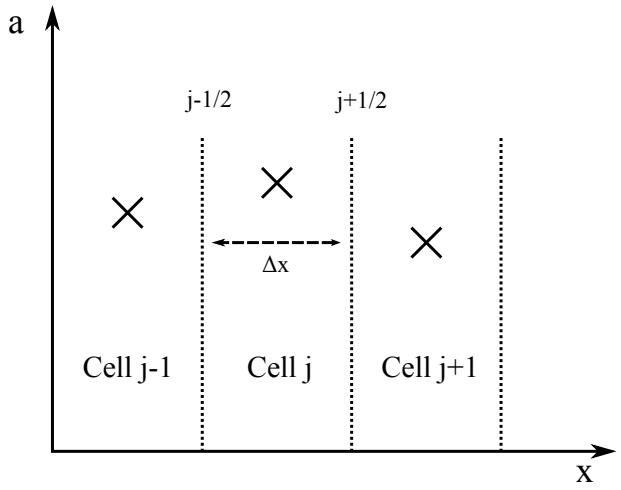

Figure 2.4: Computational grid with the function a defined at the centre of each cell

The value at the centre is the average of the solution between $x_{j-1/2}$ and $x_{j+1/2}$,

$$a_j^n = \frac{1}{\Delta x_j}\int_{x_{j-1/2}}^{x_{j+1/2}} a(x, t^n)dx$$

A piecewise interpolation method constructs a function ϕ across each individual cell which satisfies the condition

$$a_j^n = \frac{1}{\Delta x_j} \int_{x_{j-1/2}}^{x_j+1/2} \phi(x) dx$$

The solution at the centre of a cell at a time $t^{n+1} = t^n + \Delta t$, is then the value of the interpolated function at $\phi(x - u\Delta t)$,

$$a_j^{n+1} = \frac{1}{\Delta x_j} \int_{x_{j-1/2}}^{x_{j+1/2}} \phi(x - u\Delta t) dx$$

Since we are dealing with a probability distribution function, the interpolated function ϕ must meet certain requirements to keep the solution physical. The method must not introduce false extrema or accentuate existing extrema, doing so could allow $f < 0$ or $f > f_{max}$ which are not physical solutions for Vlasov's equation. If $f > f_{max}$ it would imply that particles with a velocity and position have joined and as such are joined at all times forwards and backwards. This would violate the reversibility of Vlasov's equation in time, a property shared by any purely advective equation. A negative probability is of course unphysical. VALIS uses the PPM [36] interpolation scheme to perform the advection updates. To illustrate the advantages of this method over others, first consider a simple linear interpolation scheme, the *Flux Balance Method*.

Flux Balance Method The interpolation function is piecewise linear and discontinuous at cell boundaries. The constructed linear function is illustrated in figure 2.5.

Setting $y = x/\Delta x$ (so that $y_i = i$), the method constructs a piecewise interpolation function $\phi(y)$ using the gradient between the values of U either side of the current cell:

$$D_i = (U_{i+1} - U_{i-1}) \tag{2.26}$$

$$\phi(y) = U_i + D_i y, \quad y \in [i - 1/2, i + 1/2] \tag{2.27}$$

Then the amount of fluid flowing (to the right) through the boundary

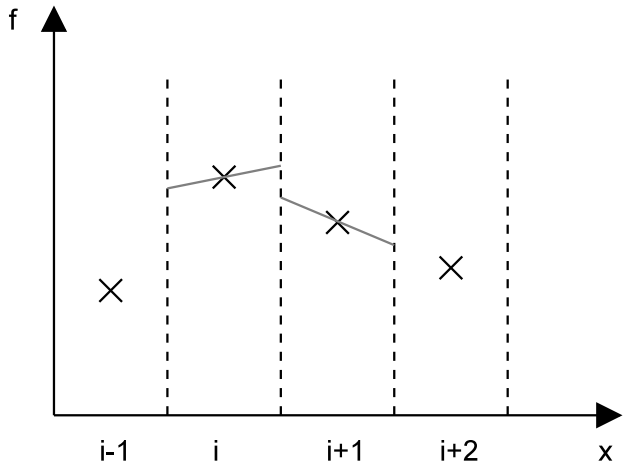

Figure 2.5: Linear Piecewise Function fitting. The interpolation function is centered at i and uses the gradient between the points $i-1$ and $i+1$. Here it is shown to introduce a false maxima at $i+1/2$

of the ith and $(i+1th)$ cell is computed,

$$\phi_{i+1/2} = \int_{i+1/2-\lambda}^{i+1/2} \phi(y)dy \tag{2.28}$$

Finally the value of U at the later time-step is computed using the difference of the flux in and out of the cell.

$$U_i^{n+1} = U_i^n - (\phi_{i+1/2} - \phi_{i-1/2}) \tag{2.29}$$

This method however is only second order accurate in space and is capable of introducing false maxima and minima into the distribution function as shown in figure 2.5.

Piecewise Parabolic Method From Gudonov's theorem it's known that any linear method that does not accentuate existing maxima and minima can, at best be first order accurate [37]. The method used in VALIS is the *Piecewise Parabolic Method*(PPM). It is an improvement on the previous scheme as the piecewise linear function is replaced by a piecewise parabolic function. The reconstruction is a quadratic function in the form:

$$f_r(x) = f_{r,i} = c_{0,i} + c_{1,i}(x - x_i) + c_{2,i}(x - x_i)^2$$

The reconstructed function $\bar{u}$ preserves the average across each cell i if

$$\frac{1}{\Delta x_i}\int_{x_{i-1/2}}^{x_{i+1/2}} f_r(x)dx = \bar{u}_i^n$$

Expressions for the function at the left and right hand boundaries are then:

$$u_{L,i} = f_{r,i}(x_{i-1/2}) = c_{0,i} - \frac{1}{2}\Delta x_i c_{1,i} + \frac{1}{4}\Delta x_i^2 c_{2,i}$$

$$u_{R,i} = f_{r,i}(x_{i+1/2}) = c_{0,i} + \frac{1}{2}\Delta x_i c_{1,i} + \frac{1}{4}\Delta x_i^2 c_{2,i}$$

Solving for each coefficient gives

$$\begin{aligned} c_{0,i} &= \bar{u}_i^n - \frac{1}{12}\Delta x_i^2 c_{2,i} \\ c_{1,i} &= \frac{u_{R,i} - u_{L,i}}{\Delta x_i} \\ c_{2,i} &= \frac{6}{\Delta x_i^2}\left(\frac{u_{R,i} + u_{L,i}}{2} - \bar{u}_i^n\right) \end{aligned}$$

1. Use a fourth order interpolation scheme to compute values of U at the cell boundaries(i.e., $U_{i+1/2}$ for each i. These values must be limited to ensure that a false maxima is not introduced, (i.e.,$U_{i+1/2} \in [U_i, U_{i+1}]$))

2. Generate $\phi(y)$ in each cell as a parabolic function passing through the boundary values which has the correct mean, i.e.,$\int_{i-1/2}^{i+1/2} \phi(y)dy = U_i$.

3. Limit ϕ in each cell such that if U_i is a local extremum, set $\phi = U_i$ across all the cell. If the interpolating function $\phi(y)$ achieves and extremum in the cell, reset one of the boundary values (making ϕ discontinuous there) so that ϕ is monotone and so that $d_y\phi = 0$ at the edge opposite to the resetting.

This method, through its use of cellwise limiters, does not introduce any false extrema into the distribution function. The interpolation scheme is third order accurate away from extrema and 1st order at extrema, due to setting $\phi = U_i$ in the cell if U_i is a local extrema.

2.3.3 Updating the Fields

The scheme to update the fields must be accurate, stable and scalable. Numerical schemes for solving Maxwell's equations can potentially suffer cumulative error in the solution of Poisson's equation or alter the dispersion relation. The scheme must avoid these and must do so without incurring significant computational cost.

A *Predictor Corrector* scheme is used in VALIS. In this scheme, the magnetic field is advanced from a time $k - 1/2$ to $k + 1/2$, then interpolating back to find $\boldsymbol{B}$ at time k. The currents are integrated onto the spatial grid at the cell faces. Here the integrated currents are denoted by $\tilde{J}$ and the number of cells in (x, y, u_x, u_y) is given by $(n_x, n_y, n_{u_x}, n_{u_y})$:

$$\tilde{J}_x^k(i,j) = -\sum_{m=1}^{n_{u_x}} \sum_{n=1}^{n_{u_y}} h_x(m,n) f_e^k(i,j,m,n) \Delta u_x(m) \Delta u_y(n) \tag{2.30}$$

$$\tilde{J}_y^k(i,j) = -\sum_{m=1}^{n_{u_x}} \sum_{n=1}^{n_{u_y}} h_y(m,n) f_e^k(i,j,m,n) \Delta u_x(m) \Delta u_y(n) \tag{2.31}$$

In the Yee mesh used in VALIS, the currents are required at the cell faces, so linear interpolation is applied:

$$J_x^k(i,j) = 0.5(\tilde{J}_x^k(i,j) + \tilde{J}_x^k(i+1,j)) \tag{2.32}$$

$$J_y^k(i,j) = 0.5(\tilde{J}_x^k(i,j) + \tilde{J}_x^k(i,j+1)) \tag{2.33}$$

The first order predictor for $E_{x,y}^{k+1/2}$ is then:

$$E_x^{k+1/2}(i,j) = E_x^k(i,j) + \frac{\Delta t}{2\Delta y}(B_z^k(i,j) - B_z^k(i,j-1)) - \frac{\Delta t}{2} J_x^k(i,j) \tag{2.34}$$

$$E_y^{k+1/2}(i,j) = E_y^k(i,j) + \frac{\Delta t}{2\Delta y}(B_z^k(i,j) - B_z^k(i-1,j)) - \frac{\Delta t}{2} J_y^k(i,j) \tag{2.35}$$

Now the distribution function can be advanced by a complete timestep via the PPM method described earlier using $B_z^{k+1/2}$ and $E_{x,y}^{k+1/2}$

Finally, apply a second order corrector to obtain electric field using time centred currents given by linearly interpolating between the current at

the previous timestep and the new timestep:

$$J_x^k(i,j) = 0.5(J_x^k(i,j) + J_x^{k+1}(i,j)) \tag{2.36}$$

$$J_y^k(i,j) = 0.5(J_y^k(i,j) + J_y^{k+1}(i,j)) \tag{2.37}$$

Where $J_{x,y}^{k+1}(i,j)$ is calculated using the updated distribution function at time k+1. Now $E_{x,y}$ can be advanced from k to k+1:

$$E_x^{k+1}(i,j) = E_x^k(i,j) + \frac{\Delta t}{\Delta y}(B_z^{k+1/2}(i,j) - B_z^{k+1/2}(i,j-1)) - \Delta t J_x^{k+1/2}(i,j) \tag{2.38}$$

$$E_y^{k+1}(i,j) = E_y^k(i,j) + \frac{\Delta t}{\Delta x}(B_z^{k+1/2}(i,j) - B_z^{k+1/2}(i-1,j)) - \Delta t J_y^{k+1/2}(i,j) \tag{2.39}$$

An illustration of the Valis algorithm is shown in figure 2.6.

For PIC(particle in cell) based codes, the charge density and current is often calculated by interpolating from the individual super-particles. While this scheme does satisfy charge conservation, it is known [38] however that the charge density and current does not satisfy the finite difference approximation of charge conservation as the system is advanced in time. As a result of this, these schemes do not satisfy Poisson's equation as time is advanced, even if it is imposed at the start. The solution to this problem for PIC schemes is to calculate the charge that crosses the cell boundaries, rather than interpolating from the particles [38]. This also all applies to direct Vlasov solvers. If the charge and current densities are calculated at grid points by integrating the distribution function and interpolating, there is no guarantee that charge conservation or Poisson's equation is satisfied. If the current used in the field update is calculated using the flux through the edges of each computational cell, these fluxes are exactly those used to update the distribution function, so they must satisfy the finite difference version of the finite difference equation and therefore must satisfy Poisson's equation to machine precision.

Fortunately the *PPM* method used in the 1D advections of the distribution calculates the flux of the distribution function through the edges of each of the computational cells. This data can be recycled and used in the *Predictor Corrector* approach.

So the time-centered currents given by equations 2.36 and 2.37 can be replaced by integrating the fluxes through the cell faces and used to calculate

the average current over the timestep. For each cell (i,j), $J_{x,y}^{k+1/2}$ is defined as:

$$J_x^{k+1/2}(i,j) = -\frac{1}{\Delta t}\sum_{m=1}^{n_{u_x}}\sum_{n=1}^{n_{u_y}} h_x(m,n)[\Delta t \phi_x^{k+1}(i,j,m,n)]\Delta u_x(m)\Delta u_y(n) \tag{2.40}$$

$$J_y^{k+1/2}(i,j) = -\frac{1}{\Delta t}\sum_{m=1}^{n_{u_x}}\sum_{n=1}^{n_{u_y}} h_y(m,n)[\Delta t \phi_y^{k+1}(i,j,m,n)]\Delta u_x(m)\Delta u_y(n) \tag{2.41}$$

where $\phi_{x,y}^{k+1}$ (i,j,m,n) is the flux through the positive direction cell boundary for cell (i,j,m,n), as calculated in the PPM advection scheme during the advance of the distribution function from k to k+1. By performing a corrector step using the exact currents from the advection, VALIS ensures that Poisson's equation is satisfied to machine precision, without any additional computational cost.

The field updates in Valis are fully explicit and require the time step to resolve the plasma period for electrostatic simulations and the minimum of the plasma period and $\Delta x/c$ for electromagnetic simulations. This explicit advance simplifies the domain decomposition process and does not require a matrix inversion. Vlasov-Fokker-Planck codes have been developed [25, 39, 40] however that update the electric and magnetic fields implicitly [41]. Implicit field updates codes allow simulation over much longer timescales but preclude the resolution of plasma oscillations and the growth of fast unstable modes.

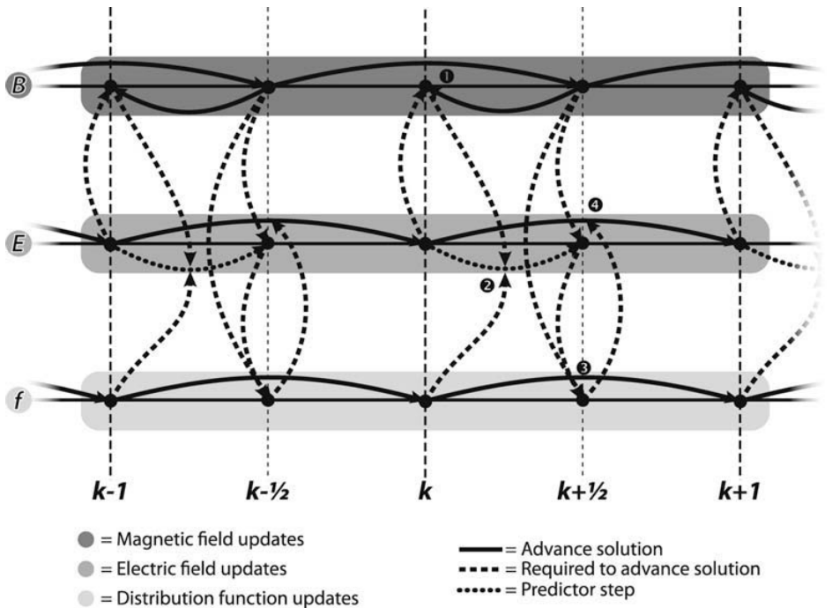

Figure 2.6: The Predictor Corrector approach used in Valis. This image is reproduced from Sircombe [32]

2.4 Normalisation

VALIS uses normalised units to avoid having to deal with numerical issues when dealing with extremely large and small numbers. The difference of various quantities involved in a laser-plasma simulation can be many orders of magnitude in SI units, for example:

$$m_e = 9.1 \times 10^{-31} kg$$
$$c = 3 \times 10^{8} ms^{-1}$$

By normalising, we choose a system of units where typical quantities are equal to 1. In Valis, masses are normalised to the electron mass, velocity to the speed of light, time to the plasma frequency and distance to the Debye length. Other units are then derived from these quantities. Table 2.1 shows all the normalised units used in Valis, where the units with marked with a tilde are normalised quantities and those without are in SI units.

However, for non-relativistic, electro-static simulations velocity is normalised to the thermal velocity, $v_0 = \sqrt{\frac{k_B T_0}{m_0}}$, where the normalising tempera-

Mass	$m = m_0\tilde{m}$	$m_0 = m_e$
Velocity	$v = v_0\tilde{v}$	$v_0 = c$
Distance	$x = x_0\tilde{x}$	$x_0 = \frac{v_0}{\omega_{pe}}$
Time	$t = t_0\tilde{t}$	$t_0 = \frac{1}{\omega_{pe}}$
Temperature	$T = T_0\tilde{T}$	$T_0 = \frac{m_0 c^2}{k_B}$
Electric Field	$E = E_0\tilde{E}$	$E_0 = \frac{\omega_{pe} v_0 m_e}{e}$
Magnetic Field	$B = B_0\tilde{B}$	$B_0 = \frac{\omega_{pe} m_e}{e}$

Table 2.1: Normalisations used in Valis

ture is specified manually. The normalising density is also specified manually, but is only used in the collision module.

2.5 Parallelisation Using MPI

2.5.1 Domain Decomposition

VALIS is parallelised using a domain decomposition scheme and uses the MPI API [42] to communicate between each compute node. It is parallel in each dimension of the 4D phase space and options exist to restrict parallelism to any number of dimensions. Inter-process communication is achieved by adjacent processes exchanging ghost cells at the beginning of each time-step. The storage for the local chunk is `nx+4` as each process receives the grid points `-2:0` from their left neighbour's `nx-2:nx` cells. Each process then updates its chunk of the distribution function from 1 to nx using the PPM method. An illustration of a 1D1P example, where the domain is parallel only in the x direction is shown in figure 2.7.

Decomposition in velocity space is implemented generally in the same way. Boundary conditions however can make things a little less straightforward and require non-nearest neighbour communication. These cases will be discussed in the next section.

2.5.2 Synchronisation and Non-Blocking Communication

VALIS implements a non-blocking communication method that allows each process to make its data available to the next process, then continue computing up until the point where it requires data from another process. In other words,

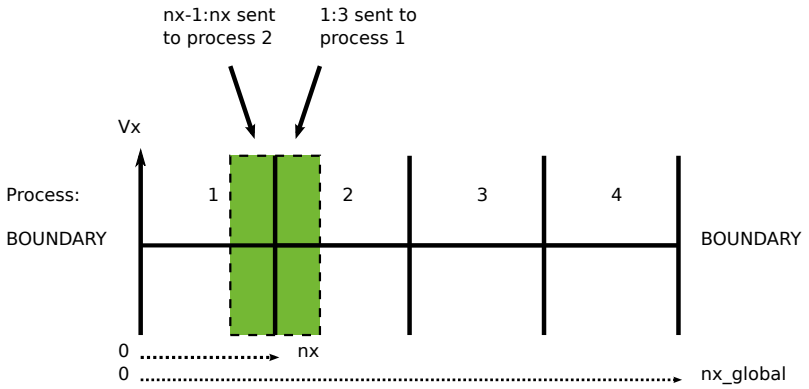

Figure 2.7: Illustration of the domain decomposition used in VALIS. Each process stores a chunk, `nx` of the total number of grid points in x, `nx_global`. The storage for the local chunk is `nx+4` as each process receives the grid points `-2:0` and `nx+1:nx+3` from their left and right neighbours respectively at the beginning of each time step.

when one process calls a subroutine to receive data it does not have to wait for another process to call a subroutine to send data before it continues execution. By doing this, the processes need only synchronise once at the end of the boundary exchange routines.

2.5.3 File IO

The output is handled using the MPIIO API which allows each process to write to a file without having to gather all the data on a single process. The output is in unformatted boundary with a custom file structure. Each block of data is preceded by a header containing information about its size, shape and name etc. Readers for the `.valis` are available for IDL, ViSiT and Python.

2.5.4 Boundary Conditions

Since VALIS solves Vlasov's equation on a discrete grid using a computer with finite resources, the extent of the domain must also be finite.

Periodic Periodic boundary conditions are a way of simulating an infinitely large domain on a finite size grid. Here the `x_min` and `x_max` are connected as if they were adjacent in space. A particle element with a velocity v_x moving into the wall appears at the other side of the domain with the same velocity.

Reflecting Reflecting boundary conditions invert the distribution function at the boundary so the value of $f(v_x)$ is copied into $f(-v_x)$ and vice versa. For the fields the boundary value simply set equal to the adjacent cell. For example, $E_x(0) = E_x(1)$ and $E_x(nx) = E_x(nx-1)$.

Laser A laser can be implemented at the boundary by simply driving components of the electric field at a given frequency. This boundary is valid on the condition that the density of the plasma at the boundary is lower than the critical density [43] , where $n_{crit}[cm^{-3}] = 1.1^{21}\left(\frac{1\mu m}{\lambda_L}\right)^2$

2.6 Numerical Tests

2.6.1 Landau Damping

Linear Landau damping of a Langmuir wave is a problem that is able to test a number of features of a Vlasov code. The electron distribution function is initialised with a density perturbation in configuration space. The advections then lead to a perturbed velocity distribution function, f_1, which varies as $f_1 \sim e^{ikvt}$. Hence there comes a time when the effective wavelength of this perturbed velocity distribution is equal to twice the grid spacing. This filamentation needs to be dissipated in a physically consistent way, that does not introduce false maxima, or allow f to become negative. The Piecewise Parabolic Method does this by limiting the gradients inside each cell to ensure that if f is an extremum at one of the cell boundaries, it never exceeds it inside. In this case it uses a first order approximation where the interpolation function inside the cell is a horizontal line which is the average of both boundaries, thus dissipating the filamentation and ensuring increasing entropy.

For this test the initial distribution function for the electrons is:

$$f_e = (1 + \alpha\cos(kx))\exp(-v_e^2/2)/\sqrt{2\pi}$$

With the amplitude of the perturbation, $\alpha = 0.01$, and $k = 0.5$ with $L_x = 4\pi$. The velocity grid runs from $(-v_e^{max}, v_e^{max})$ where $v_e^{max} = 4.5$. The ions are stationary. Here the number of spatial grid points, N_x is fixed at 32 and the number of velocity grid points is varied as $N_v = 16, 32, 64$ and 128. The amplitude of the fundamental harmonic of the electric field is plotted against

time in figure 2.8.

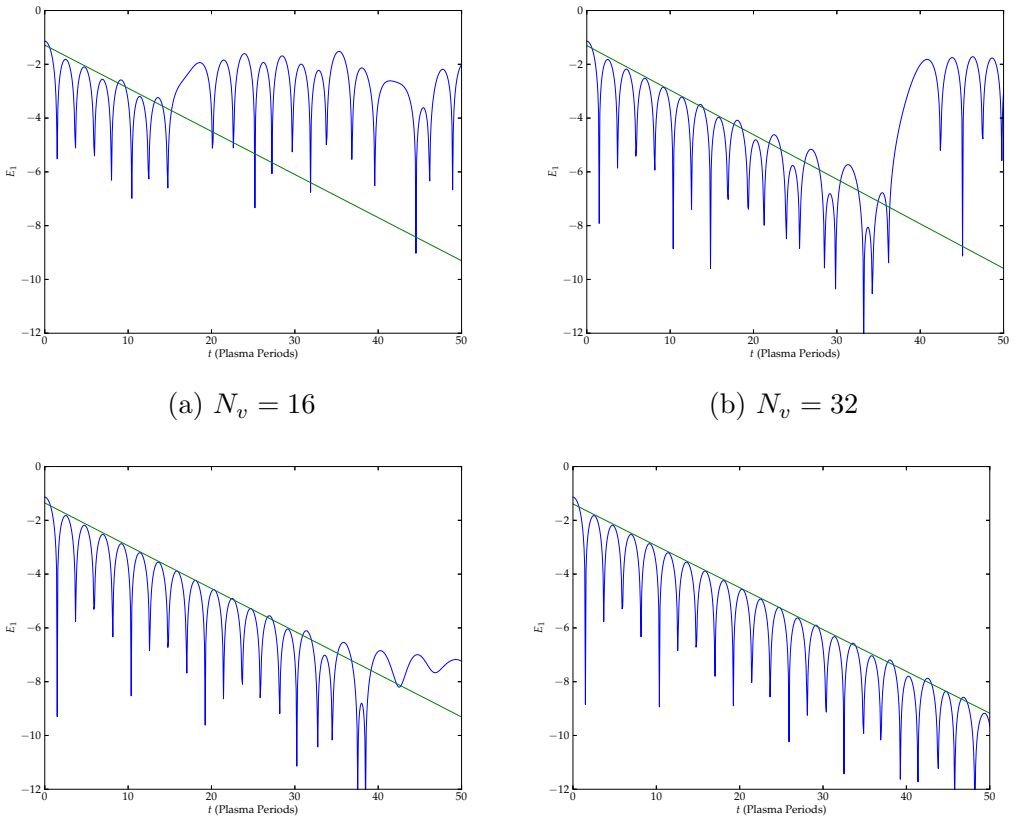

(a) $N_v = 16$ (b) $N_v = 32$

(c) $N_v = 64$ (d) $N_v = 128$

Figure 2.8: Linear Landau Damping of a Langmuir Wave

These initial conditions are identical to those in Arber and Vann [44], and the damping rate obtained using the linear dispersion relation, $\gamma = 0.153359$. A straight line is plotted through the peaks of $log_e(E_1)$, and its gradient yields the damping rate obtained numerically. Ignoring the electric field, the solution to Vlasov's equation is simply free streaming at each point in velocity space, i.e. $\partial f/\partial t = v\partial f/\partial x$. In this case each row in velocity space will be back in its initial condition after a time, $T_R = 2\pi/(k\Delta v)$. For small initial $\boldsymbol{E}$, the solution will show signs of recurrence at times close to T_R. An example of this is evident in figure 2.8 where N_v is small, hence Δv is large. In figure 2.8(a) $T_R = 22.34$ and in (b) $T_R = 44.68$. To avoid this interfering with calculations

N_v	γ	$\%Error$
16	0.160364	4.568
32	0.165704	8.05
64	0.159188	3.8
128	0.1556456	1.491

Table 2.2: Percentage Error in the Damping Rate for Various Resolutions in Velocity Space

of the damping rate, the line is fitted only through the peaks where $t < T_R/2$, which is different for each N_v. The percentage error in the damping rate for each resolution is shown in table 2.2.

2.7 Summary

An overview of numerical modelling methods was presented at the start of the chapter and the regimes in which fluid models and kinetic models are applicable was discussed. The particle-in-cell method of simulating kinetic physics was introduced as an alternative to solving Vlasov's equation. However due to the noise associated with particle-in-cell codes it was seen that for 1D1V problems it is always both more efficient and accurate to solve Vlasov's equation directly. In two dimensions the choice is dictated by the nature of the problem. The VALIS code for solving 2D2P Vlasov-Maxwell system was described.

Chapter 3

A Phenomenological Approach to Collisions: the Krook Model

3.1 Introduction

It's clear that a reduced collision operator that is accurate, stable and fast would be desirable, given the already complex Vlasov system. The Bhatnagar-Gross-Krook(BGK) [18] collision operator simply assumes that collisions act to relax the system to an equilibrium distribution function at the collisional rate:

$$\left(\frac{\partial f}{\partial t}\right)_c = -\nu(v)\,(f - F) \tag{3.1}$$

where ν is the velocity dependant collision frequency and F is the equilibrium distribution. The equilibrium distribution is a Maxwellian with the density, centre of mass velocity and temperature of f. This collision term is added to the right hand side of the Vlasov equation. After this point, the Vlasov equation with a collision operator shall be referred to as the Boltzmann equation.

A solution to the Boltzmann equation must be conservative, it must conserve particles, energy and momentum. For a homogenous plasma, it must also satisfy Boltzmann's H theorem which can be interpreted as stating that

the production of entropy:

$$S = -k \int f \log f dv$$

is always positive. This is true for the BGK operator since [21]

$$\begin{aligned} -k \int \log f.(-\nu(v)(f-F))dv &= -k \int \log f.(-\nu(v)(f-F))dv \\ &+ k \int \log F.(-\nu(v)(f-F))dv \\ &= k \int \nu(v) \log \frac{f}{F}(f-F)dv \geq 0 \end{aligned}$$

The equilibrium distribution distribution is the Maxwell-Boltzmann distribution since,

$$\nu(v)(f-F) = 0$$

when $f = F$. Furthermore the operator must maintain positive f. There are no physical parameters to F that could cause f to become negative. Here we use a velocity dependant collision frequency, which in the next section, will be shown to be implemented in a way that can conservers particles, energy and momentum.

The appeal of this operator in a kinetic model lies in its simplicity. Current Vlasov-Fokker-Planck codes [25] rely on the decomposing the electron distribution function into spherical harmonics. In the laser-plasma interaction region it is desirable to have an Eulerian direct Vlasov solver to include the laser. While a Fokker-Planck collision term has been implemented for an Eulerian Vlasov solver [45], this approach computationally demanding. A BGK model operator offers a computationally tractable method for including a collision operator in a direct Vlasov solver. In terms of the study of electron transport, the velocity dependence in the Krook collision operator would allow the simulation of effects due to differences in the mean free path, and indeed previous studies have shown this form to be in reasonable agreement with the Fokker-Planck collision term in certain scenarios [46]. However to be a viable alternative to full Vlasov-Fokker-Planck simulation, we need assess the accuracy of the Krook model and it must be able to produce at least qualitative agreement with classical transport coefficients.

3.2 Implementation

For electrons, collisions are considered both among themselves and with the ions. The operator is given by:

$$\left(\frac{\partial f_e}{\partial t}\right)_c = -\nu_{ee}(f_e - F_{e1}) - \nu_{ei}(f_e - F_{e2})$$

The collision frequencies are based on Coulomb collisions. Thus a collision is defined not by an individual interaction with another particle, but by a number of interactions that causes the test particle to be deflected by 90 degrees. The ion-electron collision frequency is therefore around 3 orders of magnitude smaller than that for electron-electron collisions. As such only ion-ion collisions are considered here. The operator for the ions is then:

$$\left(\frac{\partial f_i}{\partial t}\right)_c = -\nu_{ii}(f_i - F_i)$$

For stability, the updates to the distribution function are implemented implicitly. The time advance of the electron and ion distribution functions is then

$$f_e^{n+1} - f_e^n = \frac{-\Delta t \nu_{ee}}{1 + \Delta t(\nu_{ee} + \nu_{ei})}(f_e^n - F_{e1}) + \frac{-\Delta t \nu_{ei}}{1 + \Delta t(\nu_{ee} + \nu_{ei})}(f_e^n - F_{e2}) \quad (3.2)$$

$$f_i^{n+1} - f_i^n = \frac{-\Delta t \nu_{ii}}{1 + \Delta t \nu_{ii}}(f_i^n - F_i) \quad (3.3)$$

To conserve particle number, momentum and kinetic energy, we must ensure that the change in each remains zero. This can be imposed for each of the velocity moments over the time step.:

$$\int (f^{n+1} - f^n) v^m dv = 0 \ldots m = 0, 1, 2$$

To satisfy this, each of the terms on the right hand side of equations 3.2 and 3.3 must satisfy:

$$\int v^m \nu_{eff}(f^n - F) dv = 0 \ldots m = 0, 1, 2 \quad (3.4)$$

where, for electron-electron collisions

$$\nu_{eff} = \frac{\nu_{ee}}{1 + \Delta t(\nu_{ee} + \nu_{ei})}.$$

Equation 3.4 can be satisfied with the correct choice of F. For 1D, non-relativistic problems

$$F = \frac{a_1}{\sqrt{2\pi a_3}} exp\left(\frac{-(v_x - a_2)^2 - v_y^2}{2a_3}\right)$$

Define:

$$h(a_1, a_2, a_3) = \int \nu_{eff}(F - f)dv$$
$$h(a_1, a_2, a_3) = \int \nu_{eff} v(F - f)dv$$
$$h(a_1, a_2, a_3) = \int \nu_{eff} v^2(F - f)dv$$

Therefore we need to find a_j such that $h_m = 0$. Expand

$$h_m(\boldsymbol{a} + \delta\boldsymbol{a}) = h_m(\boldsymbol{a}) + \frac{\partial h_m}{\partial a_j}\delta a_j$$

then Newton-Rapheson gives:

$$\delta a_j g_{mj} = -h_m(\boldsymbol{a}) \tag{3.5}$$

where $g_{mj} = \frac{\partial h_m}{\partial a_j}$

We must find the elements of g_{mj} and then solve equation 3.5 to obtain δa_j.

Defining:

$$m\phi = \int \nu_{eff} F dv$$
$$vxn = \int \nu_{eff} v_x^n F dv$$

Expressions for the elements of g_{mj} for $f(v)$ distributed as a Maxwell-Boltzmann distribution are given below, the derivation of these elements is available in the appendix.

$$g_{1,1} = \frac{m\phi}{a_1} \tag{3.6}$$

$$g_{2,1} = \frac{vx1}{a_1} \tag{3.7}$$

$$g_{3,1} = \frac{vx2}{a_1} \tag{3.8}$$

$$g_{1,2} = \frac{vx1 - a_2 m\phi}{a_3} \tag{3.9}$$

$$g_{2,2} = \frac{vx2 - a_2 vx1}{a_3} \tag{3.10}$$

$$g_{3,2} = \frac{vx3 - a_2 vx2}{a_3} \tag{3.11}$$

$$g_{1,3} = \frac{-m\phi}{2a_3} + \frac{vx2 - 2a_2 vx1 + m\phi a_2^2}{2a_3^2} \tag{3.12}$$

$$g_{2,3} = \frac{-m\phi}{2a_3} + \frac{vx3 - 2a_2 vx2 + vx1 a_2^2}{2a_3^2} \tag{3.13}$$

$$g_{3,3} = \frac{-m\phi}{2a_3} + \frac{vx4 - 2a_2 vx3 + vx2 a_2^2}{2a_3^2} \tag{3.14}$$

To solve 3.5 we require $-h_m$. Defining:

$$\alpha_0 = \int \nu_{eff} f dv$$

$$\alpha_1 = \int \nu_{eff} v f dv$$

$$\alpha_2 = \int \nu_{eff} v^2 f dv$$

then

$$h_1 = m\phi - \alpha_0$$

$$h_2 = vx1 - \alpha_1$$

$$h_3 = vx2 - \alpha_2$$

α_i is not a function of F and therefore remains constant throughout the iterations and convergence is reached as h_m approaches zero.

3.2.1 Electron-Ion Collisions

While electron-electron and ion-ion collision operators must conserve momentum and energy this is not the case for electron-ion collision terms. For electron-ion collisions one expects there to be a mechanism for the electrons and ions to transfer energy between one another, meaning that eventually, these collisions will lead both species being in thermodynamic equilibrium. The electron-ion collision operator is:

$$\left(\frac{\partial f_e}{\partial t}\right)_c = \nu_{ei}(f - f_{mei})$$

where f_{mei} is a Maxwellian distribution with parameters derived from both the electron and ion distributions. Here the same approach is taken as in Greene [19] and the following parameters are used for f_{mei}

$$\boldsymbol{U}_{ei} = \frac{1}{2}(\boldsymbol{U}_e + \boldsymbol{U}_i) - \frac{1}{2}\beta(\boldsymbol{U}_e - \boldsymbol{U}_i) \tag{3.15}$$

$$\begin{aligned} T_{ei} = &\frac{m_i T_e + m_e T_i}{m_i + m_e} - \beta\frac{m_e}{m_i + m_e}(T_e - T_i) \\ &+ \frac{1}{6}(1-\beta)^2\frac{m_e m_i}{m_i + m_e}(\boldsymbol{U}_e - \boldsymbol{U}_i)^2 \\ &+ \frac{1}{12}(1+\beta)^2\frac{m_i - m_e}{m_i + m_e}m_e(\boldsymbol{U}_e - \boldsymbol{U}_i)^2 \end{aligned} \tag{3.16}$$

where β is a arbitrary constant [47]. Here we make the assumption that the ions are infinitely heavy, as such $\beta = -1$. Ion-electron collisions are ignored since the ion-electron collision time is smaller by the order of the ratio of the electron mass to the ion mass. Under these assumptions equations 3.15 and 3.16 reduce to:

$$\boldsymbol{U}_{ei} = \boldsymbol{U}_i \tag{3.17}$$

$$T_{ei} = T_e + \frac{1}{3}(\boldsymbol{U}_e - \boldsymbol{U}_i)^2 \tag{3.18}$$

Cast in this form it is easy to see that the electrons eventually relax to the same drift velocity as the ions. Also the temperature includes a contribution from the difference in relative drift velocities, leading to Ohmic heating

when currents are flowing through the plasma.

3.2.2 Relativistic Collisions

For relativistic collisions the equilibrium distribution is the Maxwell-Jüttner distribution, given(in 1D)by, [48]

$$f \sim \frac{n}{2K_1(\frac{1}{T})} exp\left(-\frac{\gamma}{T}\right)$$

where K_1 is the modified Bessel function. This distribution function ensures that no particles have a velocity exceeding c. A comparison of the Maxwell-Boltzmann and Maxwell-Jüttner distribution is shown in figure 3.1.

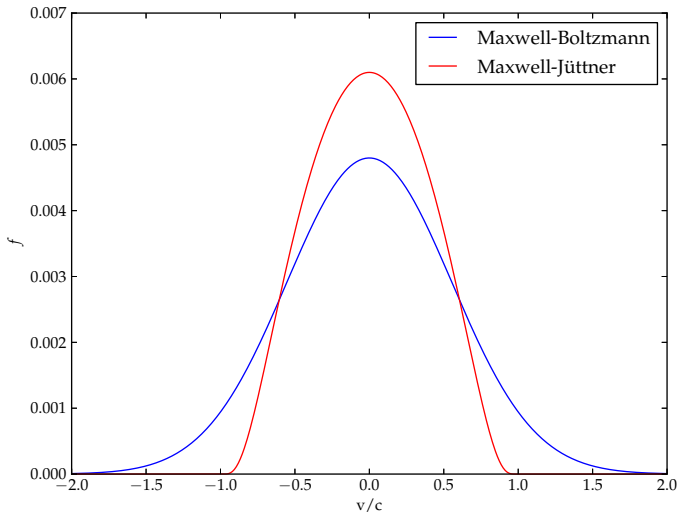

Figure 3.1: Plots of the Maxwell-Boltzmann and Maxwell-Jüttner distributions for a hot plasma. The relativistic distribution function does not allow particles with a velocity $\geq$ c.

Replacing the Maxwell-Boltzmann distribution, F in equation 3.5 with the Maxwell-Jüttner distribution yields a somewhat more complicated set of equations. Rather than finding the elements of the Jacobian analytically, they are computed numerically using a first order difference formula.

$$\frac{\partial h}{\partial a} = \frac{h(a) + h(a + \delta a)}{\delta a}$$

Care must be taken to choose a suitable value of δa to avoid zero gradients due to floating point limitations when using this method. Since the functions h_m require the integrations over velocity space, the numerical Jacobian is expensive to compute. For this reason, Broyden's method [49, 50] is used. This computes the Jacobian at the start and then uses a QR factorisation to avoid evaluating the finite difference Jacobian every iteration.

3.2.3 Quick Collisions

The collision operator detailed above can be approximated using a method that will be subsequently referred to as the quick operator. Instead of computing the Jacobian and iterating until convergence the centre of mass velocities and temperature of the target Maxwellian can be obtained by integrating the distribution function. This is the same technique used to generate the initial guesses for the fully convergent method. Mass conservation can be enforced by choosing,

$$a_1 = n\frac{m\phi}{\alpha_0}$$

This method requires significantly fewer computations that the fully conservative operator as it requires no iterations and integrations over velocity space need only to be computed once. While not guaranteeing conservation of momentum and energy, it will be shown that under certain conditions it is able to produce similar results to the full operator. On average for the electrical conductivity tests presented later in this chapter, the full operator took on average 4 iterations to converge. Each iteration requires three integrations over phase space and a matrix inversion to find elements a_n. Using this as a benchmark the quick operator on average requires 12 fewer integrations over phase space.

3.3 Collision Frequencies

The exact formula for the frequency of Coulomb collisions for a test particle α travelling through background Maxwellian field particles β is given by [51]

$$\nu_s^{\alpha|\beta} = (1 + m_\alpha/m_\beta)\psi(x^{\alpha|\beta})\nu_0^{\alpha|\beta}$$

where (in cgs units)

$$\nu_0^{\alpha|\beta} = 4\pi e_\alpha^2 e_\beta^2 \lambda_{\alpha\beta} n_\beta / m_\alpha^2 v_\alpha^3$$

$$x^{\alpha|\beta} = m_\beta v_\alpha / 2kT_\beta$$

$$\psi(x) = \frac{2}{\sqrt{\pi}} \int_0^x dt t^{1/2} e^{-t}$$

Limiting forms of this equation are tabulated in the NRL [52]. The slow test particle limit applies when $x^{\alpha|\beta} \ll 1$ and the fast when $x^{\alpha|\beta} \gg 1$. In the fast limit, the relevant collision frequencies are:

$$\nu_{slow}^{e|e} = 5.8 \times 10^{-6} T^{-3/2} n_e \lambda_{ee} \tag{3.19}$$

$$\nu_{slow}^{e|i} = 0.23 \mu^{3/2} T^{-3/2} n_i Z^2 \lambda_{ie} \tag{3.20}$$

$$\nu_{slow}^{i|i} = 6.8 \times 10^{-8} (2\mu)^{-1/2} T^{-3/2} n_i Z^4 \lambda_{ii} \tag{3.21}$$

and in the slow limit

$$\nu_{fast}^{e|e} = 7.7 \times 10^{-6} \epsilon^{-3/2} n_e \lambda_{ee} \tag{3.22}$$

$$\nu_{fast}^{e|i} = 3.9 \times 10^{-6} \epsilon^{-3/2} n_i Z^2 \lambda_{ei} \tag{3.23}$$

$$\nu_{fast}^{i|i} = 9.0 \times 10^{-8} \mu^{-1/2} T \epsilon^{-5/2} n_i Z^4 \lambda_{ii} \tag{3.24}$$

Following the treatment by Manheimer *e*t al [53], the fast and slow limit collision frequencies are analytically matched to apply to more general cases through:

$$\nu_{matched} = \frac{1}{\frac{1}{\nu_{fast}} + \frac{1}{\nu_{slow}}} \tag{3.25}$$

Giving, in SI units

$$\nu_{matched}^{e|e} = \frac{2\nu_e}{1 + 0.75(\frac{m_e v_e^2}{2k_B T_e})^{3/2}} \tag{3.26}$$

$$\nu_{matched}^{e|i} = \frac{Z\nu_e}{(\frac{m_e}{m_i})^{3/2} + \frac{1}{1.34}(\frac{m_e v_e^2}{2k_b T_e})^{3/2}} \tag{3.27}$$

$$\nu^{i|i}_{matched} = \frac{Z^4 \nu_i}{1 + \frac{1}{3.75}(\frac{m_i v^2}{2k_B T})^{3/2}} \tag{3.28}$$

where

$$\nu_e = \frac{3.63 \times 10^{-5}}{T_e^{3/2}} \tag{3.29}$$

$$\nu_i = \frac{6 \times 10^{-8} n_i \lambda_{ii}}{\mu^{1/2} T_i^{3/2}} \tag{3.30}$$

Some characterstic collision frequencies are shown in 3.2 and the collision frequencies integrated over velocity space as a function of the ionisation levels of carbon are shown in figure 3.3

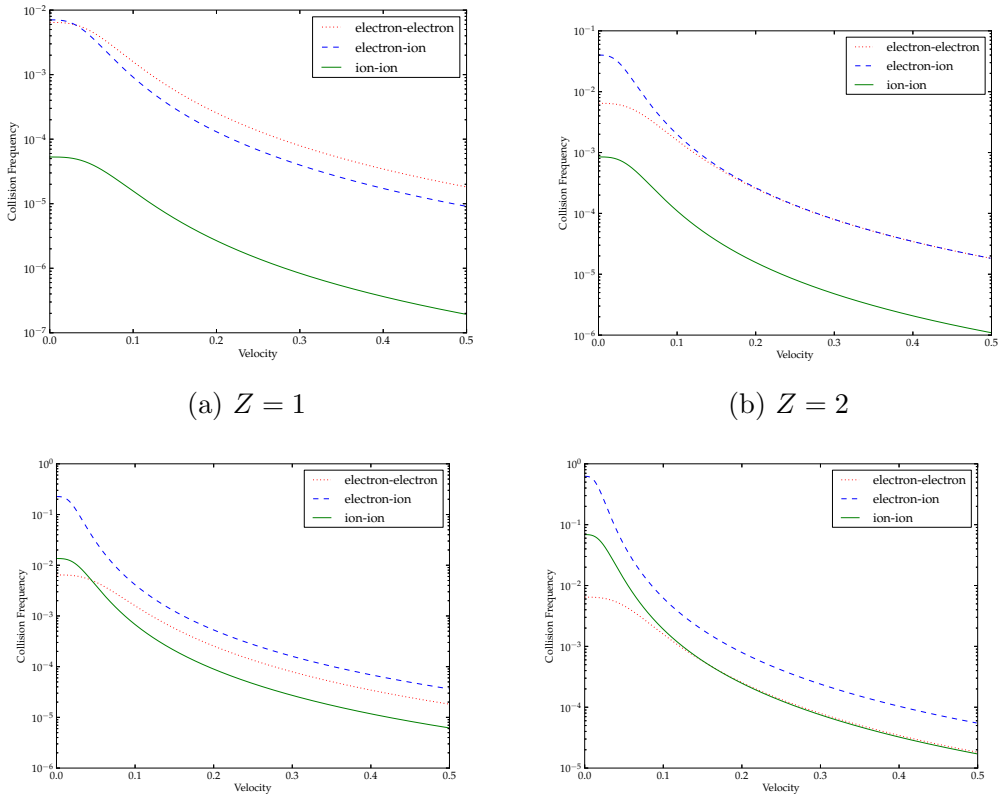

(a) $Z = 1$ (b) $Z = 2$

(c) $Z = 4$ (d) $Z = 6$

Figure 3.2: Characteristic collision frequencies as a function of velocity for various levels of background ionisation. Normalised units are used. The density is $1e^{29}m^{-3}$ and the temperature is 1keV.

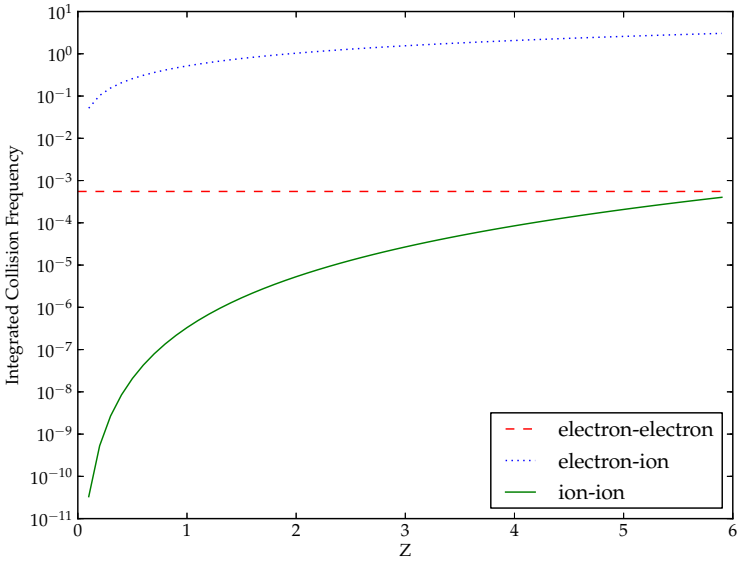

Figure 3.3: Collision frequencies integrated over velocity space as a function of the ionisation levels of carbon. Note that the collision frequency for Coulomb collisions goes to zero for neutral ions.

3.4 Heat Flux Normalisation

Modelling the non-local energy transport down steep temperature gradients is of vital importance to simulations of implosions of inertial confinement capsules. Methods of incorporating non-local energy transport into fluid models have been studied for many years [54–56]. In their efforts to derive such a method, Colombant, Manheimer and Goncharov developed a model [57–59] which uses a Krook collision term to estimate the heat flux in local and non-local limits. Using a similar method as used in the introductory chapter(section 1.5.3) to derive simple transport coefficients using a Krook operator with a velocity independent collision frequency, they derive the thermal conductivity produced by a Krook operator with a velocity dependent collision frequency. The ratio of this thermal conductivity is then compared with that predicted by Braginskii by linearising the Fokker-Planck equation and used to normalise the Krook term to ensure that it produces the same heat flux in the local limit. This factor, ζ is given by:

$$\zeta(Z) = \frac{0.64\gamma(Z)}{Z[Z_6(Z) - Z_4^2(Z)/Z_2(Z)]}$$

where

$$\gamma(Z) = 13.6\frac{Z + 0.24}{Z + 4.24}$$

$$Z_6(Z) - \frac{Z_4^2(Z)}{Z_2(Z)} = \frac{8.8}{Z} + \frac{12.5}{Z^2} + \frac{12.3}{Z^3} + \frac{5.1}{Z^4}$$

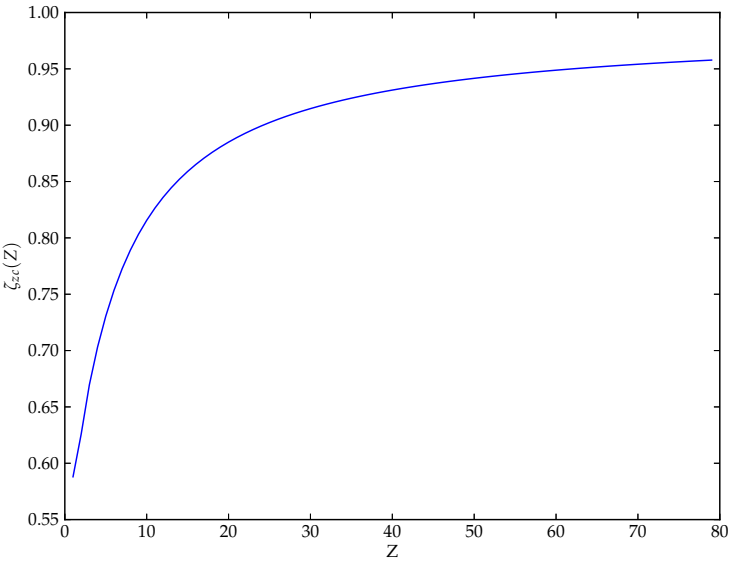

Figure 3.4: Plot of $\zeta(Z)$ for the zero current condition

3.5 Implementation Notes and Optimisation

The bulk of the computational cost in the implementation of the Krook operator is in the integration required to evaluate the functions $h_m(a_n)$. A costly element in their calculation is the evaluation of the collision frequency at every velocity grid point. Most of the factors of the collision frequency depend on space but are invariant in velocity space. For efficiency, the Coulomb logarithm and other factors are calculated outside of the velocity loop. The integrations

over phase space can also be sped up by ensuring the loops run in cache friendly indexing. When a processor loads data from main memory it fetches a chunk of contiguous values and places them into its cache which it can access orders of magnitude faster than in main memory. The integration loops are ordered such that subsequent loop iterations are more likely to depend on data already in the cache than main memory. In the column major ordering used by Fortran this means that the final index of an array should be varied on the inner-most loop.

3.6 Transport Test Results

The following test problems assess the ability of the BGK operator to reproduce the classical Transport coefficients of Spitzer [22] and Braginskii [60].

3.6.1 Electrical Conductivity

A DC background electric field is applied and the current produced is plotted as a function of time. The applied electric field produces ohmic heating in the electron population allowing testing over a range of temperatures. The current calculated by the code is then compared against that predicted using the resistivity predicted by Braginskii [60] and corrected by Epperlien and Haines [61]:

$$\eta_{Brag} = \frac{16\alpha_0(z)m_e}{3\pi e^2 n\tau_{brag}} \tag{3.31}$$

where $\alpha_0(z)$ is tabulated in Epperlien [61] and τ_{brag} is the electron-ion collision time. Following the approach by Braginskii,

$$\tau_{Brag} = \frac{3\pi^{3/2}\sqrt{m_e}\epsilon_0^2 T^{3/2}}{ne^4 Z\lambda_{ee}}$$

The current predicted using this resistivity can then be calculated simply as

$$J = \frac{E}{\eta_{Brag}}$$

These 1D simulations begin with a Z=1 plasma at 100eV with mobile ions. A constant background electric field is applied. Figure 3.5 shows the

current produced as a function of time. The Spitzer current is calculated using the temperature obtained from the code at each point in time. The collision frequencies used in the code are those analytically matched from the fast and slow limits. Figure 3.7 repeats 3.5 with $Z = 6$.

The gradients of the lines are due to ohmic heating, which happens over a larger timescale for smaller currents. The velocity grid runs from $-6 \times 10^6 ms^{-1}$ to $6 \times 10^6 ms^{-1}$. There is no discernible difference between the results obtained using 32 and 64 velocity grid points for both operators, with the full operator showing good agreement with the transport coefficients of Epperlien and Haines [61].

For the $Z = 6$ case, the code required a minimum of 32 grid points to obtain any reasonable results. At 128 grid points the full BGK operator shows excellent agreement with the transport coefficients.

3.6.2 Thermal Conductivity and Non-local Transport

The thermal flux as predicted by Braginskii can be written as

$$q_t = 3.2\gamma(z)q_f\lambda_{mfp} \tag{3.32}$$

where $q_f = nT^{3/2}$ is the free streaming flux. The thermal scale length $L = T/\nabla T$ and the mean free path for the electrons,

$$\lambda_{mfp} = \frac{\sqrt{3}1.57 \times 10^7 T_0^{3/2} T^2}{\sqrt{n} Z n Log(\Lambda)}$$

$Log(\Lambda)$ is the Coulomb logarithm.

The code is initialised with a 1-D temperature profile as:

$$T(x) = T_0(a - \frac{1}{2}(a-b)(\tanh(x - lc/wl) + 1))$$

where a and b are the fractions of T_0 of the hot and cold side respectively, c is the width of the profile and l is the length of the domain. This profile allows the accuracy of the BGK operator to be assessed over a few orders of magnitude of mean free path. The calculated heat flux normalised by the free streaming flux is plotted against scale length over mean free path. The scale length is a function of the temperature gradient and for a tanh profile each gradient occurs twice, thus the computed heat flux is multivalued corresponding to the gradients on each side of the curve.

Transport in the Local Limit

A gentle temperature gradient allows the operator to be assessed in regimes where Spitzer-Härm transport is valid. This is the case when the ratio of the electron mean free path to the temperature scale length($T/\Delta T$) is of the order of 10^{-3}. The following plots(number) correspond to a temperature profile from 10eV down to 9eV where the parameters of equation 3.6.2 are $T_0 = 10eV$, $a = 1$, $b = 0.9$, $c = 0.5$, $w = 0.1$, $l = 40,000\lambda_D$ and $Z = 4$. Results are shown for $\zeta(z)$ applied to ν_{ee}, ν_{ee} and ν_{ei}, and the Krook operator without heat flux normalisation. Figure 3.9 shows the deviation from Braginskii's predicted heat flux as a function of the number velocity space grid points computed by the Krook operator without any heat-flux normalisation. At low resolution the quick operator performs poorly, perhaps predictably given that energy

conservation is related to the resolution of the velocity distribution in this method. As the velocity space resolution is increased however both operators roughly converge to a deviation of about 43% of the Braginskii value.

However this normalisation must not come at the cost of the accuracy obtained in the previous section for the Spitzer electrical conductivity. Figures 3.10 and 3.11 show results for the quick and full operators respectively. It's seen that for both operators, applying ζ reduces the error in the thermal conductivity down to below 10%. This however comes at the cost of increasing the percentage error in the electrical conductivity calculations by an around order of magnitude for each operator. The results show the culprit to be applying ζ to the e-i operator. Restricting the application of ζ to the e-e operator is shown to increase the accuracy in the results for both the electrical and thermal conductivity.

Non-Local Transport

As the temperature gradient is increased the mean free path of the electrons can exceed the temperature scale length meaning that the classical transport coefficients are no longer valid. For this test the tanh temperature profile runs from 400eV down to 100eV. The plots in 3.12 can be read as so: the bottom right corresponds to the top of the *tanh* profile. Moving to the far left equates to the centre of the temperature gradient, the steepest point. The curve then moves back out which is the cooler part of the temperature profile. The points corresponding to the cold side of the profile are seen to exceed the value predicted by Braginskii due to the contribution of hot electrons that have streamed in from the hot part. The heat flux calculated in the hot side of the profile is depleted due to the loss of the high energy electrons to the cold side. This effect was described by Bell *e*t al [62] and their results are reproduced in figure 3.13. The results here are in qualitative agreement with those produced using the full Fokker-Planck collision term.

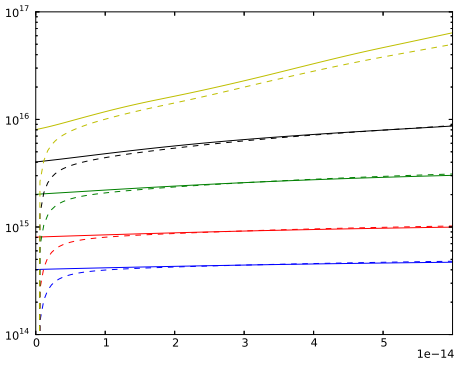

(a) $N_v = 16$, Quick Operator

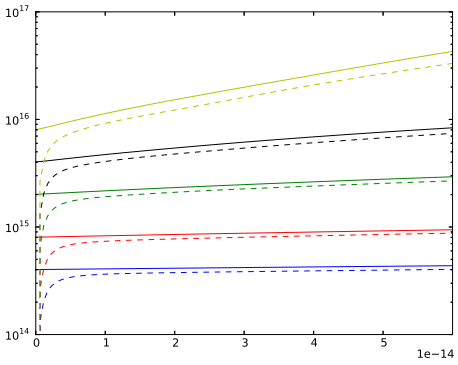

(b) $N_v = 16$, Full Operator

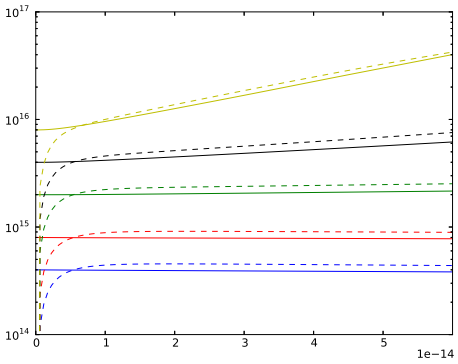

(c) $N_v = 32$, Quick Operator

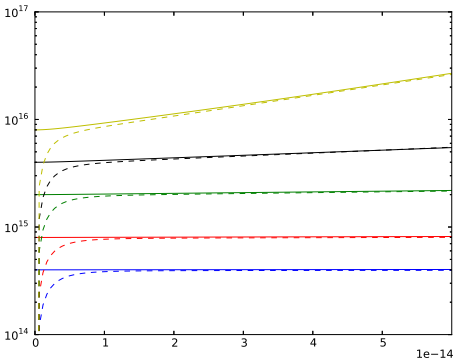

(d) $N_v = 32$, Full Operator

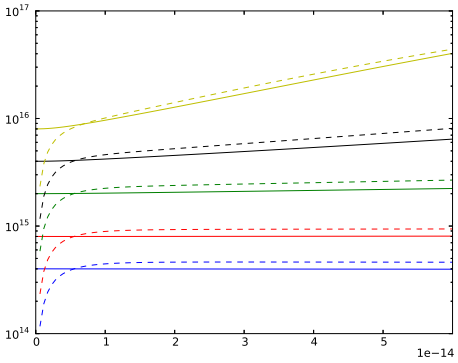

(e) $N_v = 64$, Quick Operator

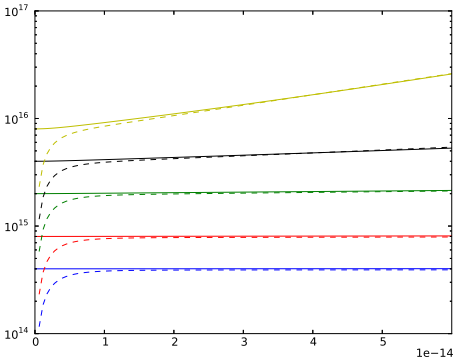

(f) $N_v = 64$, Full Operator

Figure 3.5: Plots of Current produced vs time using the quick(left) and full(right) BGK collision operators(Dashed) and the corresponding values calculated using transport coefficients(Solid) for external fields of: $2 \times 10^9 V/m$(Yellow), $10^9 V/m$(Black), $5 \times 10^8 V/m$(Green), $2 \times 10^8 V/m$(Red) and $10^8 V/m$(Blue) for a Z=1, Hydrogen plasma. The x-axis is time in seconds and the y-axis is current produced in amperes per square metre.

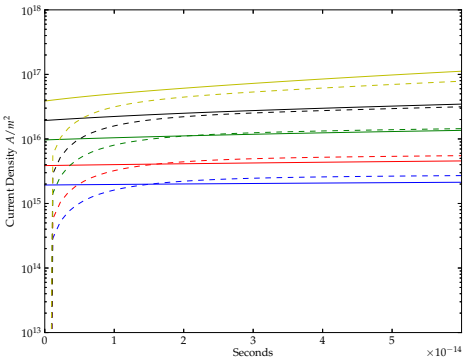

(a) $N_v = 32$, Quick Operator

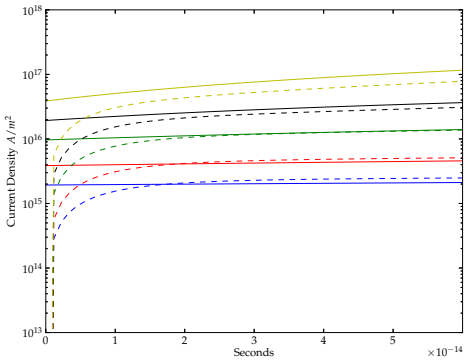

(b) $N_v = 32$, Full Operator

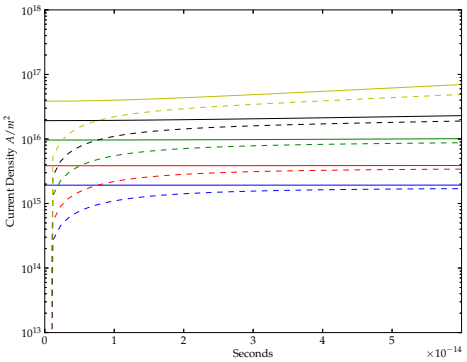

(c) $N_v = 64$, Quick Operator

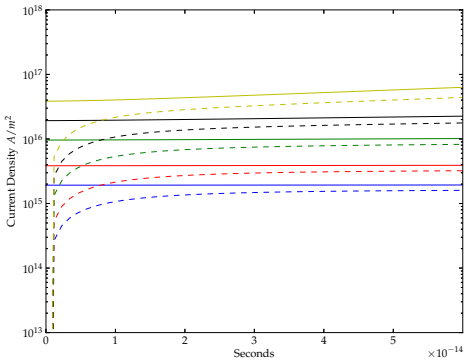

(d) $N_v = 64$, Full Operator

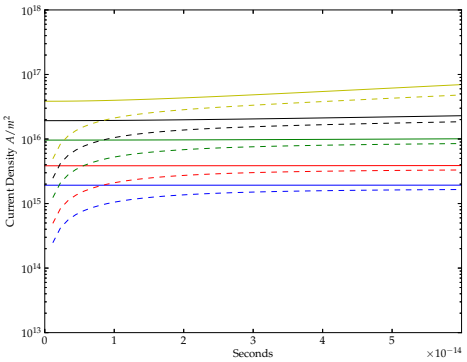

(e) $N_v = 128$, Quick Operator

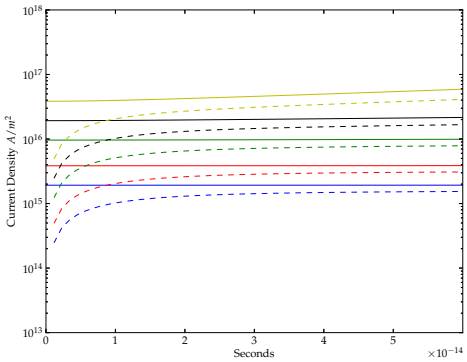

(f) $N_v = 128$, Full Operator

Figure 3.6: Plots of Current produced vs time using the quick(left) and full(right) BGK collision operators(Dashed) and the corresponding values calculated using transport coefficients(Solid) for external fields of: $2 \times 10^9 V/m$(Yellow), $10^9 V/m$(Black), $5 \times 10^8 V/m$(Green), $2 \times 10^8 V/m$(Red) and $10^8 V/m$(Blue) for a Z=4, Beryllium plasma. The x-axis is time in seconds and the y-axis is current produced in amperes per square metre.

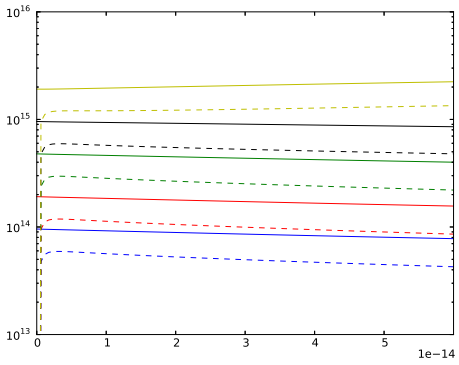

(a) $N_v = 32$, Quick Operator

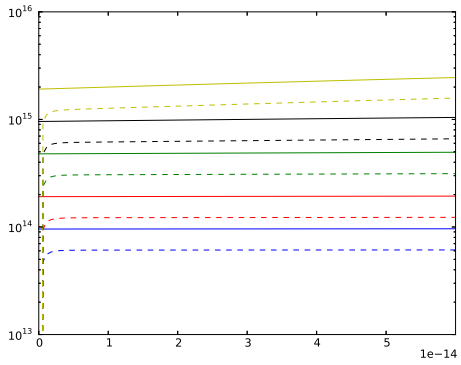

(b) $N_v = 32$, Full Operator

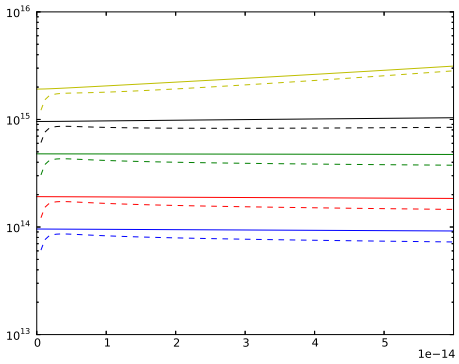

(c) $N_v = 64$, Quick Operator

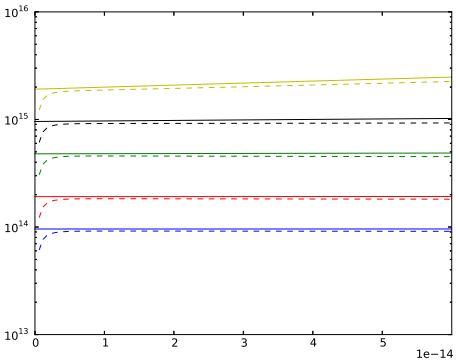

(d) $N_v = 64$, Full Operator

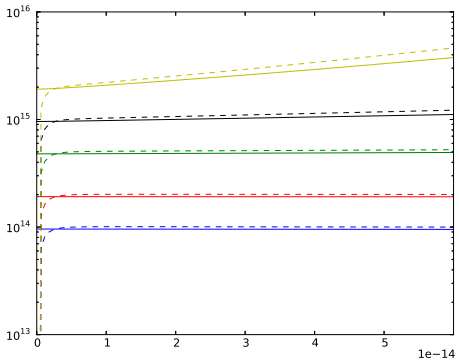

(e) $N_v = 128$, Quick Operator

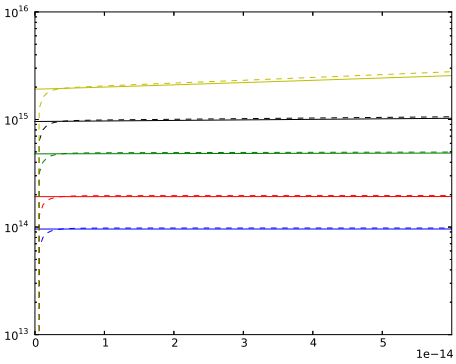

(f) $N_v = 128$, Full Operator

Figure 3.7: Plots of Current produced vs time using the quick(left) and full(right) BGK collision operators(Dashed) and the corresponding values calculated using transport coefficients(Solid) for external fields of: $2 \times 10^9 V/m$(Yellow), $10^9 V/m$(Black), $5 \times 10^8 V/m$(Green), $2 \times 10^8 V/m$(Red) and $10^8 V/m$(Blue) for a Z=6, Carbon plasma. The x-axis is time in seconds and the y-axis is current produced in amperes per square metre.

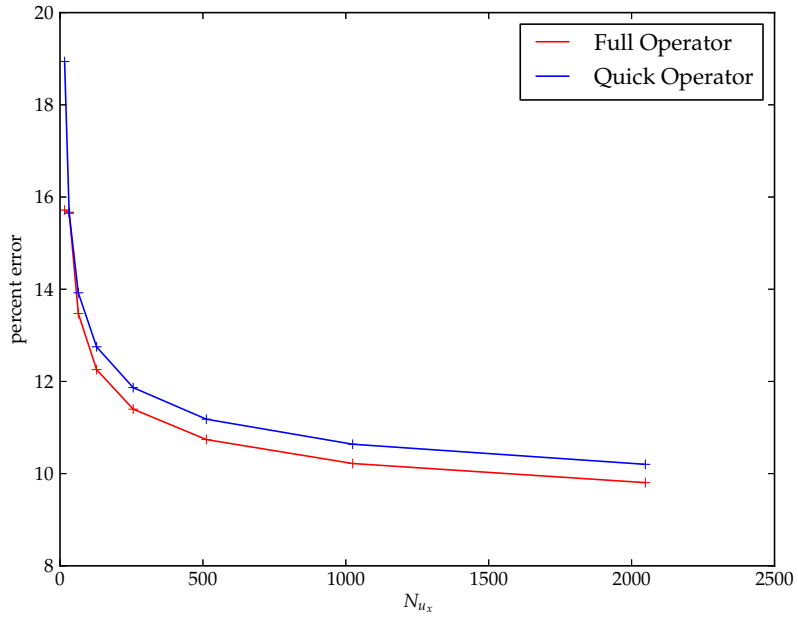

Figure 3.8: Percentage error from Spitzer using the Quick and Full Krook operators with increasing velocity space resolution.

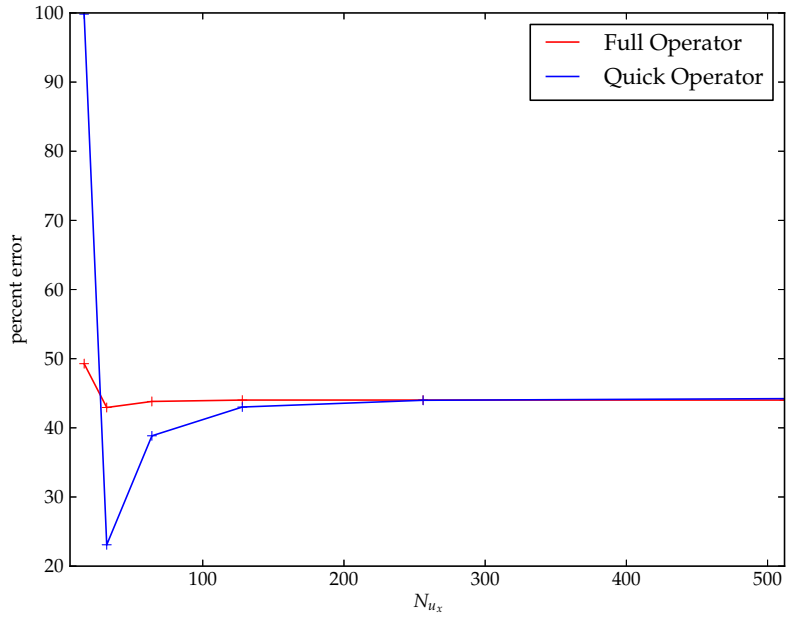

Figure 3.9: Percentage error in Krook calculated heat flux vs number of velocity grid points.

	κ error percent	η error percent	Total
No ζ	54.42006	13.40263	67.82270
ζ on e-e	42.43956	8.91618	51.35574
ζ on e-i	28.52109	101.62206	130.14315
ζ on e-e and e-i	0.43213	116.57071	117.00285

Figure 3.10: Quick Operator: Error in transport calculations for ζ applied to each operator

	κ error percent	η error percent	Total
No ζ	52.165 33	12.496 36	64.661 69
ζ on e-e	40.488 50	7.518 29	52.984 86
ζ on e-i	21.690 23	77.282 02	98.972 25
ζ on e-e and e-i	8.183 17	97.852 51	106.035 68

Figure 3.11: Full Operator: Error in transport calculations for ζ applied to each operator

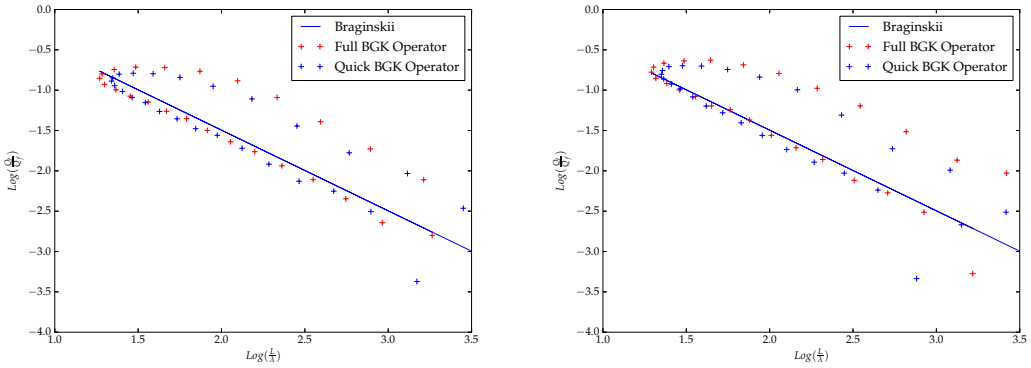

(a) Hydrogen Plasma, Z=1

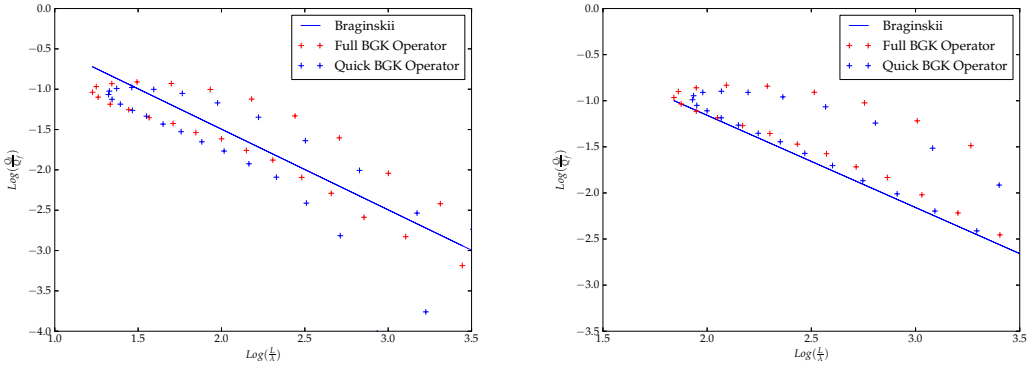

(b) Beryllium Plasma, Z=4

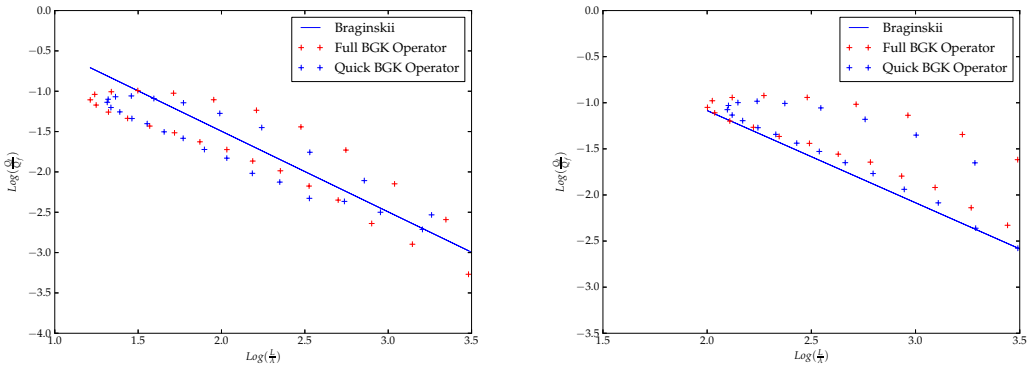

(c) Carbon Plasma, Z=6

Figure 3.12: Plots of heat flow vs inverse temperature gradient without(left) and with(right) Heat flux normalisation.

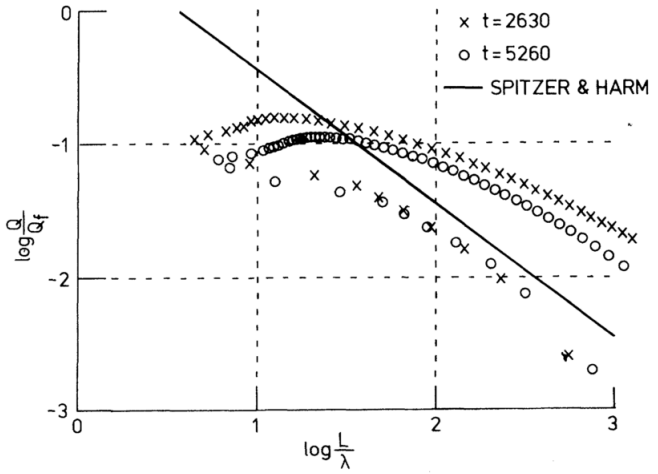

Figure 3.13: Non-Local transport. Reproduced from Bell, Evans and Nicolas [62]

3.7 Discussion

In this section the implementation of a collision operator for electron-electron, electron-ion and ion-ion collisions has been discussed and its accuracy has been benchmarked against the classical transport coefficients. It's seen that in the regimes where classical transport is valid, the operator is able to to accurately reproduce the theoretical electrical conductivity. The operator does however overestimate the thermal conductivity, but this was seen to be corrected by normalising the operator to ensure accuracy in the local limit. With the factor ζ applied to both electron-electron and electron-ion collisions it was seen for both operators that the difference between the Braginskii value and the thermal conductivity calculated using VALIS was less than 10%. This however produced an error in the electrical conductivity of over 100% of the Spitzer value By compromising and limiting the normalisation to electron-electron collisions it was shown that it's possible to improve the accuracy of the heat flux while at the same time increasing the accuracy in the electrical conductivity. In the steeper temperature gradients seen in inertial confinement experiments the mean free path of the electrons from the hot side of the gradient can exceed the temperature scale length. In this case the energy transported by suprathermal electrons is not accounted for by the classical transport coefficients. However, both the full and quick Krook implementations yielded similar results to those obtained by Bell et. al. using the Fokker-Planck operator. The ability of the Krook operator to reproduce the non-local transport predicted by Fokker-Planck simulations is an important result for its applicability to laser-plasma modelling. It also should be noted that the Fokker-Planck model itself is a truncated expansion of the Boltzmann collision operator in the reciprocal of the Coulomb logarithm. In the cold dense core of an inertial confinement target the Coulomb logarithm can be around the order of unity, implying the error in this model due to the truncated terms could of the order of 100%.

Chapter 4

Using the Krook Operator to Model Laser Heating

4.1 Introduction

The implicit implementation of the Krook collision operator outlined in the previous chapter can be modified to give a method of heating the plasma at a rate consistent with the energy deposition from a high energy laser pulse. While the laser-plasma interaction region can be accurately simulated with an Eulerian Vlasov solver, it is convenient to have a method of simply heating the plasma. Modelling an external heat source is a feature that allows direct comparison of results with Fokker-Planck simulations which also use an phenomenological heat source [1, 40].

4.2 Implementation

A heating term in the spirit of the Krook model then takes the form:

$$\left(\frac{\partial f}{\partial t}\right)_{HEAT} = -\nu_H(f - f_H)$$

Where $\nu_H = \nu_H(x,t)$ is a heating rate depending on position and temperature and f_H is a Maxwellian velocity distribution:

$$f_H = \frac{a_1}{2\pi a_3} exp\left(-\frac{(v_x - a_2)^2 + (v_y - a_4)^2}{2a_3}\right)$$

Where the parameters a_1, a_2 and a_4 are the density and x, y components of the centre of mass velocity respectively. The parameter $a_3 = T_{hot}$, the target temperature which is defined as an input.

The power delivered using this operator is given by:

$$P = \nu_H \int \frac{1}{2} m v^2 (f_H - f) dv$$

or $P = \nu_H h$, where the difference in energy,

$$h = \int \frac{1}{2} m v^2 (f_H - f) dv$$

The power delivered can be varied in time and space as

$$P = P_0 \cos^2 \left(\frac{\pi x}{x_h} \right) \sin \left(\frac{\pi t}{\tau_h} \right)$$

Where x_h is the depth over which the heating function is active into the plasma and τ_h is the duration of the heating. P_0 is set to match the energy delivered by a laser pulse with a intensity profile varying in time as:

$$I = I_0 \sin \left(\frac{\pi t}{\tau_p} \right)$$

Thus,

$$P_0 = \frac{2 I_0}{x_h}$$

The algorithm for the heating term is then:

1. Integrate f to get density and (U_x, U_y) drift.
2. Evaluate $h(x,t) = \int \frac{1}{2} m v^2 (f_h(a_n) - f) dv$
3. Evaluate $P(x,t) = P_0 \cos^2(\frac{\pi x}{x_h}) \sin(\frac{\pi t}{\tau_h})$
4. Calculate heating rate

$$\nu_H(x,t) = \begin{cases} 0, & \text{if temperature } \geq T_{hot} \\ \frac{p(x,t)}{h(x,t)}, & \text{otherwise} \end{cases}$$

5. Update f using the implicit Krook method, $f^{n+1} = f^n + \nu_H (f^{n+1} - f_H)$

Figure 4.1 plots the temperature at x=0 as a function of time. The heating function is applied to the distribution function as described above varying in intensity over time $\sim \sin \pi t \tau_h$ until the specified target temperature is reached and heating is switched off. Figure 4.2 plots the electron velocity distribution evolution during the heating phase. Note that during the heating at $f = 50$fs the distribution function is non-Maxwellian with over emphasised high velocity tails. Whilst this is an artefact of the heating functions equal application over velocity space, it is an effect is at least in qualitative agreement with previous PIC simulations [63] of laser heating. Figure 4.3 plots the distribution function over the domain to illustrate the spatially dependent heating. The heating is varied in space as $\sim \cos^2(\frac{\pi x}{x_h}$, with x_h being 250 Debye lengths of the 100eV plasma. For all these tests, particle advections and collisions were turned off.

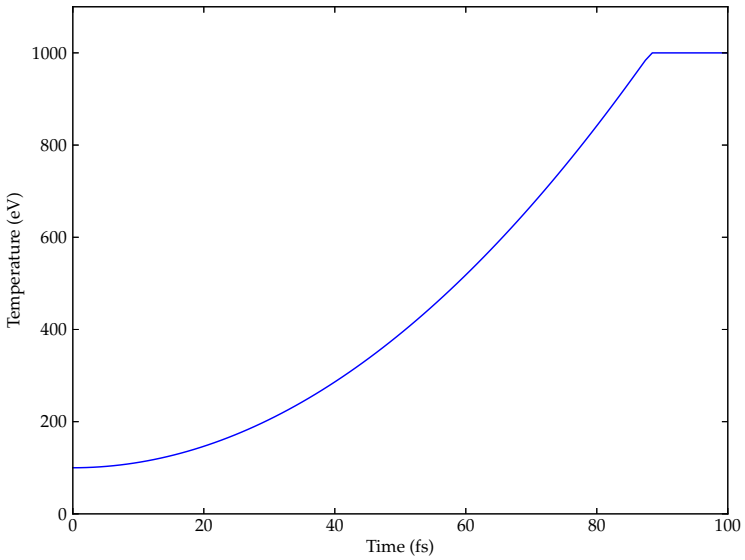

Figure 4.1: Heating a 100eV plasma to 1000eV over 100 femtoseconds

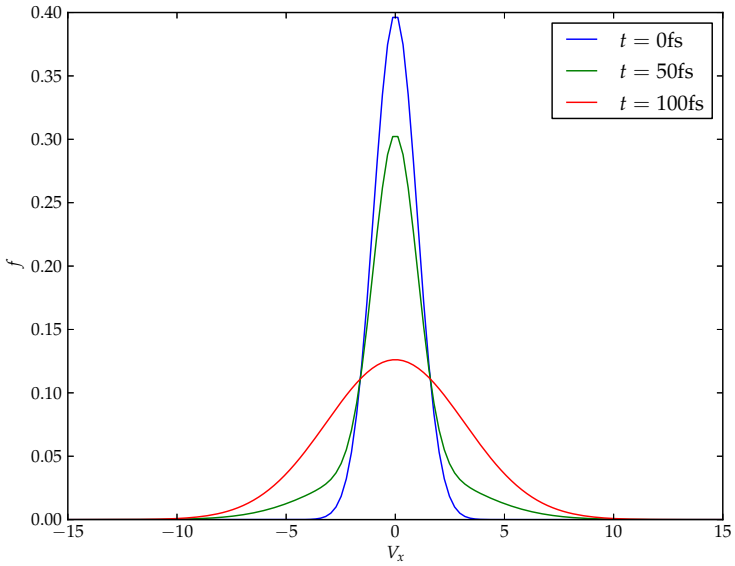

Figure 4.2: Plot of heated electron velocity distribution over time

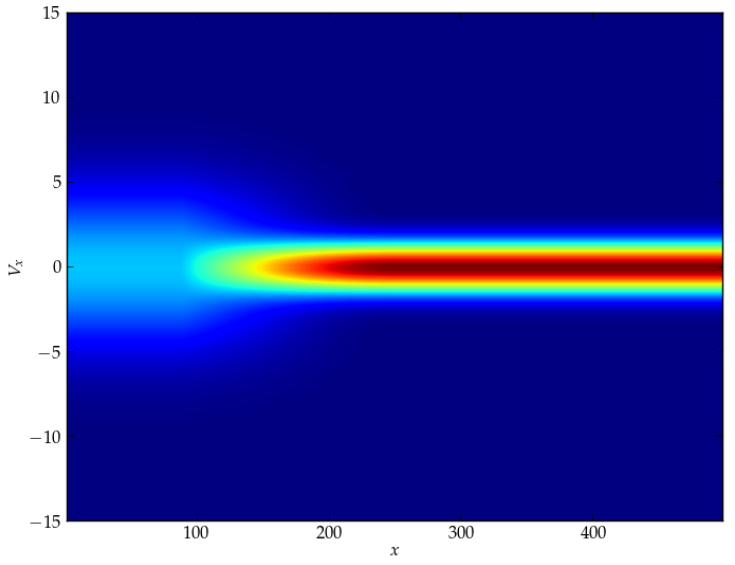

Figure 4.3: Electron distribution function at $t = 100fs$

4.3 Using Separate Distributions

A drawback of directly solving Vlasov's equation is the requirement to resolve a maximum velocity. For problems involving laser heating the temperature of

the hot distribution is far larger than that of the initial population. Thus the method outlined above requires the minimum and maximum velocities of the electron distribution function to be large to account for the high velocity tails of the hot distribution, decreasing the resolution of the initial distribution and therefore decreasing the accuracy of the solution in the cold regions.

This problem can mitigated by treating the hot electrons as a separate distribution function. This is done by subtracting a fraction of the cold distribution and adding that to a hot distribution function at each timestep. The heating rate used is the same as the one defined above. The hot distribution function is advanced from time n to $n+1$ through:

$$f_h^{n+1} = f_h^n + \Delta t \nu_H f_m$$

To update the cold distribution f_c, one cannot simply subtract the same term

$$f_c^{n+1} = f_c^n - \nu_H f_m,$$

Since this will lead to negative f in the tails of the distribution. Instead the density of the cold distribution must satisfy

$$\int f_c^{n+1} dv = \int f_c^n dv - \Delta t \nu \int f_m dv$$

We therefore want to find a factor α such that

$$\int f_c^{n+1} dv = \alpha \int f_c^n dv$$

thus,

$$\alpha = \frac{\int f_c^n dv - \Delta t \nu_H \int f_m dv}{\int f_c^n dv}$$

The two distribution functions however must both contribute to the solution of Maxwell's equations so from chapter 2, equations 2.30 and 2.31 for the

integrated current densities become:

$$\tilde{J}_x^k(i,j) = -\sum_{m=1}^{n_{u_x}}\sum_{n=1}^{n_{u_y}} h_x(m,n) f_{ec}^k(i,j,m,n)\Delta u_x(m)\Delta u_y(n) - \sum_{m=1}^{n_{u_x}}\sum_{n=1}^{n_{u_y}} h_x(m,n) f_{eh}^k(i,j,m,n)\Delta u_x(m)\Delta u_y(n)$$

$$\tilde{J}_y^k(i,j) = -\sum_{m=1}^{n_{u_x}}\sum_{n=1}^{n_{u_y}} h_y(m,n) f_{ec}^k(i,j,m,n)\Delta u_x(m)\Delta u_y(n) - \sum_{m=1}^{n_{u_x}}\sum_{n=1}^{n_{u_y}} h_y(m,n) f_{eh}^k(i,j,m,n)\Delta u_x(m)\Delta u_y(n)$$

Both distributions must also be considered in collision terms. For the hot and cold electron distributions the collision terms become:

$$\left(\frac{\partial f_e h}{\partial t}\right)_c = -\nu_{eh-eh}(f_e h - F_{e1}) - \nu_{eh-ec}(f_e h - F_{e2}) - \nu_{ei}(f_e - F_{e3}) \quad (4.1)$$

$$\left(\frac{\partial f_e c}{\partial t}\right)_c = -\nu_{ec-ec}(f_e h - F_{e1}) - \nu_{ec-eh}(f_e h - F_{e2}) - \nu_{ei}(f_e - F_{e3}) \quad (4.2)$$

The two distribution functions after a period of heating are shown in figures 4.4 and 4.5

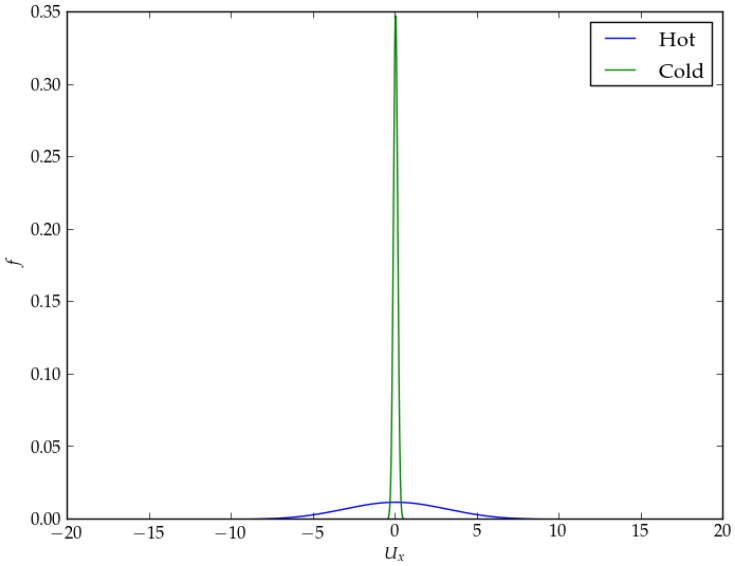

Figure 4.4: Hot and Cold Distribution functions

The target temperature T_{hot} is chosen to inline with the energy gained by the electrons from a laser of a given intensity and wavelength. A simple method for calculating this temperature is by assuming ponderomotive scaling [63]

$$T_{hot} \simeq \left[\frac{I_L}{1.2 \times 10^{19} W/cm^2 (\frac{\lambda_L}{1.06 \mu m})^2} \right]^{\frac{1}{2}} MeV$$

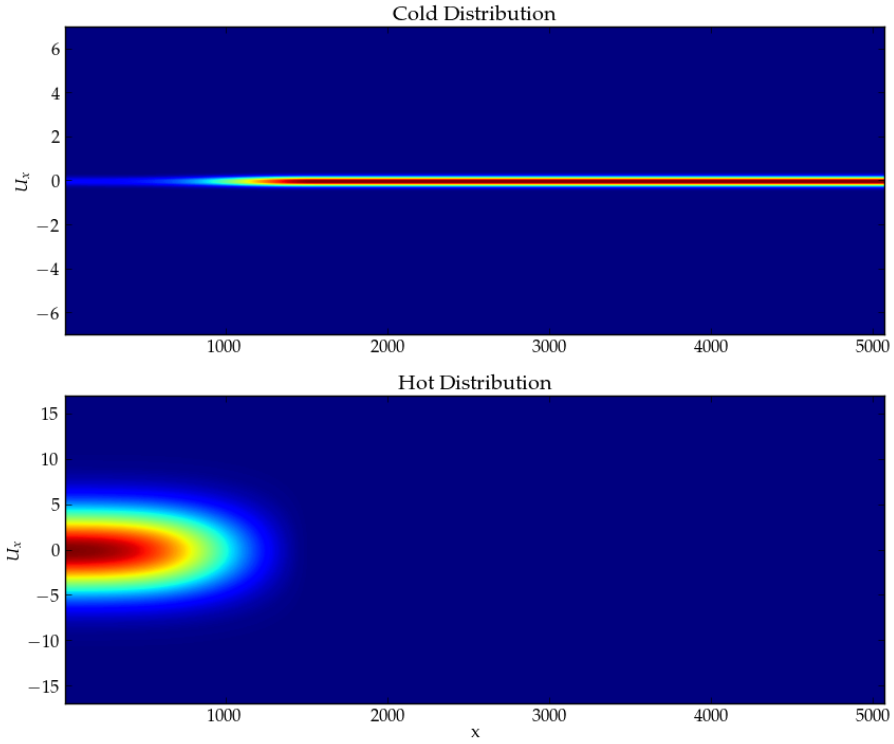

Figure 4.5: Hot and Cold Distribution functions for heterogenous heating

4.4 Summary

A method for augmenting the Krook collision operator to implement a simple mechanism for modelling laser heating has been outlined. The target temperature can be chosen inline with ponderomotive scaling but there is no reason why this method could not be used to implement heating due to another phenomenological effect. A method for subtracting a fraction of the electrons and placing them in a separate hot distribution was also outlined for situations where that may be advantageous. The most obvious advantage is where the maximum velocity grid requirements due to the hot electrons would necessitate a large number of velocity grid points to maintain resolution of the cold distribution. In the next chapter this heating source will be used to model the energy deposition of a short pulse laser in regimes relevant to fast ignition. While modelling a laser in an Eulerian Vlasov solver is simple, it is advantageous to possess a method of predictably heating the plasma whilst

maintaining total f.

Chapter 5

Model Fokker-Planck Operators

5.1 Introduction

Rathmann and Denavit [64] proposed a reduced Fokker-Planck collision operator of the form:

$$\left(\frac{\partial f}{\partial t}\right)_c = \frac{\partial}{\partial v}\left[\nu v f + D\frac{\partial}{\partial v}(\nu f)\right] \tag{5.1}$$

Where ν is the relevant collision frequency and the coefficient D is a parameter chosen such that the operator conserves energy and for a velocity dependent collision frequency is given by:

$$D = \frac{\int \nu(v) v^2 f dv}{\int \nu(v) f dv}$$

The collision operator in equation 5.1 is a non-linear advection-diffusion equation and can be interpreted and dealt with as two separate parts. The friction term,

$$\left(\frac{\partial f}{\partial t}\right)_{friction} = \frac{\partial}{\partial v}\nu(v) v f(v,t)$$

is simply an advection in velocity space pulling particles to the mean of a stationary velocity distribution. This term can be readily generalised to a

drifting distribution by introducing a drift velocity, so the velocity dependent advection equation can be written as:

$$\frac{\partial f}{\partial t} = \frac{\partial f}{\partial v}\nu(v)(v - u_{drift})$$

This advection now acts to drag particles towards the drift velocity. Care however must be taken in handling this term numerically. Since the drift velocity is calculated by integrating the distribution function, any numerical error causes this term to drag particles toward a spurious mean. This creates feedback in the next time step and can cause acceleration in the direction of the initial bias.

In their paper, Rathmann and Denavit apply this operator to a particle in cell method and simply add a velocity dependent acceleration to each particle. For a solver based entirely on a grid this must be carried out as an advection in velocity space. A conservative, positivity preserving scheme is required to carry out this advection numerically. The Piecewise Parabolic Method(PPM) detailed in Chapter 2 possesses these properties and is used.

The diffusion term can be written as:

$$\left(\frac{\partial f}{\partial t}\right)_{diffusion} = D\frac{\partial^2}{\partial v^2}(\nu(v)f)$$

The numerical scheme presented in the original paper suggests implementing the diffusion operator explicitly through:

$$f^{n+1} = f^n + \frac{2D\Delta t}{\Delta v_{i-1} + \Delta v_i}\left(\frac{(\nu f)_{i+1} - (\nu f)_i}{\Delta v_i} - \frac{(\nu f)_i - (\nu f)_{i-1}}{\Delta v_{i-1}}\right)$$

and iterating this update so the CFL condition is satisfied. For a general purpose collision operator however this can lead to prohibitively large numbers of iterations. While it precludes simple parallelisation along the velocity axis, an implicit scheme is chosen to remove the timestep restriction on the diffusion operator. Popular numerical schemes for time integrating the diffusion equation are the Crank-Nicolson and Backward Euler methods. The Crank-Nicolson method however does not damp high frequency components and if the diffusion number is high, can introduce spurious oscillations into the solution. For the diffusion equation here, the diffusion number, proportional to $\frac{\nu}{dv^2}$ is high around the origin due to the high collisionality of slow particles and the

fine resolution when a nonuniform velocity grid is used. Instead, the backward Euler method is used, which damps high frequency oscillations.

The distribution function is advanced using the backward Euler method, which when rearranged becomes:

$$-\alpha_i f_{i-1}^{n+1} + (1+2\alpha) f_i^{n+1} - \alpha_i f_{i-1}^{n+1} = f_i^n$$

Where $\alpha_i = \frac{D\nu(v_i)\Delta t}{dv^2}$. With the boundaries clamped at zero in velocity space this is a purely tridiagonal system which is solved using the Thomas [35] algorithm.

5.2 Electron-Ion Collisions

For electron-electron collisions the operator is implemented as above. The velocity dependent electron-electron collision frequency derived earlier in the chapter is used. Using the diffusion coefficient in equation 5.1 the electron-electron collision operator conserves and energy.

For electron-ion collisions there is a transfer of energy from one species to the other. A hot electron distribution should eventually cool to the temperature of the ions. Using a similar method described by Dougherty [65, 66], a mechanism for electrons to gain or lose energy to the ions in the cross collision terms is implemented by modifying equation 5.1 so that the friction and diffusion operators become:

$$\left(\frac{\partial f}{\partial t}\right)_{friction} = \frac{\partial}{\partial v}\nu_{ei}(v)(v - U_{ei})f(v,t)$$

$$\left(\frac{\partial f}{\partial t}\right)_{diffusion} = \frac{kT_{ei}}{m}\frac{\partial^2}{\partial v^2}(\nu_{ei}(v)f)$$

Where the combined moments are given by:

$$U_{ei} = \alpha_e U_e + \alpha_i U_i$$
$$T_{ei} = \beta_e T_e + \beta_i T_i$$

Here, $\alpha_e = 0$ and $\alpha_i = 1$, meaning that the friction term only drags

particles towards the centre of mass velocity of the ions. The coefficients:

$$\beta_e = \frac{m_i}{m_e + m_i}$$
$$\beta_i = \frac{m_e}{m_e + m_i}$$

mean that now the ion temperature influences the rate of diffusion in velocity space and thus a change in temperature.

5.3 Numerical Tests

5.3.1 Approach to Equilibrium

A situation where one would expect a Krook operator to perform poorly is the case where there are two distinct beams propagating in opposite directions in velocity space. In this case the Krook operator tries to fit a Maxwellian whose drift is the average of the two beams.

To test collisional relaxation to an equilibrium distribution, the plasma is initialised with two opposing cold populations using the distribution function,

$$f(v, t=0) = \frac{n}{2(2\pi)^{\frac{1}{2}} T_0} \left\{ exp\left[-\frac{1}{2} \left(\frac{v - v_{d0}}{T_0} \right)^2 \right] + exp\left[-\frac{1}{2} \left(\frac{v + v_{d0}}{T_0} \right)^2 \right] \right\}$$

Where T_0 and v_{d0} are the temperature and drift speeds of each population. For a velocity independent collision frequency the time evolution of this may be solved analytically by taking a Fourier transform with respect to velocity.

The solution is then

$$f(v, t) = \frac{n}{(2\pi v_b)^{\frac{1}{2}}} \left\{ exp\left[-\frac{1}{2} \left(\frac{v - v_d}{v_b} \right)^2 \right] + exp\left[-\frac{1}{2} \left(\frac{v + v_d}{v_b} \right)^2 \right] \right\}$$

Where $v_b = D - (D - v_{b0}^2) exp(-2\nu t)$ and $v_d = v_{d0} exp(-\nu t)$. It's easy to see that as $t \to \infty$, the equilibrium distribution is Maxwellian,

$$f(v, t \to \infty) = \frac{n}{\sqrt{2\pi D}} exp\left(\frac{v^2}{2D} \right)$$

and when $t = 0$, equation 5.3.1 is obtained.

However, for the velocity dependent form of the operator, the collision frequency is a function of time. At equilibrium, with $f(v \to \infty) = 0$,

$$\nu v f + D\frac{\partial}{\partial v}(\nu f) = 0$$

which can be integrated to give

$$f(v) = \frac{f(0)\nu(0)}{\nu(v)} e^{-v^2/2D} \tag{5.2}$$

Where $f(0)$ and the coefficient D are determined by the density and mean square velocity

$$\int_{-\infty}^{\infty} f dv = 1 \tag{5.3}$$

$$\int_{-\infty}^{\infty} v^2 f dv = \langle v^2 \rangle \tag{5.4}$$

The mean square velocity $\langle v^2 \rangle$ is known and should be conserved throughout the approach to equilibrium. Assuming a collision frequency of the form,

$$\nu(v) = C/(2\langle v^2 \rangle + v^2)^{3/2}$$

where $C = (3\langle v^2 \rangle)^{3/2}\nu_0$ where ν_0 can be interpreted as the collision frequency of a particle at the thermal velocity, $v = k_B T/m$. Substituting this collision frequency into equations 5.3 and 5.4 gives

$$2^{1/2}\langle v^2 \rangle^{1/2} f(0) \int_{-\infty}^{\infty} (1+x^2)^{3/2} e^{-\alpha x^2} dx = 1 \tag{5.5}$$

$$2^{3/2}\langle v^2 \rangle^{1/2} f(0) \int_{-\infty}^{\infty} x^2 (1+x^2)^{3/2} e^{-\alpha x^2} dx = 1 \tag{5.6}$$

where $\alpha = \langle v^2 \rangle / D$. The integrals in these two equations may be expressed in terms of the first and second order modified bessel functions of the second kind, giving:

$$f(0) = \frac{2^{1/2}}{\langle v^2 \rangle^{1/2}} e^{-\alpha/2} \left[K_0\left(\frac{\alpha}{2}\right) + \left(1 + \frac{1}{\alpha}\right) K_1\left(\frac{\alpha}{2}\right) \right]^{-1} \tag{5.7}$$

and

$$f(0) = \frac{2^{1/2}}{(2\langle v^2\rangle)^{1/2}} e^{-\alpha/2} \left[\frac{1}{2} K_0\left(\frac{\alpha}{2}\right) + \left(\frac{1}{2} + \frac{2}{\alpha}\right) K_1\left(\frac{\alpha}{2}\right)\right]^{-1} \tag{5.8}$$

solving these gives,

$$\alpha = \frac{\langle v^2\rangle}{D} = 1.76 \tag{5.9}$$

and

$$f(0) = \frac{0.3537}{\langle v^2\rangle^{1/2}} \tag{5.10}$$

Substituting 5.9 and 5.10 into equation 5.2 gives the velocity distribution at equilibrium, as derived in [64]:

$$f(v, t \to \infty) = \frac{0.3537n}{\langle v^2\rangle^{1/2}} \left(1 + \frac{v^2}{2\langle v^2\rangle}\right)^{3/2} e^{-0.88v^2/\langle v^2\rangle} \tag{5.11}$$

Which notably is not the Maxwell-Boltzmann distribution.

In this test electron-ion collisions are turned off. The results for the velocity independent and velocity dependent model Fokker-Planck electron-electron collision operators are plotted in figures 5.2 and 5.3 respectively. Under these conditions the results are almost identical. The numerical results show excellent agreement with the analytical solution. Over the timescales here the magnitude of the change in total energy never exceeded $\sim 0.01\%$. For the tests below, $v_{b0} = 0.0001$ and $v_{d0} = 0.8$ Tests with larger initial drifts and temperatures yielded identical results.

As the initial distribution function is extremely non-Maxwellian, one would expect the Krook operator to perform poorly under these conditions. The results for the Krook operator are plotted in figure 5.4. Since this operator simply applies the equilibrium distribution at each time-step, we do not see the decay in the drifts of the beams, instead the beams remain stationary and their mass is distributed across velocity space. It's also worth noting that the Krook operator, while conserving total energy, has gained 10% mass over the course of the simulation. This change in mass is due to the convergence criteria on the fully conservative Krook operator and can be alleviated by simply reducing the error tolerance at the expense of increasing the number of iterations required. This accounts for the difference between the equilibrium distribution calculated at the start compared to the one obtained numerically.

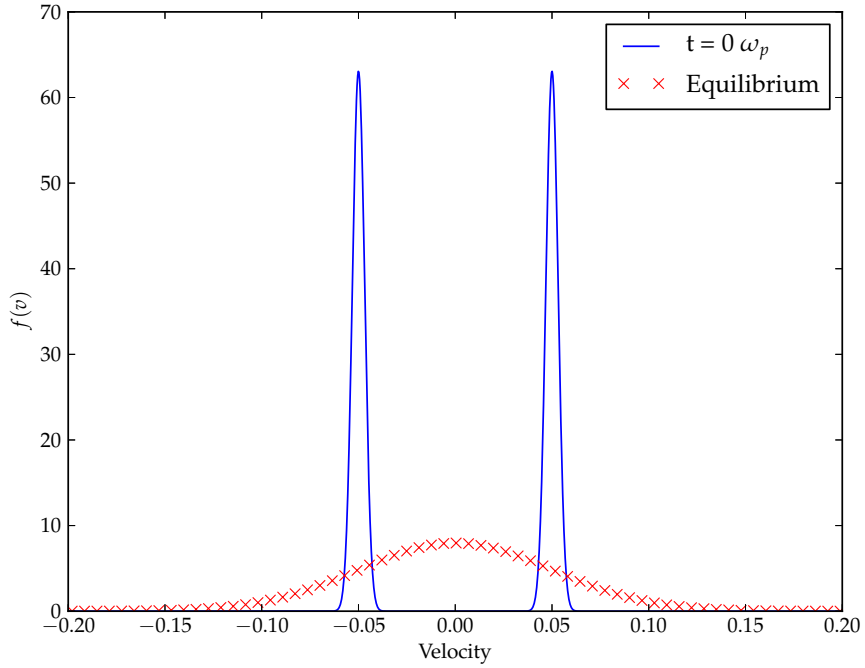

Figure 5.1: Initial velocity distribution for the relaxation tests

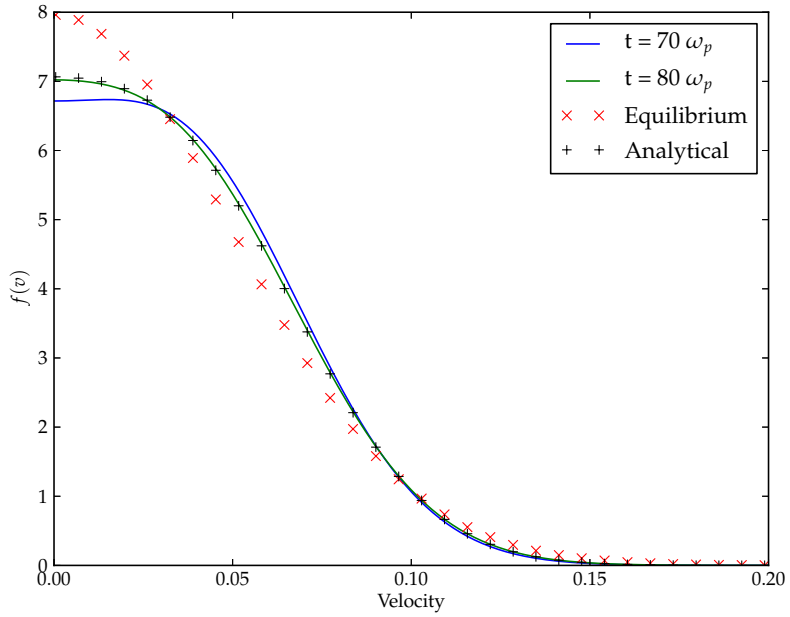

(a)

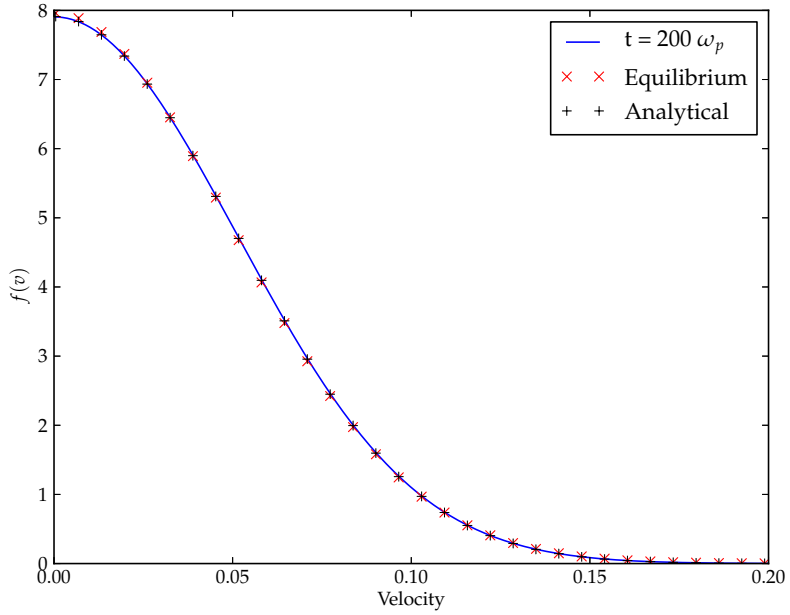

(b)

Figure 5.2: Approach to Equilibrium, Model Fokker-Planck Operator with a Velocity Independent Collision Frequency. Here $V_{b0} = 0.00001$ and $V_{d0} = 0.05$.

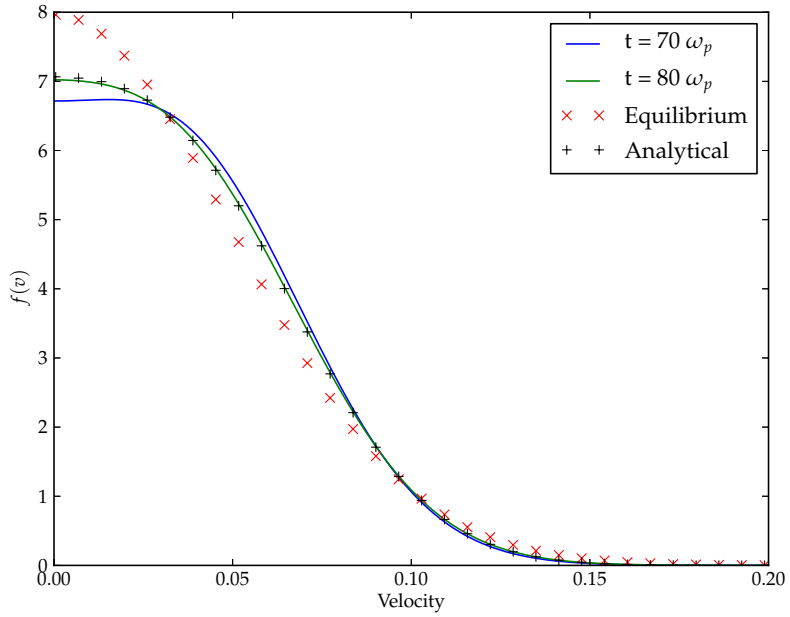

(a)

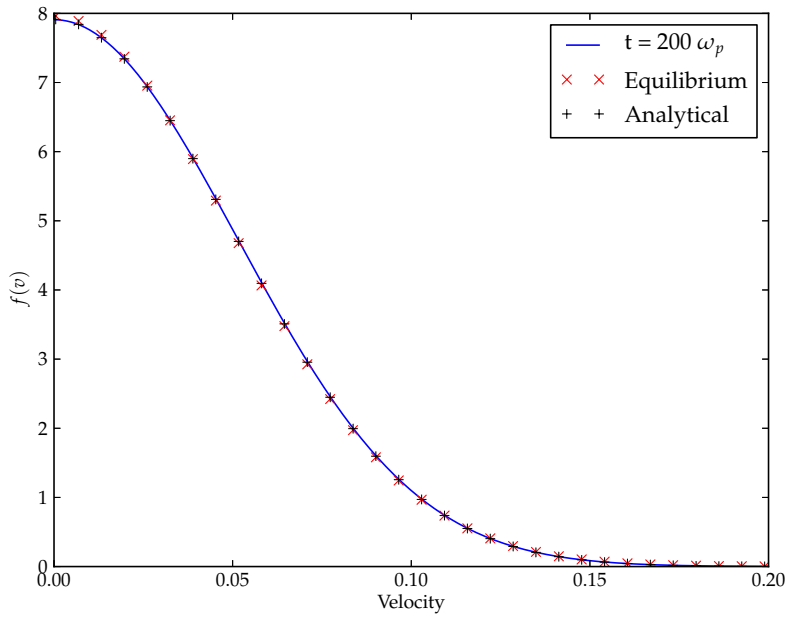

(b)

Figure 5.3: Approach to Equilibrium, Model Fokker-Planck Operator with a Velocity Dependent Collision Frequency. Here $V_{b0} = 0.00001$ and $V_{d0} = 0.05$.

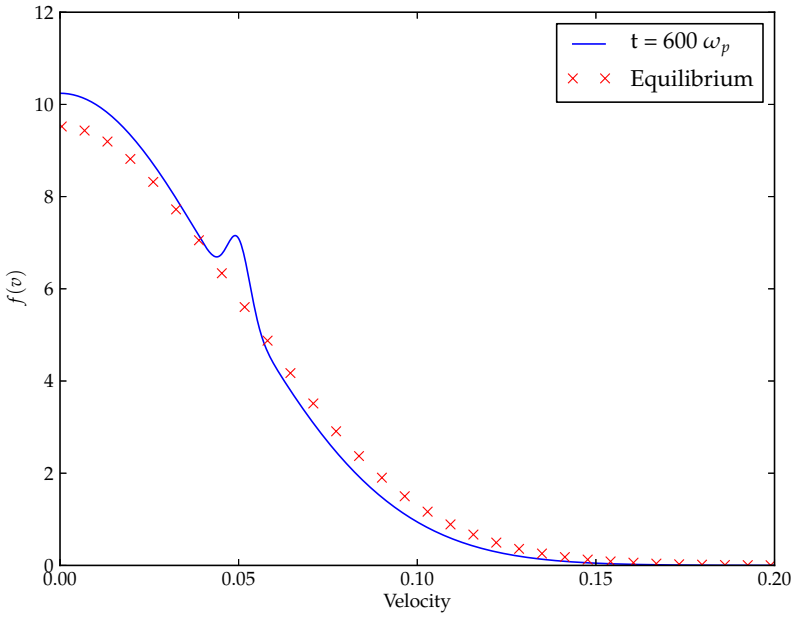

(a)

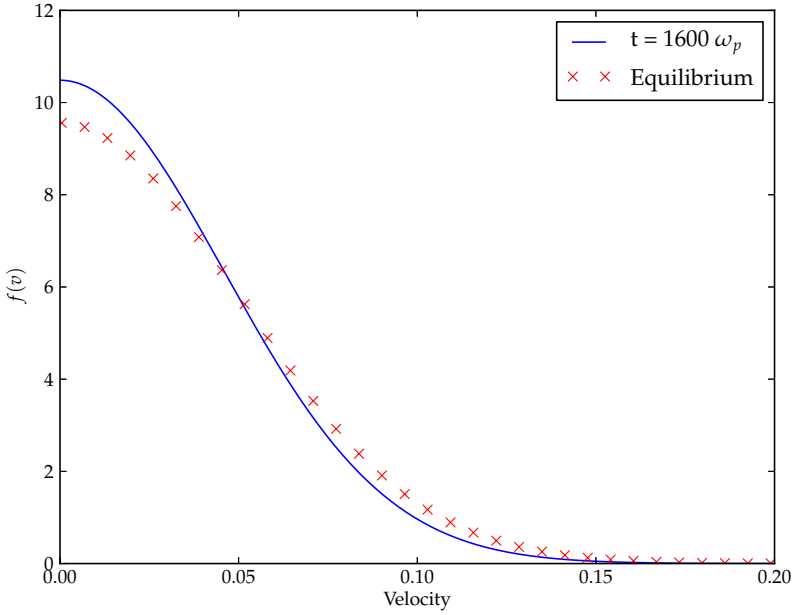

(b)

Figure 5.4: Approach to Equilibrium, Krook Collision Operator. Here $V_{b0} = 0.00001$ and $V_{d0} = 0.05$.

5.3.2 Collisional Heating and Electrical Conductivity

To test both the electron-electron and electron-ion collision operator, the plasma is heated by a strong homogenous DC electric field. Figure 5.5 compares the velocity distribution produced after $400\omega_p$ for the Krook operator and the model Fokker-Planck operator with and without a velocity dependent collision frequency. The Krook operator, as shown in chapter 3 reproduces classical transport well under these conditions so is useful as a comparison. The model Fokker-Planck operator with a velocity dependent collision frequency shows a similar shape to the Krook model, the velocity distribution deviates from a Maxwellian as particles of differing velocities are allowed to thermalise at different rates. The Model Fokker-Planck operator with a constant collision performs poorly in this test as it is unable to thermalise the momentum gained from the electric field.

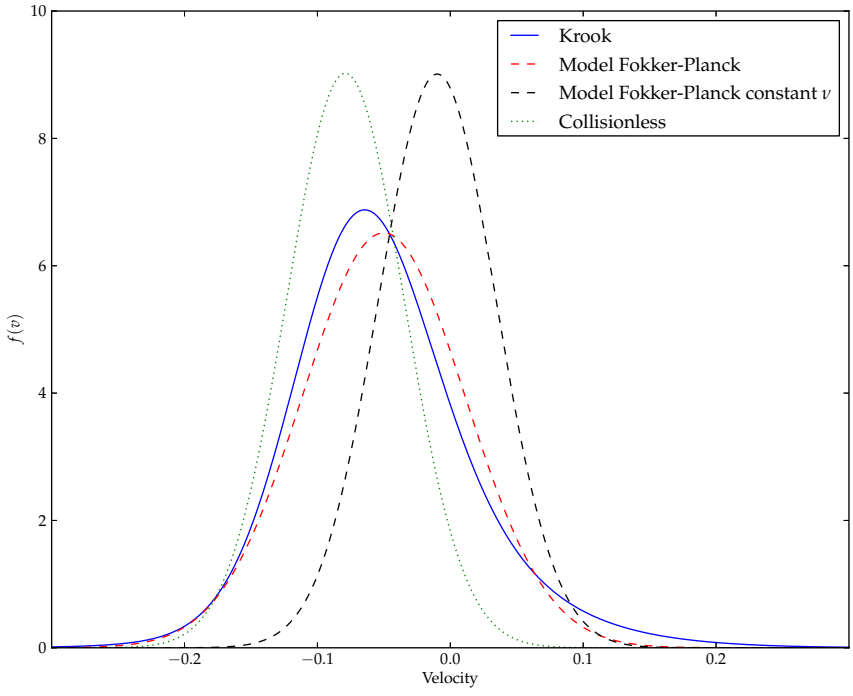

Figure 5.5: Collisional heating by a DC electric field $= 1 \times 10^{10}$V/m. The velocity distribution is plotted at $400\omega_p$

The current produced by a DC electric field is compared to that predicted by Spitzer as in chapter 3 and is plotted in figure 5.6. In this test, the number of velocity points, N_v was 6,000 to obtain results for the lower field strengths. Lower resolution tests were unable to capture the small changes in drift velocities generated by the weaker electric fields and were negated completely by the friction term. The model Fokker-Planck collision operator with a velocity independent collision frequency was unable to reproduce transport anywhere near those predicted by Spitzer.

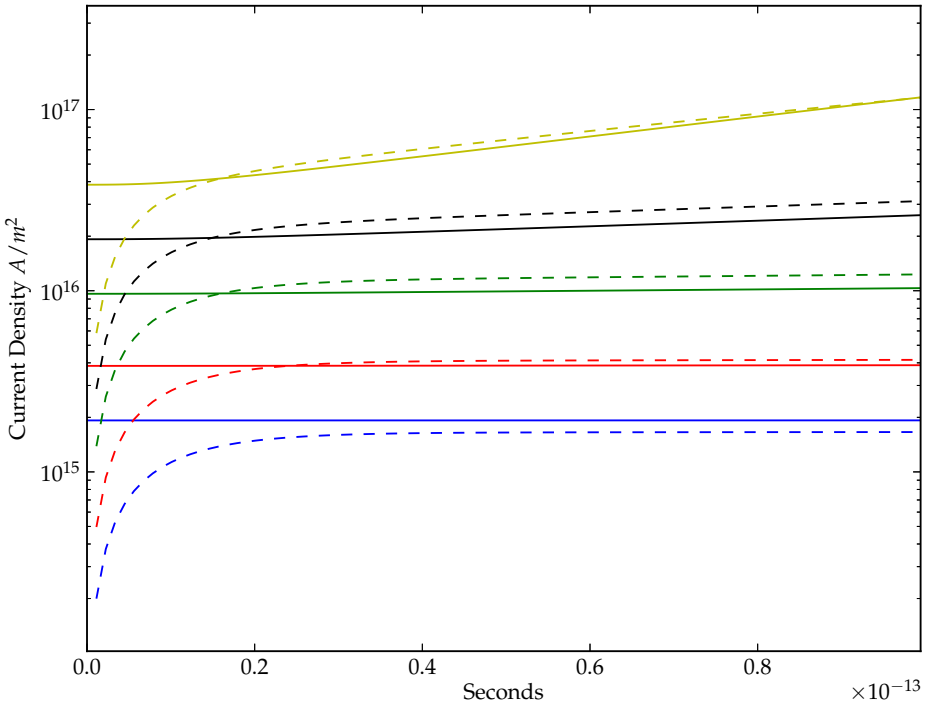

Figure 5.6: Current Produced by a DC electric field calculated by the model Fokker-Planck operator with a velocity dependent collision frequency(Dashed) and that predicted by the classical transport coefficients(Solid). The colours correspond to external fields of: $2 \times 10^9 V/m$(Yellow), $10^9 V/m$(Black), $5 \times 10^8 V/m$(Green), $2 \times 10^8 V/m$(Red) and $10^8 V/m$(Blue)

5.4 Summary

The two forms of the Model Fokker-Planck collision operator have been applied to some transport and collisional relaxation tests. In the approach to relaxation test both the velocity dependent and independent forms of the operator yielded almost identical results. This test also highlighted the limitations of the Krook model in this particular scenario where the distribution function is far away from equilibrium. The collisional heating test highlighted the benefit of the velocity dependent operator over the the velocity independent model and indeed this was evident its ability to reproduce the classical electrical conductivity from Spitzer. A disadvantage in this model however is the explicit numerical implementation of the friction term. This explicit term limits the time-step to $\Delta U_x/U_x\nu$, which in the case of velocity dependent collisions can become huge around the origin, requiring an artificial limit on $\nu(v)$. These problems however could be resolved through adapting the implementation to a stable fully implicit method [67, 68]. However it was proven that the equilibrium distribution function for the velocity dependent collision frequency was not the Maxwell-Boltzmann distribution. While this issue did not impact the results in the idealised tests done here, it raises questions over its wider applicability. Both forms of the Model Fokker-Planck operator were also unable to reproduce either classical thermal transport or the non-local transport given by calculations using the full Fokker-Planck collision integral or the Krook model. As a result, while in certain scenarios the model Fokker-Planck operator gives a better representation of the physics, particularly in the case of a strongly non-Maxwellian plasma, it is the Krook operator that has to be preferred for its robustness and accuracy in more general scenarios.

Chapter 6

Fast Electron Transport and Return Currents

6.1 Introduction

In fast ignition studies the interaction of an ultra-intense laser($> 10^{22} W m^{-2}$) with an overdense plasma leads to the acceleration of electrons away from the laser pulse via a number of different mechanisms, most notably through inverse bremstrahlung, vacuum heating [69] [70], resonance between the laser pulse and plasma waves, $\mathbf{J} \times \mathbf{B}$ acceleration and the ponderomotive force [43]. This accelerated beam of electrons then propagates though the coronal plasma and constitutes a significant forward current, $\boldsymbol{J}_F$ Through the low density coronal plasma the electrons in this beam have a mean free path many times longer than the length of the target so are essentially collisionless. This forward current sets up an electric field which draws a collisional return current $\boldsymbol{J}_R$ which is roughly equal to the forward current. The non-equilibrium distribution functions produced in this scenario means the classical transport theory is not valid.

6.2 Simulation

The electron density profile(figure 6.1) is chosen to match previous simulations [1] using the full Fokker-Planck collision term and represents a cone-guided fast ignition scenario. The ions form a neutral background and are

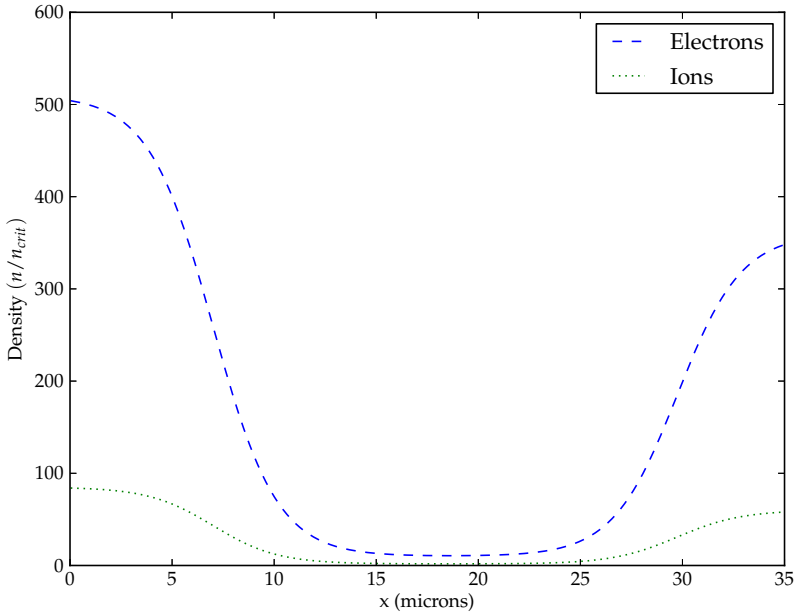

Figure 6.1: Initial density profiles

assumed immobile. Fast electrons are generated in the solid density region in the first $10\mu m$ which represents the gold cone. They then travel through the low density beryllium fuel shell coronal plasma that rises from $10n_{crit}$ to $350n_{crit}$ at the right hand boundary. To generate a hot 1D Maxwellian profile, the heating function described in the chapter 4 is used to model a laser with a peak intensity, $I_{peak} = 10^{25}Wm^{-2}$ and a temporal intensity profile given by $I = I_{peak}\sin(\pi t/2\tau)$, where the pulse length $\tau = 250fs$. From ponderomotive scaling this pulse yields $T_{hot} = 580KeV$. The heating function is applied spatially as $\sim cos^2(\pi x/x_h)$ where x_h is $5\mu m$. The peak power of the heating function,

$$P_0 = \frac{2I_0}{x_h} = 2 \times 10^{31}$$

The left hand boundary is reflective, meaning that elements of the distribution function with velocities are reflected with an equal and opposite velocity out of the boundary. At the right hand boundary the initial velocity profile is maintained throughout so fast electrons hitting this boundary flow back in at the initial temperature. The quick collision operator is used with the ζ factor described in chapter 3 applied to electron-electron collisions. All collision

terms are assumed non-relativistic since only these non-relativistic electrons are collisional over the timescales considered here. The electric and magnetic field updates in the previous work were handled using an implicit field algorithm which is beneficial for Vlasov-Fokker-Planck since it allows time steps of the order of the collision time. In the explicit field algorithm used in VALIS the time step is limited by the plasma frequency. This is however less of a concern when using the computationally cheap BGK collision operator.

6.3 Results

Figure 6.2 plots the distribution function 50fs into the heating phase. The colour range for the contour plots in this section is set so that values of the distribution function greater than 50 are masked to make the structures in lower values of f visible. The plots in figure 6.2 show the hot electrons streaming through the low density central region exiting kinetic instabilities in particular the two stream instability shown in 6.2(b). In figure 6.3 the electric field and temperature is plotted vs depth for the corresponding 50fs into the heating phase. It's seen that at this point the hottest part of the domain is outside the heated region and inside the low density central region. Joule heating due to the high amplitude Langmuir oscillations is a mechanism for the heating in this region.

The next set of figures are plotted after 300fs, 50fs after the heating pulse has ended. Figure 6.4 plots the distribution function. At this time collisions have damped much of the high amplitude instabilities. The hotter forward current is shown to draw a cool return current visible as a narrow beam of high f in the central region centred around $V_x \sim -1$. The damping of the electric field is seen in figure 6.5 where the peaks of the electric field are less than a third of those seen after 50fs.

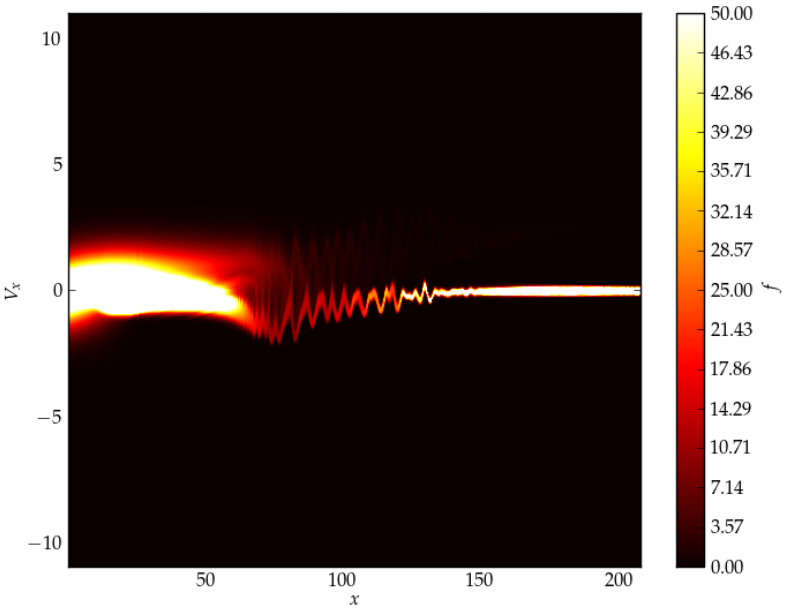

(a) Phase Space

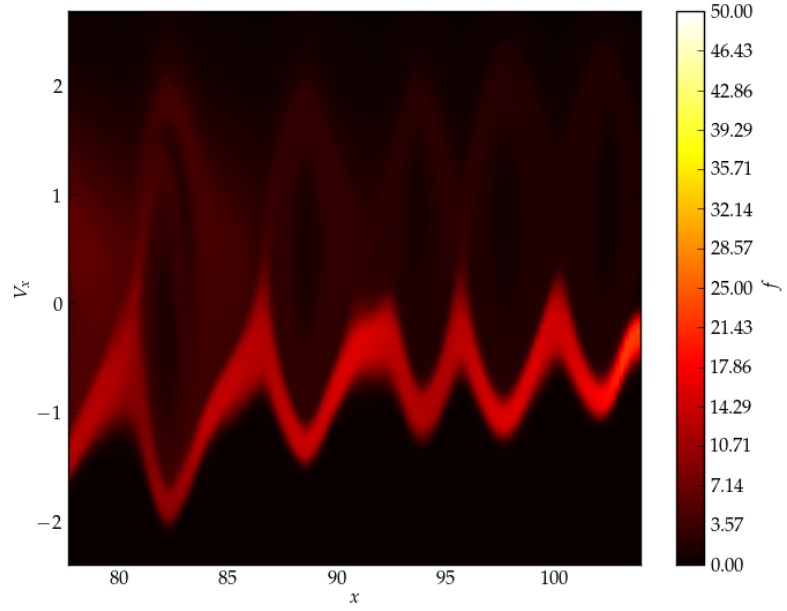

(b) Phase space zoomed about the centre of (a)

Figure 6.2: Phase space plots in normalised units after 50fs

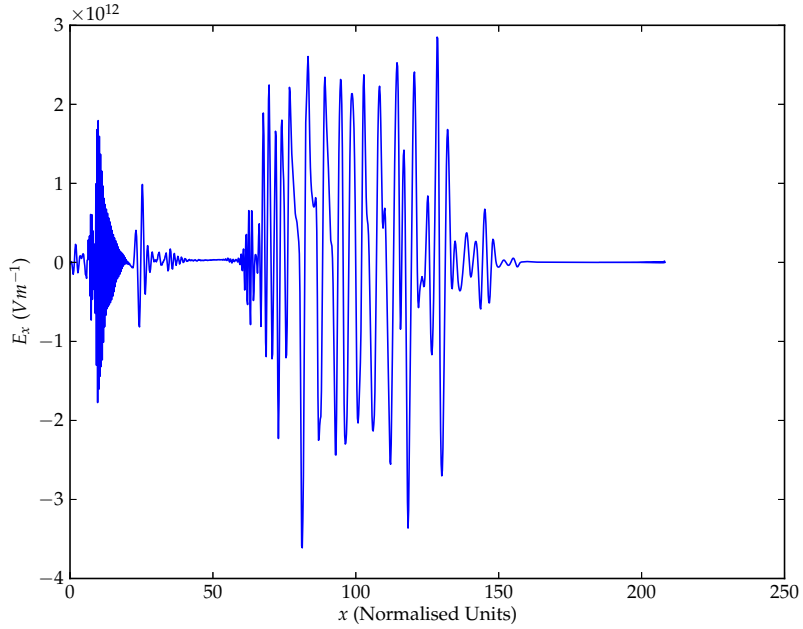

(a) E_x

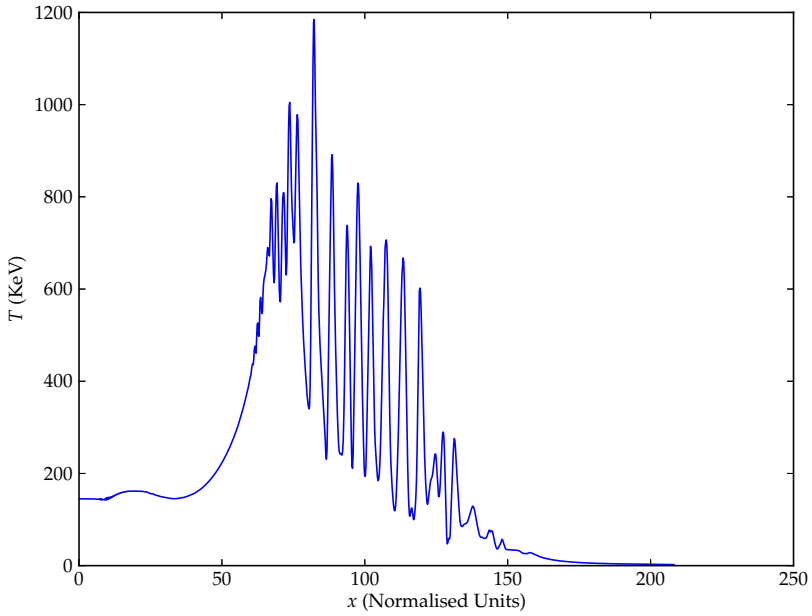

(b) Temperature

Figure 6.3: Electric field and temperature plots after 50fs

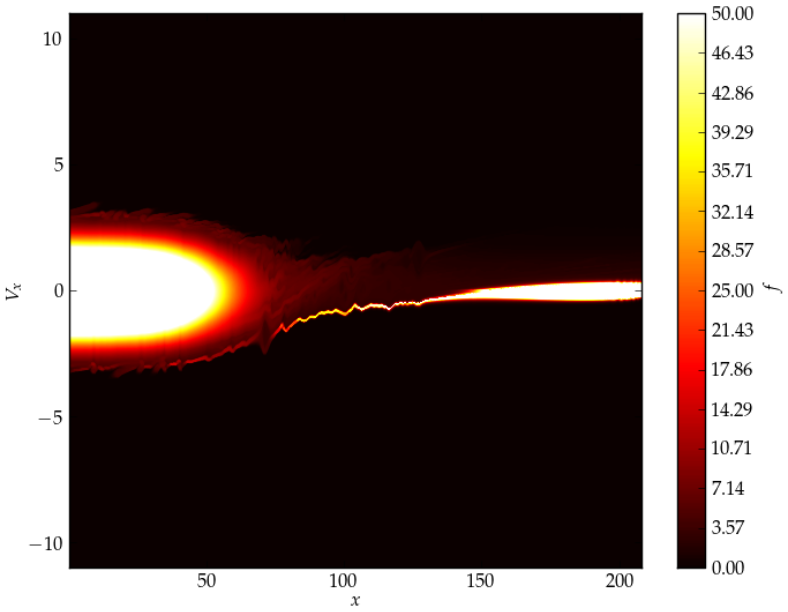

Figure 6.4: Phase space plots in normalised units after 300fs

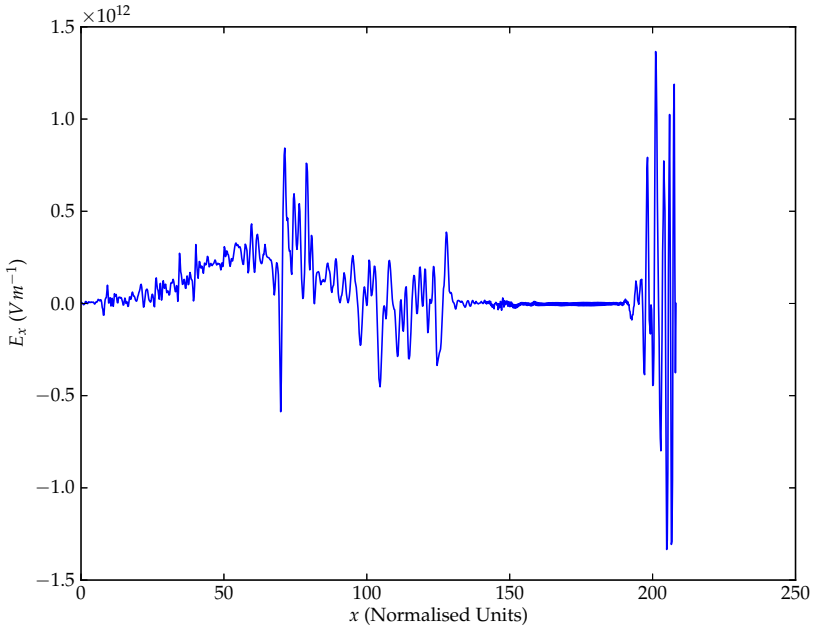

(a) E_x

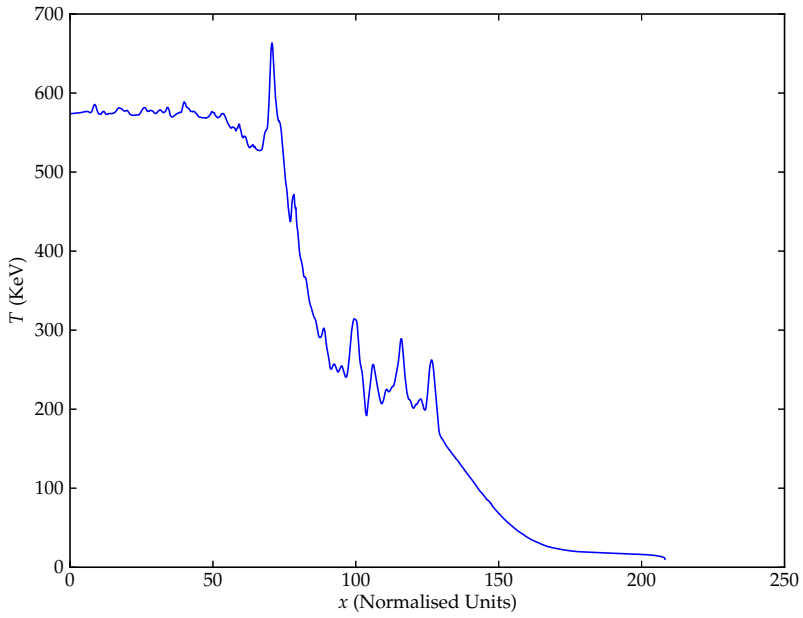

(b) Temperature

Figure 6.5: Electric field and temperature plots after 300fs

6.4 Summary

In this section a simulation of electron heating and transport was carried out. It was seen that early in the simulation the hot electrons produced by the heating function led to the growth a high amplitude ($\sim 3 \times 10^{12} Vm^{-1}$) oscillating electric field. The oscillating currents produced by these fields were then responsible for substantial Joule heating in the low density central region. Later in the simulation a cold return current was seen to be drawn toward the heated plasma. These results however were in contrast to those obtained previously by Sherlock et al. [1]. In their studies an implicit algorithm was used to advance the electric and magnetic fields to allow larger time steps than are possible with the explicit algorithm used in VALIS. This implicit field solver however precludes the resolution of electrostatic instabilities which occur over short timescales, such as the two-stream instability. This was justified by the assumption that collisional effects would damp the growth of these stabilities over the timescale studied. However, The simulations here using an explicit field algorithm showed the effect of collisions was not sufficient to damp the growth of these unstable modes and moreover, these instabilities were responsible for significant heating of the plasma.

Conclusions and Further Work

While progress has been made in providing models of non-local energy transport for use in hydrodynamic simulations [56], solving the computationally intensive Vlasov-Fokker-Planck equation is crucial to properly understanding a variety of kinetic effects and instabilities in an inertial confinement plasma. In particular the supra-thermal electron population generated by an intense pulse leads to non-local heating and electric field generation not predicted by the classical transport coefficients. In terms of fast ignition, understanding the transport of the energetic particle beam produced by the ignitor pulse is crucial. The divergence, filamentation and collimation of this beam must be accurately modelled to provide a useful estimate of the energy that can be deposited at the hotspot. For conventional ICF schemes this non-local transport produces heating ahead of the implosion shock front. This rise in temperature increases the pressure ahead of the shock front, reducing the efficiency of the implosion. This is also an issue for shock ignition schemes that rely on a precise prediction of the implosion velocities in order for the shocks to converge.

In this thesis VALIS, an efficient, parallel Eulerian Vlasov-Maxwell Code developed at Warwick was described and then extended to include a few reduced collision models. The accuracy of these models was assessed through comparison with classical transport co-efficients under the conditions where they are valid. In the regime where energy transport becomes non-local the results were compared to previous simulations using the Fokker-Planck equation. A Krook collision model with a velocity dependent collision frequency was implemented which is able to conserve number, momentum and energy using Newton's method to find the parameters of the equilibrium distribution to enforce this. A quicker Krook method was described that is formulated to

requires no iteration and conserves number for an arbitrary grid spacing while momentum and energy conservation is not guaranteed numerically. As an alternative to the Krook collision model, a reduced Fokker-Planck model based on an advection-diffusion equation is implemented. This model Fokker-Planck equation is implemented with both velocity dependent advection-diffusion and velocity independent advection-diffusion.

Both forms of the Krook collision model and the velocity dependent model Fokker-Planck equation were able to accurately reproduce the electrical resistivity predicted by Spitzer in response to electric field sizes comparable to those encountered in inertial confinement fusion. In the local limit, where the mean free path of the electrons is shorter than the temperature scale length, the Krook collision model was shown to overestimate the thermal conductivity by around 45%. However, by calculating the ratio of the predicted heat flux using the Krook operator with a velocity dependent collision analytically to that given by transport coefficients the operator can be normalised to reproduce accurate local transport derived from the Fokker-Planck equation. This however comes at the cost of reduced accuracy in the results for electrical conductivity where the error was seen to increase by 100% of the Spitzer value. The electrical resistivity is largely due to electron-ion collisions which produce as a drag on the electrons toward the ion centre of mass velocity with a contribution of the relative velocities which are manifested as Joule heating. It was seen that restricting the normalisation to electron-electron collisions a compromise could be made that reduces the error in the heat-flux calculations by around 12% while simultaneously reducing the error in the electrical conductivity by around 5% of their respective transport coefficients. These errors however must be put in context however. The Fokker-Planck model is derived using an expansion in the reciprocal of the Coulomb Logarithm. In regions of low $\log(\lambda)$ encountered in the cool dense core of an ICF capsule the truncation error in the Fokker-Planck equation means there are no guarantees that it is a more accurate model than the Krook model in these regions. The model Fokker-Planck operator however was unable to produce results for the heat flux test in either regime and while the velocity dependent form of the operator performed well in the electrical conductivity and two stream relaxation tests, it suffers a major drawback in that the asymptotic distribution is not the Maxwell-Boltzmann distribution.

The Krook operator was then used on the problem of one-dimensional

fast electron transport through a tenuous plasma to match previous work using an implicit Vlasov-Fokker-Planck code. The accelerated electrons seeded large amplitude Langmuir waves which further acted the heat the plasma. This effect was not seen however in the implicit Vlasov-Fokker-Planck simulation. The implicit update of Maxwell's equations allows time-steps many times larger than the plasma period. While this provides greater efficiency in calculating collisional phenomena, it also precludes the growth of Langmuir oscillations and electrostatic instabilities. The algorithm used in VALIS updates the electric and magnetic fields explicitly using a predictor-corrector method and requires that the plasma period is resolved. Recent results [71] using a Vlasov-Fokker-Planck with an explicit field algorithm however suggest results similar to those obtained with VALIS and the Krook collision operator.

Further work is required optimise in particular the fully conservative Krook operator. Additionally the numerical Jacobian evaluated for relativistic collisions is expensive to compute and analytical integrations of the Maxwell-Jüttner distribution would provide an efficient alternative. While only 1D1P problems were presented in this thesis, the implementation of the Krook collision operator was generalised for 2D2P problems. There are many 2D2P Vlasov-Fokker-Planck simulations of fast electron transport that could be reproduced to further verify the performance of this Krook operator in fast ignition scenarios. While time did not permit here, the model Fokker-Planck operator could be improved by making it fully implicit, which permit greater resolution in velocity space. Doing this may improve the results obtained using the velocity independent variant of the operator. The results in chapter 6 suggest that the growth of fast kinetic instabilities plays an important role in the physics of fast electron transport. Further work is required to quantify these effects however in this regime.

Bibliography

[1] M. Sherlock, a. R. Bell, R. J. Kingham, a. P. L. Robinson, and R. Bingham. Non-Spitzer return currents in intense laser-plasma interactions. *Physics of Plasmas*, 14(10):102708, 2007.

[2] H. A. Bethe and C. L. Critchfield. The Formation of Deuterons by Proton Combination. *Physical Review*, 176, 1938.

[3] HA Bethe. Energy Production in stars. *Physical Review*, (1), 1939.

[4] JD Lawson. Some criteria for a power producing thermonuclear reactor. *Proceedings of the Physical Society. Section B*, 6, 1957.

[5] T. J. M. Boyd and J. J. Sanderson. *The Physics of Plasmas*. Cambridge University Press, Cambridge, 2003.

[6] ITER. http://www.iter.org/faq.

[7] S. Atzeni. Advanced ICF Ignition Schemes. In *Laser-Plasma Interactions and Applications*. Springer, 2013.

[8] Edward I. Moses and Wayne R. Meier. Preparing for ignition experiments on the National Ignition Facility. *Fusion Engineering and Design*, 83(7-9):997–1000, December 2008.

[9] W. L Kruer. Laser-Plasma Coupling with Ignition-Scale Targets. In *Laser-Plasma Interactions and Applications*. Springer, 2013.

[10] https://commons.wikimedia.org/wiki/File:Inertial_confinement_fusion.svg.

[11] Lawrence Livermoor National Laboratory. https://lasers.llnl.gov/programs/nic/icf/.

[12] John Lindl. Development of the indirect-drive approach to inertial confinement fusion and the target physics basis for ignition and gain. *Physics of Plasmas*, 2(11):3933, 1995.

[13] S Fujioka, Z Zhang, N Yamamoto, S Ohira, Y Fujii, K Ishihara, T Johzaki, a Sunahara, Y Arikawa, K Shigemori, Y Hironaka, Y Sakawa, Y Nakata, J Kawanaka, H Nagatomo, H Shiraga, N Miyanaga, T Norimatsu, H Nishimura, and H Azechi. High-energy-density plasmas generation on GEKKO-LFEX laser facility for fast-ignition laser fusion studies and laboratory astrophysics. *Plasma Physics and Controlled Fusion*, 54(12):124042, December 2012.

[14] R. Betti, C. Zhou, K. Anderson, L. Perkins, W. Theobald, and a. Solodov. Shock Ignition of Thermonuclear Fuel with High Areal Density. *Physical Review Letters*, 98(15):155001, April 2007.

[15] Dwight R. Nicholson. *Introduction to Plasma Theory*. John Wiley & Sons, Ltd, New York, 1983.

[16] S Chandrasekhar. Stochastic problems in physics and astronomy. *Reviews of modern physics*, 1943.

[17] MN Rosenbluth and WM MacDonald. Fokker-Planck equation for an inverse-square force. *Physical Review*, 107(1), 1957.

[18] P.L. Bhatnagar, E.P. Gross, and M. Krook. A Model for Collision Processes in Gases. I. Small Amplitude Processes in Charged and Neutral One-Component Systems. *Physical Review*, 94(3):511, 1954.

[19] John M. Greene. Improved Bhatnagar-Gross-Krook model of electron-ion collisions. *Physics of Fluids*, 16(11):2022, 1973.

[20] I. P. Shkarofsky, Ira B. Bernstein, and B. B. Robinson. Condensed Presentation of Transport Coefficients in a Fully Ionized Plasma. *Physics of Fluids*, 6(1):40, 1963.

[21] Henning Struchtrup. The BGK-model with velocity-dependent collision frequency. *Continuum Mechanics and Thermodynamics*, pages 23–31, 1997.

[22] L. Spitzer Jr and R. Harm. Transport phenomena in a completely ionized gas. *Physical Review*, 89(5):977, 1953.

[23] A. G. R. Thomas, M. Tzoufras, A.P.L. Robinson, R. J. Kingham, C.P. Ridgers, M. Sherlock, and A. R Bell. A review of VlasovFokkerPlanck numerical modeling of inertial confinement fusion plasma. *Journal of Computational Physics*, 231(3):1051–1079, October 2012.

[24] J R Davies. Laser absorption by overdense plasmas in the relativistic regime. *Plasma Physics and Controlled Fusion*, 51(1):014006, January 2009.

[25] A. R. Bell, A. P. L. Robinson, M. Sherlock, R. J. Kingham, and W. Rozmus. Fast electron transport in laser-produced plasmas and the KALOS code for solution of the VlasovFokkerPlanck equation. *Plasma Physics and Controlled Fusion*, 48(3):R37–R57, March 2006.

[26] A. Bell and R. Kingham. Resistive Collimation of Electron Beams in Laser-Produced Plasmas. *Physical Review Letters*, 91(3):1–4, July 2003.

[27] P. Gibbon, F. N. Beg, E. L. Clark, R. G. Evans, and M. Zepf. Tree-code simulations of proton acceleration from laser-irradiated wire targets. *Physics of Plasmas*, 11(8):4032, 2004.

[28] M. M. Marinak, G. D. Kerbel, N. a. Gentile, O. Jones, D. Munro, S. Pollaine, T. R. Dittrich, and S. W. Haan. Three-dimensional HYDRA simulations of National Ignition Facility targets. *Physics of Plasmas*, 8(5):2275, 2001.

[29] G.B Zimmerman and W. L Kruer. *Comments on Plasma Physics and Controlled Fusion*, volume 2. 1975.

[30] J. P. Boris. Relativistic Plasma Simulation-Optimization of a Hybrid Code. In *Proceedings of the 4th Conference on Numerical Simulation of Plasmas(NRL)*, pages 3–67, 1970.

[31] N. Besse, G. Latu, A. Ghizzo, E. Sonnendrücker, and P. Bertrand. A wavelet-MRA-based adaptive semi-Lagrangian method for the relativistic VlasovMaxwell system. *Journal of Computational Physics*, 227(16):7889–7916, August 2008.

[32] N. J. Sircombe. VALIS: A split-conservative scheme for the relativistic 2D Vlasov-Maxwell system. *Journal of Computational Physics*, 228(13):4773–4788, 2009.

[33] K. Yee. Numerical solution of initial boundary value problems involving Maxwell's equations in isotropic media. *Antennas and Propagation, IEEE Transactions on*, 14(3):302–307, May 1966.

[34] C. Cheng and G. Knorr. The integration of the vlasov equation in configuration space. *Journal of Computational Physics*, 22(3):330–351, November 1976.

[35] J. D. Hoffman. *Numerical Methods for Engineers and Scientists*. McGraw-Hill, 1992.

[36] P. Colella and P. Woodward. The Piecewise Parabolic Method (PPM) for gas-dynamical simulations. *Journal of Computational Physics*, 54(1):174–201, April 1984.

[37] C.B. Laney. *Computational Gasdynamics*. Cambridge University Press, 1998.

[38] J. Villasenor. Rigorous charge conservation for local electromagnetic field solvers. *Computer Physics Communications*, 69, 1992.

[39] R.J. Kingham and a.R. Bell. *An implicit VlasovFokkerPlanck code to model non-local electron transport in 2-D with magnetic fields*, volume 194. February 2004.

[40] M. Tzoufras, A. Tableman, F. S. Tsung, W. B. Mori, and A. R. Bell. A multi-dimensional Vlasov-Fokker-Planck code for arbitrarily anisotropic high-energy-density plasmas a). 056303:1–11, 2013.

[41] R. J. Mason. An electromagnetic field algorithm for 2D implicit plasma simulation. *Journal of Computational Physics*, 1987.

[42] MPI. The Message Passing Interface (MPI) standard.

[43] S. Eliezer. *The Interaction of High-Power Lasers with Plasmas*. IOP, 2002.

[44] T.D. Arber and R. G. L. Vann. A Critical Comparison of Eulerian-Grid-Based Vlasov Solvers. *Journal of Computational Physics*, 180(1):339–357, July 2002.

[45] Roland Duclous, Bruno Dubroca, Francis Filbet, and Vladimir Tikhonchuk. High order resolution of the Maxwell Fokker Planck Landau model intended for ICF applications. *Journal of Computational Physics*, 228(14):5072–5100, August 2009.

[46] S. Livi and E. Marsch. Comparison of the Bhatnagar-Gross-Krook approximation with the exact Coulomb collision operator. *Physical Review A*, 34(1):533, January 1986.

[47] T. F. Morse. Kinetic Model Equations for a Gas Mixture. *Physics of Fluids*, 7(12):2012, 1964.

[48] G. Medeiros C. Cercignani. *The Relativistic Boltzmann Equation: Theory and Applications*. Springer, 2002.

[49] W. H. Press, B. P. Flannery, S. A. Teukolsky, and W. T. Vetterling. *Numerical Recipes*. Cambridge University Press, 1992.

[50] C. G. Broyden. A Class of Methods for Solving Nonlinear Simultaneous Equations. *Mathematics of Computation*, 19(92):577, October 1965.

[51] B. A. Trubnikov. Particle Interactions in a Fully Ionized Plasma. *Reviews of Plasma Physics*, 1:105, 1965.

[52] J.D. Huba. NRL PLASMA FORMULARY. Technical report, DTIC Document, 2004.

[53] W. Manheimer, D. Colombant, and V. Goncharov. The development of a Krook model for nonlocal transport in laser produced plasmas. I. Basic theory. *Physics of Plasmas*, 15(8):083103, 2008.

[54] JF Luciani and P Mora. Nonlocal heat transport due to steep temperature gradients. *Physical review letters*, 5(18):2–5, 1983.

[55] G. P. Schurtz, Ph. D. Nicolai, and M. Busquet. A nonlocal electron conduction model for multidimensional radiation hydrodynamics codes. *Physics of Plasmas*, 7(10):4238, 2000.

[56] A Marocchino, M Tzoufras, and S Atzeni. Comparison for non-local hydrodynamic thermal conduction models. *Physics of ...*, 022702:1–9, 2013.

[57] D. Colombant and W. Manheimer. The development of a Krook model for nonlocal transport in laser produced plasmas. II. Application of the theory and comparisons with other models. *Physics of Plasmas*, 15(8):083104, 2008.

[58] D. Colombant and W. Manheimer. Krook model for nonthermal electron energy transport. III. Spherical configurations. *Physics of Plasmas*, 16(6):062705, 2009.

[59] D. G. Colombant and W. M. Manheimer. Internal tests and improvements of the Krook model for nonlocal electron energy transport in laser produced plasmas. *Physics of Plasmas*, 17(11):112706, 2010.

[60] S I Braginskii. Transport processes in a plasma. *Reviews of plasma physics*, 1:205–311, 1965.

[61] EM Epperlein and MG Haines. Plasma transport coefficients in a magnetic field by direct numerical solution of the FokkerPlanck equation. *Physics of Fluids*, 29(May 2011):1029, 1986.

[62] A. R. Bell, R. G. Evans, and D. J. Nicholas. Elecron Energy Transport in Steep Temperature Gradients in Laser-Produced Plasmas. *Physical Review Letters*, 46(4):243–246, 1981.

[63] S. C. Wilks, W. L. Kruer, M. Tabak, and A. B. Langdon. Absorption of Ultra-Intense Laser Pulses. *Physical Review Letters*, 69(9):1383–1386, 1992.

[64] C. E. Rathmann and J. Denavit. Simulation of collisional effects in plasmas. *Journal of Computational Physics*, 187:165–187, 1975.

[65] J. P. Dougherty. Model Fokker Planck Equation for a Plasma and Its Solution. *Physics of Fluids*, 7(11):1788, 1964.

[66] J. P. Dougherty and S. R. Watson. Model Fokker Planck Equations: Part 2. The equation for a multicomponent plasma. *Journal of Plasma Physics*, 1(03):317–326, 1967.

[67] B Wang, GH Miller, and P Colella. A Particle-in-Cell Method With Adaptive Phase-Space Remapping for Kinetic Plasmas. *SIAM Journal on Scientific Computing*, 33(6):3509–3537, 2011.

[68] EH Twizell, AB Gumel, and MA Arigu. Second-order, L 0-stable methods for the heat equation with time-dependent boundary conditions. *Advances in Computational ...*, 6:333–352, 1996.

[69] D. Umstadter. Relativistic laserplasma interactions. *Journal of Physics D: Applied Physics*, 151, 2003.

[70] D. Bauer and P. Mulser. Vacuum heating versus skin layer absorption of intense femtosecond laser pulses. *Physics of Plasmas*, 14(2):023301, 2007.

[71] M. Sherlock. Ifsa 2013 Conference Proceedings.